Investigating Galaxy Evolution and Active Galactic Nucleus Feedback with the Sunyaev-Zel'dovich Effect

by

Alexander Edward Spacek

A Dissertation Presented in Partial Fulfillment
of the Requirements for the Degree
Doctor of Philosophy

Approved June 2017 by the
Graduate Supervisory Committee:

Evan Scannapieco, Chair
Judd Bowman
Nat Butler
Chris Groppi
Patrick Young

ARIZONA STATE UNIVERSITY

August 2017

ABSTRACT

Galaxy formation is a complex process with aspects that are still very uncertain or unknown. A mechanism that has been utilized in simulations to successfully resolve several of these outstanding issues is active galactic nucleus (AGN) feedback. Recent work has shown that a promising method for directly measuring this energy is by looking at small increases in the energy of cosmic microwave background (CMB) photons as they pass through ionized gas, known as the thermal Sunyaev-Zel'dovich (tSZ) effect.

In this work, I present stacked CMB measurements of a large number of elliptical galaxies never before measured using this method. I split the galaxies into two redshift groups, "low-z" for z=0.5-1.0 and "high-z" for z=1.0-1.5. I make two independent sets of CMB measurements using data from the South Pole Telescope (SPT) and the Atacama Cosmology Telescope (ACT), respectively, and I use data from the Planck telescope to account for contamination from dust emission. With SPT I find average thermal energies of $7.6^{+3.0}_{-2.3} \times 10^{60}$ erg for 937 low-z galaxies, and $6.0^{+7.7}_{-6.3} \times 10^{60}$ erg for 240 high-z galaxies. With ACT I find average thermal energies of $5.6^{+5.9}_{-5.6} \times 10^{60}$ erg for 227 low-z galaxies, and $7.0^{+4.7}_{-4.4} \times 10^{60}$ erg for 529 high-z galaxies.

I then attempt to further interpret the physical meaning of my observational results by incorporating two large-scale cosmological hydrodynamical simulations, one with (Horizon-AGN) and one without (Horizon-NoAGN) AGN feedback. I extract simulated tSZ measurements around a population of galaxies equivalent to those used in my observational work, with matching mass distributions, and compare the results. I find that the SPT measurements are consistent with Horizon-AGN, falling within 0.4σ at low-z and 0.5σ at high-z, while the ACT measurements are very different from Horizon-AGN, off by 6.9σ at low-z and 14.6σ at high-z. Additionally, the SPT measurements are loosely inconsistent with Horizon-NoAGN, off by 1.8σ at low-z

but within 0.6σ at high-z, while the ACT measurements are loosely consistent with Horizon-NoAGN (at least much more so than with Horizon-AGN), falling within 0.8σ at low-z but off by 1.9σ at high-z.

Dedicated to Amanda, Sneezy, and Flurry. They inspire all I do.

ACKNOWLEDGMENTS

For all of the general work contained within this dissertation, I owe much to my advisor, Evan Scannapieco, who has helped me with every aspect of it. I have also been helped immensely by the other co-authors of Chapters 2 and 3: Seth Cohen, Bhavin Joshi, and Phil Mauskopf. A special debt is also owed to Mark Richardson for countless reasons, especially for qualifying exam help and the work done in Chapter 4. I also must thank all current and former members of my PhD committee for their years of keeping tabs on my progress and giving me advice: Judd Bowman, Nat Butler, Chris Groppi, Sangeeta Malhotra, Phil Mauskopf, and Patrick Young. Obvious gratitude goes to Arizona State University, the School of Earth and Space Exploration, and anyone within those groups who has been helpful. Enormous thanks go to Amanda Truitt, Rick Sarmento, and Luke Probst for sharing offices with me and for their help through insightful talks and general support. Finally, thanks to Mike Veto for sharing a house with me for several years, Anusha Kalyan and Peter Nguyen for sharing an office with me, George Che and Becky Jackson for late-night homework sessions, and the rest of my fellow graduate students who I took classes with, played games with, watched movies with, and everything else.

For my South Pole Telescope work specifically, I thank Shantanu Desai, Mariska Kriek, Eliot Quataert, and Daniel Marrone for helpful discussions, and the anonymous ApJ referee for very helpful comments. This work was supported by the National Science Foundation (NSF) under grant AST14-07835. ES gratefully acknowledges Joanne Cohn, Eliot Quataert, the UC Berkeley Theoretical Astronomy Center, and Uroš Seljak and the Lawrence Berkeley National Lab Cosmology group, for hosting him when a lot of this work was done. I would also like to thank the Joint Space-Science Institute for letting me present a poster of this work at the 2015 Supermassive Black Hole Formation and Feedback conference.

For my Atacama Cosmology Telescope (ACT) work specifically, I would like to thank Arthur Kosowsky for helpful discussions. The publication makes use of data products from the WISE, which is a joint project of UCLA, JPL, and Caltech funded by NASA. It also makes use of data produced from SDSS-III, which was funded by the Alfred P. Sloan Foundation, the NSF, the U.S. Department of Energy Office of Science, and the SDSS-III Participating Institutions. Finally, I make use of data from the ACT project, which operates in the Parque Astronómico Atacama in northern Chile under the auspices of the Comisión Nacional de Investigación Científica y Tecnológica de Chile (CONICYT), and is funded by the NSF, Princeton University, U. Penn., and a Canada Foundation for Innovation award to UBC. This work was supported by the NSF under grant AST14-07835.

For my Horizon simulation work specifically, I would like to thank Julien Devriendt, Mark Richardson, and the University of Oxford for hosting me when a significant part of the work was carried out. I'd also like to thank the ASU Graduate and Professional Student Association for funding part of my travel to the United Kingdom through their travel grant. This work has made use of the Horizon Cluster, hosted by Institut d'Astrophysique de Paris, and data from the Horizon simulations (horizon-simulation.org/about.html), with generous help from Stephane Rouberol.

For my life in general while completing this work, I'd like to sincerely thank my entire extended family (aunts, uncles, cousins) for being amazing, and especially thank my mom, dad, grandma, and grandpa for their incredible and constant support. Infinite thanks to Amanda Truitt for literally everything, and thanks to her mom, dad, sister, and the rest of her family for being amazing. Thanks to all my friends for being awesome, especially Marcus Ghiasi for decades of good times. Thanks to Sneezy and Flurry for bringing me joy. And finally, thanks to Rick and Morty, Key & Peele, and the (American) Office for making me laugh throughout graduate school.

TABLE OF CONTENTS

Page

CHAPTER Page

CHAPTER Page

LIST OF TABLES

Table Page

Table Page

LIST OF FIGURES

Figure Page

Chapter 1

INTRODUCTION

1.1 Perspective

A large part of the world's population, especially in the United States, lives either in or relatively close to areas of modern human technology and the corresponding light pollution. This makes nothing but the brightest stars, planets, and moon visible. I have been one of these people for most of my life, growing up about 10 miles from San Francisco, California, going to college near San Diego, California, and going to graduate school near Phoenix, Arizona. It is really not so bad, given just how much wonderful and mysterious magnificence is contained within a single star or planet, but it is far from the full picture and represents just a minuscule sphere within the scale of the Universe. Any time I have traveled away from the light of the cities, though, I have been treated to a much more glorious sight: countless stars, unique phenomena such as nebulae and star clusters, and what impresses me the most, the Andromeda galaxy.

To provide perspective, the visible, bright, and fairly distant star Deneb, located in our own Milky Way galaxy, is approximately 800 pc from Earth (Schiller & Przybilla, 2008), while the Andromeda galaxy is approximately 770,000 pc from Earth (Karachentsev et al., 2004). This is roughly equivalent to the following scenario: if the Earth was at the Golden Gate Bridge, and Andromeda was at the Statue of Liberty, 2566 mi away (a scale of 300 parsecs per mile), then Deneb would be at Alcatraz Island, a mere 3 mi away (see Figure 1.1). The closest star to us, Proxima Centauri,

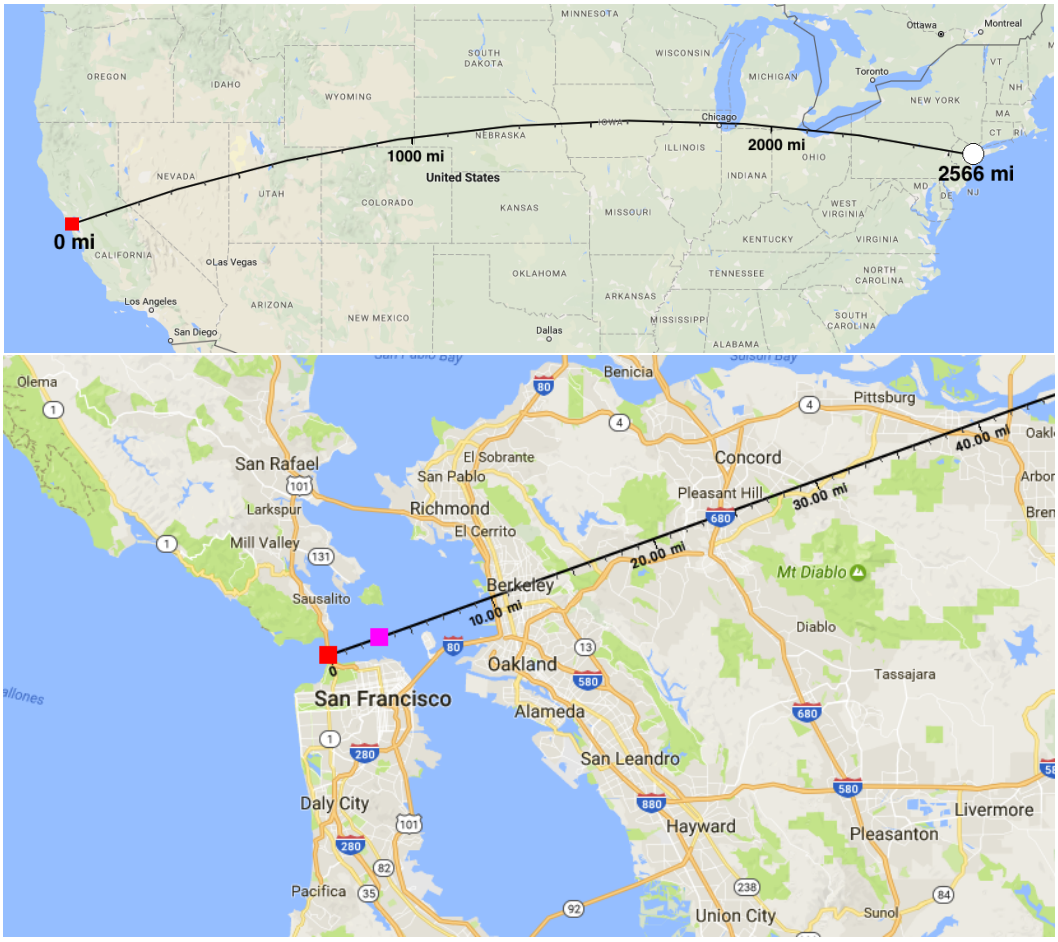

Figure 1.1: Top: distance from the Golden Gate Bridge (red square) to the Statue of Liberty (white circle), 2566 mi. Bottom: magnification of the red square in the top image, now with the Golden Gate Bridge (red square) and Alcatraz Island (purple square), 3 mi away, clearly visible. Taken from Google Maps, 2017.

would only be 23 ft away, about the width of two of the lanes[1] going across the bridge (Lurie et al., 2014). This illustrates the vast scale of galaxies, still just a tiny scale within the Universe, but a scale at which a seemingly endless number of fascinating and important processes take place.

[1] goldengatebridge.org/projects/MoveableMedianBarrier.php

1.2 Galaxies and Active Galactic Nucleus Feedback

Starting at just a few hundred million years after the Big Bang (e.g. Richard et al., 2011), galaxies have been the main observable component of the large-scale structure of the Universe, revealing both dark matter (e.g. Blumenthal et al., 1984) and dark energy (e.g. Blake et al., 2011), and ultimately creating the conditions that formed our Solar System and allowed life to evolve on Earth. Since 1929, when Edwin Hubble first observed that Cepheid variable stars in the Andromeda galaxy indicated a distance much larger than the rest of the stars in the sky (Hubble, 1929), and even earlier (e.g. MacPherson, 1916), galaxies have been a prominent focus in astrophysics research. The broad focus of the work presented here is the evolution of galaxies over time.

As more and more galaxies, likely numbering in the millions today, are observed with increasingly powerful telescopes, they are found to vary wildly in all imaginable aspects. Still, a significant fraction of them (e.g. $\sim$1% of local galaxies; Page, 2001) are host to an active galactic nucleus (AGN). Early studies of AGNs (before they were known to be the active centers of galaxies) were done by Carl Seyfert in 1943 (Seyfert, 1943), who looked at galaxies with nuclear emission lines, and then by Maarten Schmidt and others in 1963 (Schmidt, 1963), who looked at extremely bright quasars at high redshifts (for a nice history of AGNs, see Shields, 1999). By the early 1970s it was becoming clear that these quasars were located at the centers of galaxies (Gunn, 1971; Kristian, 1973), and soon AGNs became associated with accretion onto supermassive black holes at the centers of galaxies (e.g. Lynden-Bell, 1969; Rees, 1984). It also became apparent that several different types of observed objects (i.e. Seyfert galaxies, quasars, BL Lac objects, and radio galaxies) were actually AGNs viewed at different orientations (e.g. Antonucci, 1993).

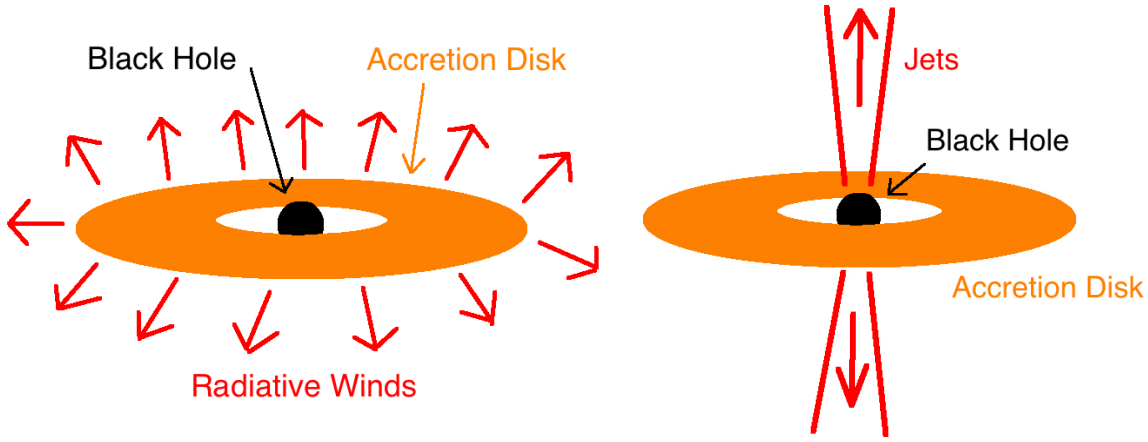

Figure 1.2: Simple diagrams of radiative mode (left) and kinetic mode (right) models of AGN feedback.

These AGNs are some of the most energetic phenomena observed in the Universe. Not only are these extreme energies impressive to witness, they also have a potentially drastic impact on the evolution of the galaxies containing them, a process known as AGN feedback. A good detailed review of AGN feedback is given in Fabian (2012). The basis of the feedback process is accretion onto the supermassive black hole, and it can be categorized into two modes: radiative mode (also known as quasar mode; Figure 1.2 left) and kinetic mode (also known as radio mode; Figure 1.2 right). Radiative mode happens when the black hole accretion is extremely energetic, close to the Eddington limit (i.e. the point where the energy released threatens to rip the black hole apart; see above Equation 2.13), and the radiative winds are able to push cold gas around. Kinetic mode typically happens at lower accretion rates where the black hole has powerful radio jets that are able to inject large amounts of energy into the surrounding medium and heat gas up. One potentially important consequence of this AGN feedback is that it may be able to both heat up and push out cool gas in and around galaxies and prevent further collapse of gas into star formation and AGN accretion.

Many details regarding the specific nature, evolution, and impact of AGN feedback are highly uncertain, and although it is often utilized in modern galaxy simulations with great success, direct observations of AGN feedback and the associated energetics have been difficult. Quasar activity and the richness of gas in galaxies, and therefore the impact of AGN feedback, likely peaked around $z \sim 2-3$ (e.g. Fabian, 2012). Directly observing galaxies and their associated feedback at these high redshifts typically requires very powerful telescopes with high angular resolutions and high sensitivities. However, there is a novel way of measuring the thermal energy around galaxies at any redshift by looking at the scattering of photons from the cosmic microwave background (CMB), known as the thermal Sunyaev-Zel'dovich (tSZ) effect.

1.3 The Thermal Sunyaev-Zel'dovich Effect

The origins of this CMB phenomenon go back to 1923, when Arthur Compton discovered that photons could scatter off of electrons and transfer some of their momentum to the electrons, a process known as Compton scattering (Compton, 1923). Then in the 1940s, Eugene Feenberg and Henry Primakoff did work on the interaction between photons and cosmic rays (Feenberg & Primakoff, 1948), where the electrons had such high energies that they boosted the momentum of the photons, a process known as inverse Compton scattering (e.g. Jones, 1965). This coincided with the first predictions of the CMB in 1948 by Ralph Alpher and Robert Herman (Alpher & Herman, 1948), which was finally detected in 1965 by Arno Penzias and Robert Wilson (Penzias & Wilson, 1965, see left panel of Figure 1.3). Following this, Rashid Sunyaev and Yakov Zel'dovich developed a theory for expected small perturbations in the CMB due to inverse Compton scattering of the CMB photons off of ionized

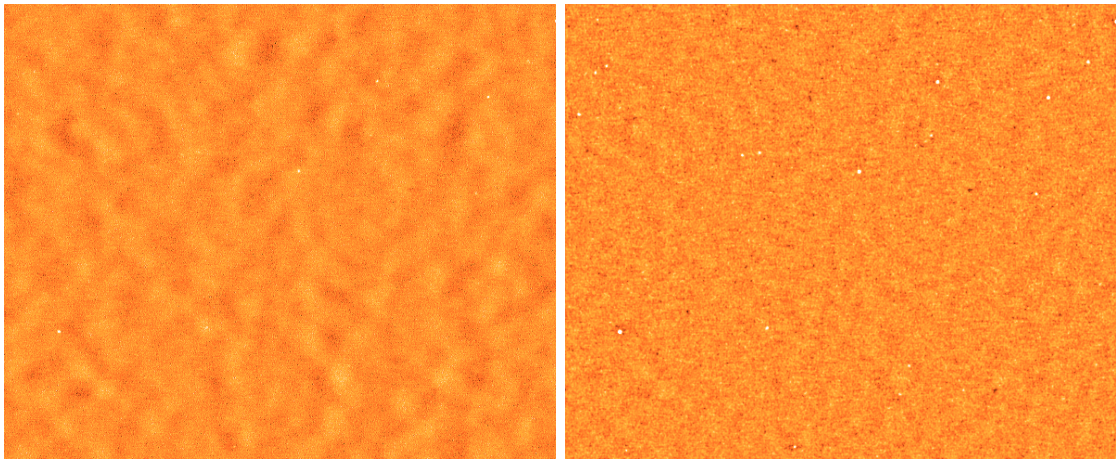

Figure 1.3: Left: 3×7 deg image of fluctuations of the CMB at 150 GHz from the South Pole Telescope (Schaffer et al., 2011), revealing large-scale anisotropies. Right: the same region and data, but filtered such that the large-scale fluctuations are suppressed, revealing small-scale anisotropies such as the SZ effect (see Figure 2.8).

gas, known as the Sunyaev-Zel'dovich (SZ) effect (Sunyaev & Zeldovich, 1970, 1972, see right panel of Figure 1.3).

Jump ahead to the late 1990s, and Natarajan and Sigurdsson suggested that AGN feedback might create a detectable SZ signal (Natarajan & Sigurdsson, 1999). In the 2000s, the upcoming launches of several next-generation millimeter-sensitive telescopes, including the South Pole Telescope (SPT), Atacama Cosmology Telescope (ACT), Planck space telescope (Planck), and Atacama Large Millimeter/ submillimeter Array (ALMA), opened up the opportunity for unprecedentedly powerful CMB measurements. In 2004, Scannapieco and Oh investigated the significance of AGN feedback in galaxy evolution and proposed that future CMB measurements might help constrain the impact of AGN feedback (Scannapieco & Oh, 2004). These possibilities prompted Chatterjee and Kosowsky to theoretically investigate the promise of measuring AGN feedback energy with the tSZ effect in 2007 (Chatterjee & Kosowsky, 2007), applying this theory to cosmological simulations in 2008 (Chatterjee et al., 2008) around the same time as separate simulation studies by Scannapieco, Thacker,

and Couchman (Scannapieco et al., 2008), whose paper forms the main conceptual basis for the work done in this dissertation.

1.4 Observational Motivation

From the 1970s to the 1990s, the prevailing model of galaxy formation consisted of the idea that galaxies form through the collapse of gas into the densest dark matter structures (e.g. White & Rees, 1978; White & Frenk, 1991; Kauffmann et al., 1993; Lacey & Cole, 1993). As time goes on, larger structures are able to form, and as gas falls into these potential wells it gets heated. The gas needs time to radiate this energy away so that it can collapse further and form stars (and thus galaxies), and this cooling time grows longer the more the gas is heated (e.g. Binney, 1977; Rees & Ostriker, 1977; Silk, 1977). This corresponds to larger dark matter structures and later times. Further heating and growth occurs as galaxies merge within dark matter halos, and this is observed to be related to AGN evolution (e.g. Richstone et al., 1998; Cattaneo et al., 1999; Kauffmann & Haehnelt, 2000; Menci, 2006). Overall, structures are expected to form hierarchically with the largest and most energetic structures forming at the latest times (i.e. larger galaxies forming today than in the past).

Starting in the 1990s, though, and building greatly in the 2000s, an increasing number of observations started revealing a much more complex picture of structure formation with anti-hierarchical trends. Since $z \approx 2$ the typical mass of star-forming galaxies has decreased by a factor of $\approx$10 or more (Cowie et al., 1996; Brinchmann et al., 2004; Kodama et al., 2004; Bauer et al., 2005; Bundy et al., 2005; Feulner et al., 2005; Treu et al., 2005; Papovich et al., 2006; Noeske et al., 2007; Cowie & Barger, 2008; Drory & Alvarez, 2008; Vergani et al., 2008; Kang et al., 2016; Rosas-Guevara et al., 2016; Siudek et al., 2016). During roughly the same time, the typical luminosity

of AGNs is observed to have decreased by as much as a factor of ≈1000 (Pei, 1995; Ueda et al., 2003; Barger et al., 2005; Hopkins et al., 2007; Buchner et al., 2015). These trends indicate that less massive galaxies are forming stars and smaller black holes are becoming AGNs as time goes on, contrary to the simple hierarchical formation model. It is possible that the standard hierarchical model naturally produces these anti-hierarchical trends (e.g. Enoki et al., 2014), but it is more likely that these trends, combined with other well-known relationships between black holes and their host galaxies like the $M_{\rm BH}$–$\sigma_\star$ relation (e.g. Shankar et al., 2016), indicate a mechanism affecting both the small scale of the black hole and the large scale of the galaxy.

One promising mechanism used to explain these trends is energetic feedback from accreting supermassive black holes, i.e. AGN feedback, which heats and blows out cool gas around galaxies and which has become a prominent process in theoretical and numerical models of galaxy evolution (Merloni, 2004; Scannapieco & Oh, 2004; Scannapieco et al., 2005; Bower et al., 2006; Neistein et al., 2006; Thacker et al., 2006; Sijacki et al., 2007; Merloni & Heinz, 2008; Chen et al., 2009; Hirschmann et al., 2012; Mocz et al., 2013; Hirschmann et al., 2014; Lapi et al., 2014; Schaye et al., 2015; Kaviraj et al., 2016; Keller et al., 2016). AGN feedback has been most notably observed in the form of giant radio jets within galaxy clusters (Schawinski et al., 2007; Rafferty et al., 2008; Fabian, 2012; Farrah et al., 2012; Page et al., 2012; Teimoorinia et al., 2016), where central galaxies tend to host these jets and may have energies large enough to effectively prevent gas from cooling (Burns, 1990; Bîrzan et al., 2004; Best et al., 2005; McNamara et al., 2005; Rafferty et al., 2006; Brüggen & Scannapieco, 2009; Simionescu et al., 2009).

Direct measurements of AGN feedback in environments less dense than clusters are uncommon because of the high redshifts and faint signals involved. Broad absorption-line outflows are observed in the spectra of ≈20% of all of quasars (Hewett & Foltz,

2003; Ganguly & Brotherton, 2008; Knigge et al., 2008), but in order to quantify the AGN feedback energy the mass and energy of the outflows must be estimated (e.g. Wampler et al., 1995; de Kool et al., 2001; Hamann et al., 2001; Feruglio et al., 2010; Sturm et al., 2011; Veilleux et al., 2013). This is often highly uncertain, and while several of these measurements have been made (e.g. Chartas et al., 2007; Moe et al., 2009; Dunn et al., 2010; Greene et al., 2012; Borguet et al., 2013; Chamberlain et al., 2015), it is unclear how these results generalize to AGNs as a whole. The same goes for a select few measurements that provide evidence of AGN feedback in nearby galaxies (e.g. Tombesi et al., 2015; Lanz et al., 2016; Schlegel et al., 2016).

An effective, novel method for measuring the AGN feedback energy around galaxies at high redshifts and low signals is by stacking CMB measurements of the tSZ effect. The CMB has large-scale fluctuations that have been measured in great detail recently and provide insight into the cosmological parameters that shape our universe (e.g., Planck Collaboration et al., 2015d). At angular scales smaller than $\approx$5 arcmin, though, Silk damping suppresses the primary CMB fluctuations (Silk, 1968; Planck Collaboration et al., 2015d), revealing small-scale fluctuations such as the SZ effect, where CMB photons are scattered by hot, ionized gas (Sunyaev & Zeldovich, 1970, 1972). When the gas has a bulk velocity, CMB photons interacting with electrons in the gas experience a Doppler boost, resulting in frequency-independent fluctuations in the CMB temperature known as the kinematic Sunyaev-Zel'dovich (kSZ) effect. The kSZ effect can be used to measure where ionized gas is located within dark matter halos, providing insight on the hot gas around galaxies. This can be useful for understanding how AGN feedback heats up gas and moves it around (Battaglia et al., 2010). Some of the first detections of the kSZ effect in galaxy clusters have been made recently by stacking CMB observations with Planck (Planck Collaboration et al., 2016), the SPT (Soergel et al., 2016), and the ACT (Schaan et al., 2016).

On the other hand, for hot enough gas, inverse Compton scattering will shift the CMB photons to higher energies, resulting in the redshift-independent tSZ effect. The tSZ effect depends on the thermal energy of the free electrons that the CMB radiation passes through, and it has a unique spectral signature that makes it well suited for measuring AGN feedback energy (Voit, 1994; Birkinshaw, 1999; Natarajan & Sigurdsson, 1999; Platania et al., 2002; Lapi et al., 2003; Chatterjee & Kosowsky, 2007; Chatterjee et al., 2008; Scannapieco et al., 2008; Battaglia et al., 2010). Measurements of the tSZ effect have been useful in detecting massive galaxy clusters (e.g. Reichardt et al., 2013), and simulations have shown that the tSZ effect can be effective in distinguishing between models of AGN feedback (e.g. Chatterjee et al., 2008; Scannapieco et al., 2008). Individual tSZ signals are weak, however, so a stacking analysis must be performed on many galaxies in order to derive a significant measurement.

This method has been used previously by a handful of studies in relation to AGNs and galaxies. Chatterjee et al. (2010) found a tentative detection of quasar feedback using the Sloan Digital Sky Survey (SDSS) and Wilkinson Microwave Anisotropy Probe (WMAP), though the significance of AGN feedback in their measurements is disputed (Ruan et al., 2015). Hand et al. (2011) stacked >2300 SDSS-selected "luminous red galaxies" in data from the ACT and found a $2.1\sigma - 3.8\sigma$ tSZ detection after selecting radio-quiet galaxies and binning them by luminosity. Planck Collaboration et al. (2013) investigated the relationship between tSZ signal and stellar mass using ≈260,000 "locally brightest galaxies" with significant results, especially with stellar masses $\gtrsim 10^{11} M_{\odot}$. Gralla et al. (2014) stacked data from the ACT at the positions of a large sample of radio AGNs selected at 1.4 GHz to make a 5σ detection of the tSZ effect associated with the haloes that host active AGNs. Greco et al. (2015) used Planck full-mission temperature maps to examine the stacked tSZ signal of 188,042 "locally brightest galaxies" selected from the SDSS Data Release 7, finding a signifi-

cant measurement of the stacked tSZ signal from galaxies with stellar masses above $\approx 2\times10^{11} M_{\odot}$. Ruan et al. (2015) stacked Planck tSZ Compton-y maps centered on the locations of 26,686 spectroscopic quasars identified from SDSS to estimate the mean thermal energies in gas surrounding such $z \approx 1.5$ quasars to be $\approx 10^{62}$ erg, although the significance of AGN feedback in their measurements has also been disputed (Cen & Safarzadeh, 2015b). Crichton et al. (2016) stacked >17,000 radio-quiet quasars from the SDSS in ACT data and found 3σ evidence for the presence of associated thermalized gas and 4σ evidence for the thermal coupling of quasars to their surrounding medium. Hojjati et al. (2016) used data from Planck and RCSLenS to find a tSZ signal suggestive of AGN feedback. These tSZ AGN feedback measurements continue to be promising.

Quasars are a popular target for measuring AGN feedback due to their brightness and their active feedback processes, but they have drawbacks due to their relative scarcity and the contaminating emission they contain that obscures the tSZ signatures of AGN feedback. In Chapters 2 and 3 of this dissertation, we focus on measuring co-added tSZ distortions in the CMB around massive ($\geq 10^{11} M_{\odot}$) quiescent elliptical galaxies at moderate redshifts ($0.5 \leq z \leq 1.5$), using data from the Blanco Cosmology Survey (BCS; Desai et al., 2012), SDSS (Alam et al., 2015), VISTA Hemisphere Survey (VHS; McMahon, 2012), Wide-Field Infrared Survey Explorer (WISE; Wright et al., 2010), SPT SZ survey (SPT-SZ; Schaffer et al., 2011), and ACT (Dünner et al., 2013). These galaxies contain almost no dust and are numerous in the sky, making them well-suited for co-adding in large numbers in order to obtain constraints on the energy stored in the surrounding gas.

Directly measuring the energy and distribution of hot gas around galaxies can only reveal so much about the specific physical mechanisms resulting in the observations. In order to place constraints on AGN feedback and other non-gravitational heat-

ing processes, it is necessary that observational work be complimented by accurate, detailed simulations. There is a rich history of complementing tSZ measurements and AGN feedback with simulations. For example, both Scannapieco et al. (2008) and Chatterjee et al. (2008) used large-scale cosmological simulations to give details about the possibilities of measuring AGN feedback with the tSZ effect, Cen & Safarzadeh (2015b) used simulations to investigate the feedback energies from quasars and implications for tSZ measurements, Hojjati et al. (2015) used large-scale cosmological simulations to estimate AGN feedback effects on cross-correlation signals between gravitational lensing and tSZ measurements, and Dolag et al. (2016) used large-scale simulations to study the impact of structure formation and evolution with AGN feedback on tSZ measurements.

In Chapter 4 of this dissertation, we utilize the large-scale cosmological simulations Horizon-AGN and Horizon-noAGN, which are simulations with and without AGN feedback, respectively (Dubois et al., 2012, 2014; Kaviraj et al., 2015, 2016), to compliment the work done in Chapters 2 and 3. We investigate looking at a similar population of moderate redshift, quiescent elliptical galaxies and simulate their tSZ measurements. We then use their measurement distribution and stacking statistics to give insight into the previous observational results. These Horizon simulations have a comoving volume of 100 Mpc/h, 1024^3 dark matter particles, and a minimum cell size of 1 physical kpc, which allow for a large enough population of the generally uncommon galaxies we are interested in.

The structure of this manuscript is as follows: in Chapter 2, I present the published work "Constraining AGN Feedback in Massive Ellipticals with South Pole Telescope Measurements of the Thermal Sunyaev-Zel'dovich Effect" (Spacek et al., 2016). In Chapter 3, I present the published work "Searching for Fossil Evidence of AGN Feedback in WISE-selected Stripe-82 Galaxies by Measuring the Thermal

Sunyaev-Zel'dovich Effect with the Atacama Cosmology Telescope" (Spacek et al., 2017). In Chapter 4, I present an analysis of the observational results presented in the previous two chapters by comparing their tSZ stacking measurements with galaxy measurements taken from the Horizon-AGN and Horizon-noAGN cosmological simulations. In Chapter 5, I discuss the overall results, tying together the work done in the previous three chapters, and conclude with an outline of future work that can be done to improve and enhance the results presented here.

Chapter 2

CONSTRAINING AGN FEEDBACK IN MASSIVE ELLIPTICALS WITH SOUTH POLE TELESCOPE MEASUREMENTS OF THE THERMAL SUNYAEV-ZEL'DOVICH EFFECT

2.1 Introduction

In the prevailing model of galaxy formation, the collapse of baryonic matter follows the collapse of overdense regions of dark matter (e.g., White & Rees, 1978; White & Frenk, 1991; Kauffmann et al., 1993; Lacey & Cole, 1993). Over time, these dark matter halos accrete and merge to form deep gravitational potential wells. These, in turn, lead to strong gravitationally powered shocks that cause the inflowing gas to be heated to high temperatures. To collapse and form stars, the gas must radiate this energy away, a process that takes longer in the largest, most gravitationally bound structures (e.g., Binney, 1977; Rees & Ostriker, 1977; Silk, 1977). Furthermore, galaxies also accrete and merge over time within their dark matter halos, a process that appears to be closely linked to the evolution of active galactic nuclei (AGNs; e.g., Richstone et al., 1998; Cattaneo et al., 1999; Kauffmann & Haehnelt, 2000). Together, these processes point to a hierarchical picture in which larger star-forming galaxies, hosting larger AGNs, form at later times as larger dark matter halos coalesce and more gas cools and condenses.

On the other hand, an increasing amount of observational evidence suggests that recent trends in galaxy and AGN evolution were anti-hierarchical. More massive galaxies appear to be forming stars at higher redshift, and since $z \approx 2$ the characteristic mass of star-forming galaxies appears to have dropped by more than a factor

of 3 (Cowie et al., 1996; Brinchmann et al., 2004; Kodama et al., 2004; Bauer et al., 2005; Bundy et al., 2005; Feulner et al., 2005; Treu et al., 2005; Papovich et al., 2006; Noeske et al., 2007; Cowie & Barger, 2008; Drory & Alvarez, 2008; Vergani et al., 2008). Similarly, since $z \approx 2$ the characteristic AGN luminosity has dropped by more than a factor of 10, indicating that the typical masses of active supermassive black holes were larger in the past (Pei, 1995; Ueda et al., 2003; Barger et al., 2005; Buchner et al., 2015). While it has been argued that this observed "downsizing" is a natural result of the standard hierarchical framework (e.g., Enoki et al., 2014), most work has suggested that it requires additional heating of the circumgalactic medium by AGN feedback (Merloni, 2004; Scannapieco & Oh, 2004; Scannapieco et al., 2005; Bower et al., 2006; Neistein et al., 2006; Thacker et al., 2006; Sijacki et al., 2007; Merloni & Heinz, 2008; Chen et al., 2009; Hirschmann et al., 2012, 2014; Mocz et al., 2013; Lapi et al., 2014; Schaye et al., 2015).

In a general AGN feedback model (e.g., Scannapieco et al., 2005), energetic AGN outflows due to broad absorption-line winds and/or radio jets blow cool gas out of the galaxy and/or heat the nearby intergalactic medium (IGM) enough to suppress the cooling needed to form further generations of stars and AGNs. This quenching is redshift dependent, as the higher-redshift IGM is more dense and rapidly radiating and therefore a highly energetic outflow driven by a large AGN is required to have effective feedback. In the less dense lower-redshift IGM, a less energetic outflow by a smaller AGN can produce similar cooling times. This means that at lower redshifts the AGNs in smaller galaxies can exert efficient feedback, preventing larger galaxies from forming stars, suppressing AGN accretion, and resulting in the cosmic downsizing that we observe.

There has been significant observational evidence of AGN feedback in action in galaxy clusters, primarily in the form of radio jets (Schawinski et al., 2007; Rafferty

et al., 2008; Fabian, 2012; Farrah et al., 2012; Page et al., 2012). Galaxies near the center of clusters show a boosted likelihood of hosting large radio-loud jets of AGN-driven material (Burns, 1990; Best et al., 2005; McNamara et al., 2005), whose energies are comparable to those needed to stop the gas from cooling (e.g., Simionescu et al., 2009). Furthermore, AGN feedback from the central cD galaxies in clusters increases in proportion to the cooling luminosity, as expected in an operational feedback loop (e.g., Bîrzan et al., 2004; Rafferty et al., 2006; Brüggen & Scannapieco, 2009).

Direct measurements of the characteristic heating of the interstellar medium (ISM) and surrounding IGM by AGN feedback have been more difficult due to the relatively high redshifts and faint signals involved. Broad absorption-line outflows (winds) are observed as blueshifted troughs in the rest-frame spectra of ≈20% of all of quasars (Hewett & Foltz, 2003; Ganguly & Brotherton, 2008; Knigge et al., 2008). However, quantifying AGN feedback requires estimating the mass-flux and the energy released by these outflows (e.g., Wampler et al., 1995; de Kool et al., 2001; Hamann et al., 2001; Feruglio et al., 2010; Sturm et al., 2011; Veilleux et al., 2013). These quantities, in turn, can only be computed in cases for which it is possible to estimate the distance to the outflowing material from the central source, which is often highly uncertain. While these measurements have been carried out for a select set of objects (e.g., Chartas et al., 2007; Moe et al., 2009; Dunn et al., 2010; Borguet et al., 2013; Chamberlain et al., 2015), it is still unclear how these results generalize to AGNs as a whole. At the same time it is still an open question whether AGN outflows triggered by galaxy interactions actually quench star formation in massive, high-redshift galaxies (e.g., Fontanot et al., 2009; Pipino et al., 2009; Debuhr et al., 2010; Ostriker et al., 2010; Faucher-Giguère & Quataert, 2012; Newton & Kay, 2013; Feldmann & Mayer, 2015).

A promising method for quantifying the effect of AGN feedback is through measurements of the cosmic microwave background (CMB) radiation. The CMB has large-scale anisotropies that have been measured in great detail and provide insight into the cosmological parameters that shape our universe (e.g., Planck Collaboration et al., 2015d). At angular scales smaller than ≈5 arcmin, though, Silk damping washes out the primary CMB anisotropies (Silk, 1968; Planck Collaboration et al., 2015d), leaving room for secondary anisotropies. These include the Sunyaev-Zel'dovich effect, where CMB photons are scattered by hot, ionized gas (Sunyaev & Zeldovich, 1970, 1972). If the gas is sufficiently heated, inverse Compton scattering will shift the CMB photons to higher energies. This thermal Sunyaev-Zel'dovich (tSZ) effect directly depends on the thermal energy of the free electrons that the CMB radiation passes through, and it has a unique spectral signature that makes it well suited to measuring the heating of gas and characterizing AGN feedback (Voit, 1994; Birkinshaw, 1999; Natarajan & Sigurdsson, 1999; Platania et al., 2002; Lapi et al., 2003; Chatterjee & Kosowsky, 2007; Chatterjee et al., 2008; Scannapieco et al., 2008; Battaglia et al., 2010). On the other hand, if an object is moving along the line of sight with respect to the CMB rest frame, then the Doppler effect will lead to an observed distortion of the CMB spectrum, referred to as the kinetic Sunyaev-Zel'dovich effect. The magnitude of this effect is proportional to the overall column depth of the gas times the velocity of the line of sight motion, and its spectral signature is indistinguishable from primary CMB anisotropies.

The expected tSZ distortion per source is too small to be detected by current instruments (e.g., Scannapieco et al., 2008), and so a stacking method must be applied to many sources in order to derive a significant signal from them. Chatterjee et al. (2010) found a tentative detection of quasar feedback using the Sloan Digital Sky Survey (SDSS) and Wilkinson Microwave Anisotropy Probe (WMAP), although it is

ambiguous how much of their detected signal is due to AGN feedback and how much is due to other processes (see Ruan et al., 2015). Hand et al. (2011) stacked >2300 SDSS-selected "luminous red galaxies" in data from the Atacama Cosmology Telescope (ACT) and found a $2.1\sigma - 3.8\sigma$ tSZ detection after selecting radio-quiet galaxies and binning them by luminosity. Gralla et al. (2014) stacked data from ACT at the positions of a large sample of radio AGN selected at 1.4 GHz to make a 5σ detection of the tSZ effect associated with the haloes that host active AGN. Greco et al. (2015) used Planck full mission temperature maps to examine the stacked tSZ signal of 188,042 "locally brightest galaxies" selected from the SDSS Data Release 7, finding a significant measurement of the stacked tSZ signal from galaxies with stellar masses above $\approx 2\times 10^{11} M_{\odot}$. Ruan et al. (2015) stacked Planck tSZ Compton-y maps centered on the locations of 26,686 spectroscopic quasars identified from SDSS to estimate the mean thermal energies in gas surrounding such $z \approx 1.5$ quasars to be $\approx 10^{62}$ erg. On the contrary, Cen & Safarzadeh (2015b) used a statistical analysis of stacked y maps of quasar hosts using the Millennium Simulation and found that, with the 10 arcmin full width at half maximum (FWHM) resolution of their Planck stacking process, the results of Ruan et al. (2015) could be explained by gravitational heating alone, with a maximum feedback energy of about 25% of their stated value. In addition, they found that a 1 arcmin FWHM beam is much more favorable in distinguishing between quasar feedback models. Crichton et al. (2016) stacked >17,000 radio-quiet quasars from SDSS in ACT data and found 3σ evidence for the presence of associated thermalized gas and 4σ evidence for the thermal coupling of quasars to their surrounding medium. These initial tSZ AGN feedback measurements using quasars are promising, and they continue to motivate direct measurements that probe different AGN feedback regimes, especially at the 1 arcmin FWHM resolution of the South Pole Telescope (SPT) used in this work.

Although quasars are a popular target for measuring AGN feedback due to their brightness and their active feedback processes, their drawbacks are that they are relatively scarce and contain contaminating emission that obscures the signatures of AGN feedback. In this paper, we focus on measuring co-added tSZ distortions in the CMB around massive ($\geq 10^{11} M_{\odot}$) quiescent elliptical galaxies at moderate redshifts ($0.5 \leq z \leq 1.5$) using data from the Blanco Cosmology Survey (BCS; Desai et al., 2012), VISTA Hemisphere Survey (VHS; McMahon, 2012), and South Pole Telescope SZ survey (SPT-SZ; Schaffer et al., 2011), in order to characterize the energy injected by the AGNs they once hosted. These galaxies contain almost no dust and are very numerous on the sky, making them well-suited for co-adding in large numbers in order to obtain good constraints on the energy stored in the gas that surrounds them.

The structure of this paper is as follows. In Section 2, we give an overview of the tSZ effect and provide a theoretical basis for our tSZ results. In Section 3, we describe the data that we use from the BCS, VHS, and SPT-SZ surveys. In Section 4, we describe our method of selecting optimal galaxies for our measurements. In Section 5, we describe how we generate a reliable catalog of sources and the parameters that describe their properties. In Section 6, we describe how we generate the final catalog of galaxies for our tSZ measurements. In Section 7, we describe our SPT-SZ filtering, the galaxy co-add process, and our overall results. This includes the initial measurements, χ^2 statistics using just the SPT-SZ data, χ^2 statistics incorporating Planck data, and a goodness-of-fit test using the Anderson-Darling (A-D) statistic. In Section 8, we summarize our results, discuss the implications for AGN feedback, and provide conclusions.

Throughout this work, we adopt a Λ cold dark matter cosmological model with parameters (from Planck Collaboration et al., 2015d), $h = 0.68$, $\Omega_0 = 0.31$, $\Omega_\Lambda = 0.69$, and $\Omega_b = 0.049$, where h is the Hubble constant in units of 100 km s^{-1} Mpc^{-1}, and

Ω_0, Ω_Λ, and Ω_b are the total matter, vacuum, and baryonic densities, respectively, in units of the critical density. All of our magnitudes are quoted in the AB magnitude system (i.e., Oke & Gunn, 1983).

2.2 Methods

2.2.1 The tSZ Effect

The tSZ effect describes the process by which CMB photons gain energy when passing through ionized gas (Sunyaev & Zeldovich, 1970, 1972). The photons are shifted to higher energies by thermally energetic electrons through inverse Compton scattering, and the resulting CMB anisotropy has a distinctive frequency dependence which causes a deficit of photons at frequencies below $\nu_{\rm null} = 217.6\,{\rm GHz}$ and an excess of photons above $\nu_{\rm null}$, with no change at $\nu_{\rm null}$. For the nonrelativistic plasma we will be interested in here, the change in CMB temperature as a function of frequency due to the tSZ effect is

$$\frac{\Delta T}{T_{\rm CMB}} = y\left(x\frac{e^x+1}{e^x-1} - 4\right), \tag{2.1}$$

where the dimensionless Compton-y parameter is defined as

$$y \equiv \int dl\, \sigma_T \frac{n_e k\,(T_e - T_{\rm CMB})}{m_e c^2}, \tag{2.2}$$

where σ_T is the Thomson cross section, k is the Boltzmann constant, m_e is the electron mass, c is the speed of light, n_e is the electron number density, T_e is the electron temperature, $T_{\rm CMB}$ is the CMB temperature (we use $T_{\rm CMB} = 2.725$ K), and the integral is performed over the line of sight distance l. Finally, the dimensionless frequency x is given by

$$x \equiv \frac{h\nu}{kT_{\rm CMB}} = \frac{\nu}{56.81\,{\rm GHz}}, \tag{2.3}$$

where h is the Planck constant.

We can calculate the total excess thermal energy associated with a source by integrating Equation (2.2) over a region of sky around the source as (e.g., Scannapieco et al., 2008; Ruan et al., 2015),

$$\int d\boldsymbol{\theta}\, y(\boldsymbol{\theta}) = \int d\boldsymbol{\theta} \int dl\, \sigma_T \frac{n_e k T_e}{m_e c^2} = \frac{\sigma_T}{m_e c^2} l_{\rm ang}^{-2} \int dV\, n_e k T_e, \tag{2.4}$$

where $\boldsymbol{\theta}$ is a two-dimensional vector in the plane of the sky in units of radians, $l_{\rm ang}$ is the angular diameter distance to the source, V is the volume of interest around the source, and we have restricted our attention to hot gas with $T_e \gg T_{\rm CMB}$. In Equation (2.4), the Compton-y integral has become a volume integral of the electron pressure (i.e. $P_e = n_e k T_e$), which is related to the associated thermal energy as

$$\int dV\, n_e k T_e = \left(\frac{2}{3}\right)\left(\frac{1+A}{2+A}\right) E_{\rm therm}, \tag{2.5}$$

where $A = 0.08$ is the cosmological number abundance of helium, and $E_{\rm therm}$ is the total thermal energy associated with the source: that gained from the initial collapse of the baryons, plus the contribution from the AGN, minus the losses due to cooling and the PdV work done during expansion. We can combine Equations (2.4) and (2.5) and solve for $E_{\rm therm}$ to get

$$\begin{aligned} E_{\rm therm} &= 2.9 \frac{m_e c^2}{\sigma_T} l_{\rm ang}^2 \int d\boldsymbol{\theta} y(\boldsymbol{\theta}) \\ &= 2.9 \times 10^{60} {\rm erg} \left(\frac{l_{\rm ang}}{\rm Gpc}\right)^2 \frac{\int d\boldsymbol{\theta} y(\boldsymbol{\theta})}{10^{-6}\,{\rm arcmin}^2} \end{aligned} \tag{2.6}$$

(we feel it worth noting that working out the units while going from the first to the second line of the above equation does indeed yield almost exactly 10^{60} erg). Finally, we can combine Equations (2.1) and (2.6) to get $E_{\rm therm}$ in terms of ΔT at a given dimensionless frequency x,

$$E_{\rm therm} = \frac{1.1 \times 10^{60} {\rm erg}}{x\frac{e^x+1}{e^x-1} - 4} \left(\frac{l_{\rm ang}}{\rm Gpc}\right)^2 \frac{\int \Delta T(\boldsymbol{\theta}) d\boldsymbol{\theta}}{\mu{\rm K\ arcmin}^2}. \tag{2.7}$$

2.2.2 Models of Gas Heating

To compare the energies and angular sizes above with the expectations from models of feedback, we can construct a simple model of gas heating with and without AGN feedback. To do this we first compute $R_{\rm vir}$, the virial radius of a (spherical) dark matter halo defined as the physical radius within which the density is 200 times the mean cosmic value. As a function of redshift z and mass M, this is

$$\begin{aligned} R_{\rm vir} &= \left[\frac{M}{(4\pi/3)200\Omega_0\rho_{\rm crit}(1+z)^3}\right]^{1/3} \\ &= 0.67\,{\rm Mpc}\,M_{13}^{1/3}(1+z)^{-1}, \end{aligned} \tag{2.8}$$

where $\rho_{\rm crit}$ is the critical density at $z = 0$, and M_{13} is the mass of the halo in units of $10^{13}M_\odot$. This can be compared to the angular scales above, using the fact that at an angular diameter distance of 1 Gpc, 1 arcminute corresponds to 0.29 Mpc.

If the gas collapses and virializes along with the dark matter, it will be shock-heated during gravitational infall to the virial temperature,

$$T_{\rm vir} = \frac{GM}{R_{\rm vir}}\frac{\mu m_p}{2k} = 2.4\times10^6{\rm K}\,M_{13}^{2/3}(1+z), \tag{2.9}$$

where G is the gravitational constant, m_p is the proton mass, and $\mu = 0.62$ is the average particle mass in units of m_p. If we approximate the gas distribution as isothermal at this temperature, its total thermal energy can then be estimated as

$$\begin{aligned} E_{\rm therm,gravity} &= \frac{3kT_{\rm vir}}{2}\frac{\Omega_b}{\Omega_0}\frac{M}{\mu m_p} \\ &= 1.5\times10^{60}\,{\rm erg}\,M_{13}^{5/3}(1+z). \end{aligned} \tag{2.10}$$

To relate the stellar masses of the galaxies we will be stacking to the dark matter halo masses, we can take advantage of the observed relation between black hole mass and halo circular velocity, v_c, from Ferrarese (2002, see also Merritt & Ferrarese, 2001; Tremaine et al., 2002), and convert the black hole mass to its corresponding bulge

dynamical mass using a factor of 400 (Marconi & Hunt, 2003). This gives

$$\begin{aligned} M_{\rm stellar} &= 6.6^{+5.5}_{-3.2} \times 10^{10}\, M_\odot \left(\frac{v_{\rm c}}{300\,{\rm km\ s^{-1}}}\right)^5 \\ &= 2.8^{+2.4}_{-1.4} \times 10^{10} M_\odot\, M_{13}^{5/3} (1+z)^{5/2}, \end{aligned} \tag{2.11}$$

where we have used the fact that $v_c = (GM/R_{\rm vir})^{1/2} = 254\,{\rm km\,s^{-1}}\, M_{13}^{1/3}(1+z)^{1/2}$, and taken $M_{\rm stellar} \propto v_c^{\alpha_c}$ with the power law index $\alpha_c = 5$, which is near the center of the allowed range of 5.4 ± 1.1, and we take our uncertainties from Ferrarese (2002). Substituting Equation (2.11) into Equation (2.10) gives

$$E_{\rm therm,gravity} = 5.4^{+5.4}_{-2.9} \times 10^{60}\,{\rm erg} \times \frac{M_{\rm stellar}}{10^{11} M_\odot} (1+z)^{-3/2}. \tag{2.12}$$

This is the total thermal energy expected around a galaxy of stellar mass $M_{\rm stellar}$ due purely to gravitational heating, and ignoring both radiative cooling, which will decrease $E_{\rm therm}$, and AGN feedback, which will increase it.

While there are many models of AGN feedback, each of which will lead to somewhat different signatures in our data, we can estimate the overall magnitude of this effect by making use of the simple model described in Scannapieco & Oh (2004, see also Thacker et al., 2006; Scannapieco et al., 2008). In this case, AGN feedback is described as tapping into a small fraction, ϵ_k, of the total bolometric luminosity of the AGN to heat the surrounding gas. In particular, black holes are assumed to shine at the Eddington luminosity (1.2×10^{38} erg s^{-1} $M_\odot^{-1}$) for a time $0.035\, t_{\rm dynamical}$, where

$$t_{\rm dynamical} \equiv R_{\rm vir}/v_c = 2.6\,{\rm Gyr}\,(1+z)^{-3/2}. \tag{2.13}$$

This choice of timescale gives a good match to the observed evolution of the quasar luminosity function (Wyithe & Loeb, 2002, 2003; Scannapieco & Oh, 2004). This gives

$$E_{\rm therm,feedback} = 4.1 \times 10^{60}\,{\rm ergs}\,\epsilon_{k,0.05} \times \frac{M_{\rm stellar}}{10^{11} M_\odot}\,(1+z)^{-3/2}. \tag{2.14}$$

Here $\epsilon_{k,0.05} \equiv \epsilon_k/0.05$, such that the kinetic energy input is normalized to a typical value needed to achieve antiheirarchical galaxy evolution through effective feedback (e.g., Scannapieco & Oh, 2004; Thacker et al., 2006; Costa et al., 2014). Note that the uncertainty in this equation is completely dominated by the $\epsilon_{k,0.05}$ term, which is uncertain to within an order of magnitude.

This energy input is equal in magnitude to the errors in $E_{\rm therm,gravity}$, meaning that the differences between models with and without AGN feedback will not be dramatic. Thus only detailed simulations will be able to make precise predictions on the level needed to rule out or lend support to a particular model of AGN feedback. Although carrying out such simulations is beyond the scope of this paper, Equations (2.12) and (2.14) are roughly consistent with such sophisticated models (e.g., Thacker et al., 2006; Chatterjee et al., 2008), meaning that they can be used as an approximate guide to interpreting our results. Thus, we will use them to provide a general context for thinking about our observational results in terms of AGN feedback.

Finally, we note that the sound speed c_s of the gas in the gravitationally heated case is similar to the circular velocity (i.e., $c_s = [\gamma kT/(\mu m_p)]^{1/2} = (\gamma/2)^{1/2} v_c$, where γ is the adiabatic index), and the expected energy input from the AGN is similar to the energy input from gravitational heating. This means that the energy input from the AGN will take a timescale $\approx t_{\rm dynamical}$ to impact gas on the scale of the halo, and it is unlikely to affect scales much larger than $\approx 2R_{\rm vir}$. These sizes and timescales mean that at the moderate redshifts we will be exploring, the majority of the gas heating we are interested in will occur on scales $\lesssim 2$ arcmin.

2.3 Data

Three public datasets are critical to our analysis. To detect, measure, and select galaxies, we use optical and infrared data from the BCS (Desai et al., 2012) and

Filter	Center [nm]	Width [nm]	Depth [AB]	Seeing [FWHM]	Survey
g	481.3	153.7	23.9	1.0 arcsec	BCS
r	628.7	146.8	24.0	1.0 arcsec	BCS
i	773.2	154.8	23.6	0.8 arcsec	BCS
z	940.0	200.0	22.1	0.9 arcsec	BCS
J	1252	172.0	20.86	1.1 arcsec	VHS DES
H	1645	291.0	20.40	1.0 arcsec	VHS DES
K_s	2147	309.0	20.16	1.0 arcsec	VHS DES
150GHz	153.4 GHz	35.2 GHz	17 μK-arcmin	1.15 arcmin	SPT-SZ
220GHz	219.8 GHz	43.7 GHz	41 μK-arcmin	1.05 arcmin	SPT-SZ

Table 2.1: Band/filter information. BCS depths are 10σ AB magnitude point source depths; VHS depths are 5σ median AB magnitude depths; SPT depths use a Gaussian approximation for the beam. The BCS information is taken from http://www.ctio.noao.edu/noao/content/MOSAIC-Filters and Desai et al. (2012), the VHS information from http://casu.ast.cam.ac.uk/surveys-projects/vista/technical/filter-set and McMahon (2012), and the SPT information from Schaffer et al. (2011).

infrared data from the VHS (McMahon, 2012). To stack microwave observations to detect the tSZ signal, we use data from the SPT-SZ survey (Schaffer et al., 2011). The three datasets overlap over an area of $\approx$43 deg^2, as can be seen in Figure 2.1, and provide good wavelength coverage and sensitivities, as can be seen in Table 2.1. Here we describe each of these data sets in turn.

2.3.1 The BCS

The BCS was a National Optical Astronomy Observatory (NOAO) Large Survey project that observed $\approx$80 deg^2 of the southern sky over 60 nights between 2005 November and 2008 November on the 4m Víctor M. Blanco telescope at the Cerro Tololo Inter-American Observatory in Chile using the Mosaic II imager with g, r, i,

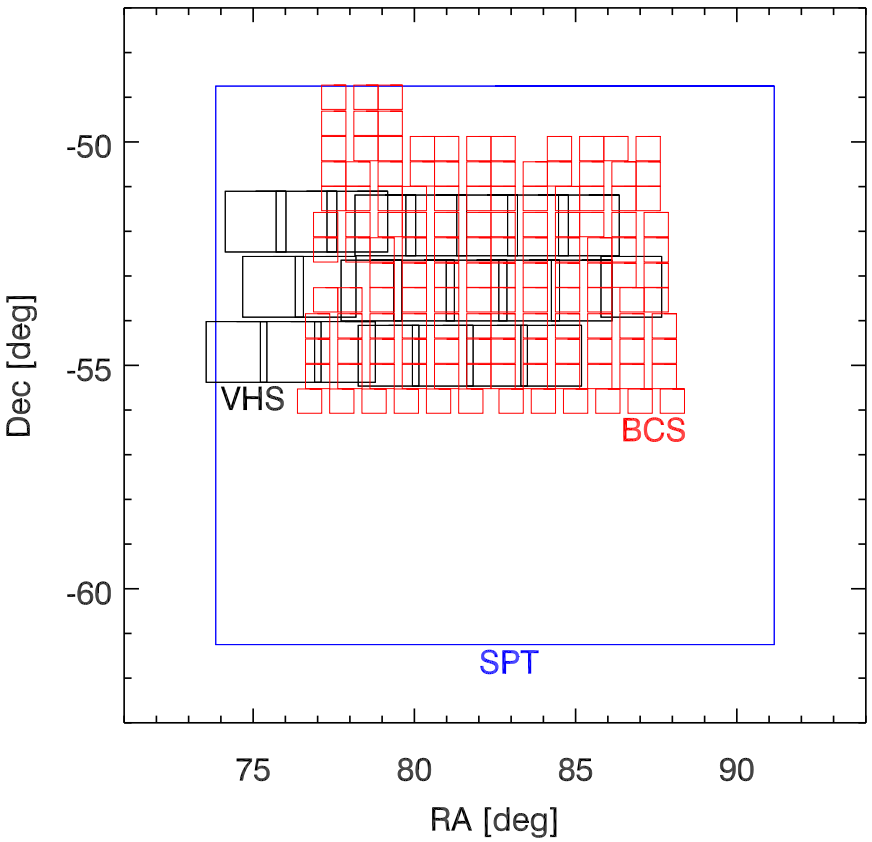

Figure 2.1: Approximate locations on the sky for the overlapping BCS tiles (red), VHS tiles (black), and SPT-SZ field (blue).

and z bands (Desai et al., 2012). The filter centers, effective widths, and magnitude limits are given in Table 2.1.

The BCS data is split up into many smaller 36 × 36 arcmin (8192 × 8192 pixel) images called tiles, with ≈1 arcmin overlap between neighboring tiles. Each pixel subtends 0.27 arcsec on the sky. As described in Desai et al. (2012), each raw data tile is put through a detrending pipeline, which consists of crosstalk corrections, overscan, flatfield, bias and illumination correction, and astrometric calibration. The average FWHM of the seeing disk in the single epoch images ranges between 0.7 and 1.6 arcsec. Each tile is then put through a co-addition pipeline that combines data taken over the same locations on the sky to build deeper single images. This results

in a co-added tile image and an inverse-variance weightmap (confidence image) for each tile region of the survey. We use the area of the BCS that overlaps with the VHS and SPT-SZ, known as the *5 hr field* (referring to its right ascension). This dataset consists of 135 tiles and their associated weightmaps for each band, covering ≈45 deg^2.

2.3.2 The VHS

The VHS is a large-scale near-infrared survey whose goal is to survey the entire southern celestial hemisphere (≈20,000 deg^2; McMahon, 2012). The survey component in which we are interested is called the VHS DES (DES because it overlaps with the Dark Energy Survey), a 5000 deg^2 region that is imaged with 120 s exposure times in the J, H, and K_s bands (see Table 2.1). The data was obtained from 2009 to 2011 on the 4.1 m Visible and Infrared Survey Telescope for Astronomy (VISTA) at the Paranal Observatory in Chile.

The VHS data is split up into ≈2 × 1.5 deg (≈12,770 × 15,660 pixel) tiles. Each pixel subtends 0.33 arcsec on the sky. As described on the VISTA data processing web page,[2] the raw VHS data go through a pipeline that involves reset correction, dark correction, linearity correction, flat field correction, sky background correction, destripe, jitter stacking, astrometric and photometric calibration, and tile generation. Tiles are generated from six smaller, stacked pawprints, each containing 16 even smaller detector-level images,[3] and the median image seeing as measured from stellar FWHM on VHS pawprints ranges from 0.89 arcsec in K_s to 0.99 arcsec in J. The stacked paw prints then result in a science-ready tile image and inverse-variance weightmap for each tile region of the survey. We are interested in the area of the

[2]http://casu.ast.cam.ac.uk/surveys-projects/vista/technical/data-processing

[3]http://casu.ast.cam.ac.uk/surveys-projects/vista/technical/tiles

VHS that overlaps with the BCS (see Figure 2.1). This results in 20 tiles and their associated weightmaps, covering ≈ 55 deg^2.

2.3.3 The SPT-SZ Survey

The SPT-SZ survey (Schaffer et al., 2011) used the 10m SPT at the National Science Foundation's (NSF) Amundsen-Scott South Pole Station to survey a large area of the sky at millimeter and sub-millimeter wavelengths with arcminute angular resolution and low noise (Ruhl et al., 2004; Padin et al., 2008; Carlstrom et al., 2011). The survey observed 2500 deg^2 of the southern sky during the austral winter seasons of 2008 through 2011. Data from the 2011 release that we are using covers $\approx$95 deg^2 to a depth of 17 and 41 μK arcmin at 150 GHz and 220 GHz, respectively, centered at (R.A., decl.) = (82.7, -55) degrees (see Table 2.1).

The SPT-SZ data is contained in a single image per band, $\approx 20^\circ \times 10^\circ$ ($\approx$3000 $\times$ 3000 pixels) projected as either a Sanson-Flamsteed projection or an oblique Lambert equal-area azimuthal projection. The Sanson-Flamsteed projection is most useful for cluster-finding and contains masked point-sources, while the Lambert projection is most useful for point-source analysis. Since we are interested in individual sources that are undetected and within the noise level, we use the Sanson-Flamsteed projection with point-sources masked. Each pixel subtends 15 arcsec on the sky. As described in Schaffer et al. (2011), the raw data goes through a pre-processing stage where the data from a single observation of the field is calibrated, data selection cuts are applied, and initial filtering and instrument characterization are performed. A map-making stage with additional filtering is performed on the pre-processed data and the data are binned into single-observation maps used for final co-adds. The final data products include a co-added image, two-dimensional beam functions, filter transfer functions, and noise power spectral densities for each band.

It is worth noting that 220 GHz is very close to the frequency at which there is no change in the CMB due to the tSZ effect ($\nu_{\rm null}$ = 217.6 GHz), while 150 GHz, which is close to the peak of the undistorted CMB spectrum (160 GHz), will see a decrement in radiation. Equations (2.1) and (2.3) can be rewritten for these bands, though the equations must now involve integration over the SPT filter curves. Once this is done, we can write the Compton-y parameter as

$$y = -0.41\,\frac{\Delta T_{150}}{1\mathrm{K}} \qquad \text{and} \qquad y = 9.9\,\frac{\Delta T_{220}}{1\mathrm{K}}, \tag{2.15}$$

where ΔT_{150} and ΔT_{220} are the temperature anisotropies at 150 and 220 GHz, respectively. Here we can explicitly see that, for the same y, the increase in ΔT_{220} is about 24 times less than the decrease in ΔT_{150}. A measurement of the tSZ effect is therefore expected to give us a clear decrement at 150 GHz and no detectable change at 220 GHz.

We can also use Equations (2.3) and (2.7), integrated over the SPT filter curve as mentioned above, to compare the tSZ decrement at 150 GHz to the total thermal energy of an object as

$$E_{\rm therm} = -1.2 \times 10^{60}\mathrm{ergs}\left(\frac{l_{\rm ang}}{\mathrm{Gpc}}\right)^2 \frac{\int \Delta T_{150}(\boldsymbol{\theta}) d\boldsymbol{\theta}}{\mu\mathrm{K\ arcmin}^2}. \tag{2.16}$$

Given the arcminute angular resolution and 17 μK arcmin sensitivity of the SPT 150 GHz data, this means that for stacks of several thousand sources we can hope to derive constraints on the order of $\Delta E_{\rm therm} \approx 10^{60}$ erg. This is sufficient to derive constraints that are interesting for discriminating between models of AGN feedback, as discussed in Section 2.2.2.

2.4 Selecting Galaxies to Constrain AGN Feedback

If we compare Equation (2.6) with (2.12) and (2.14), we can see that achieving constraints on $E_{\rm therm}$ at the level to discriminate between the models above requires

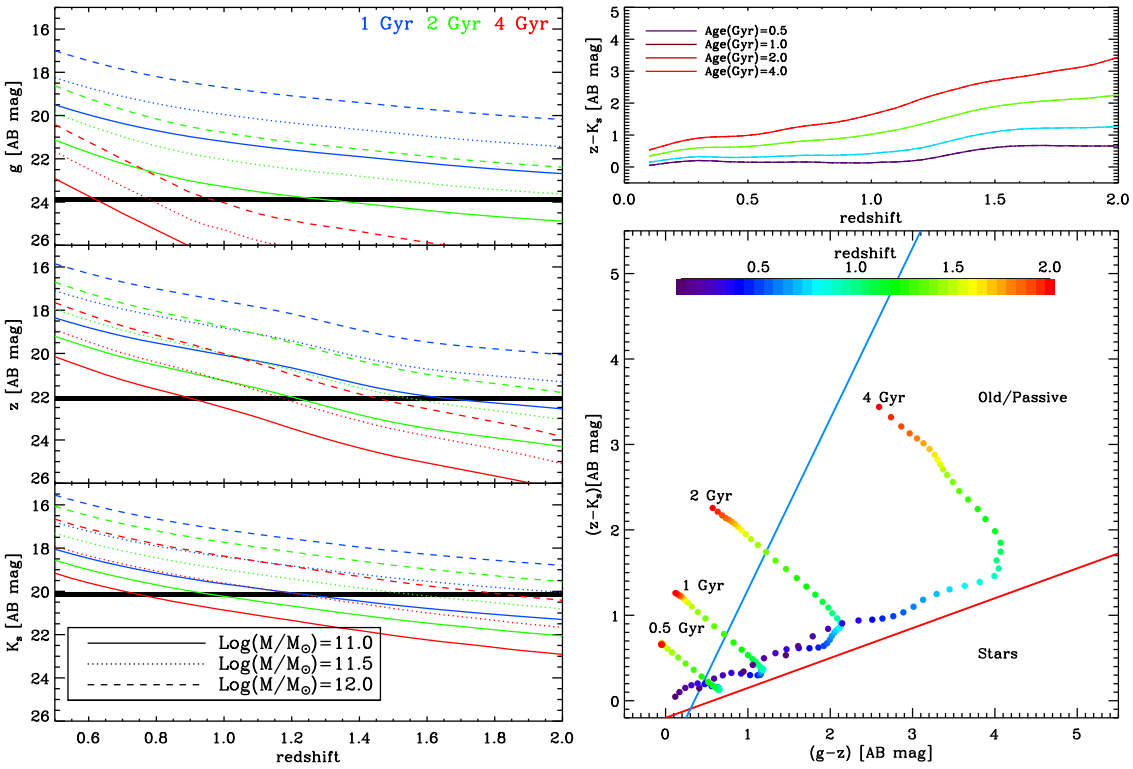

Figure 2.2: Left: Optical and infrared magnitudes of early-type galaxies as a function of mass (indicated by line type), age (indicated by color), and redshift, as compared with limits from VHS (K_s) and BCS (g, z; solid black lines). Upper-right: Color-redshift plot showing how age and redshift are distinguished in a galaxy's $z-K_s$ color. Lower-right: Color-color plot illustrating how passive $z \geq 0.5$ galaxies are easily distinguished from stars and young galaxies. The red and blue lines represent Equations (2.17) and (2.18), respectively.

measurements with sensitivities on the order of $\int d\boldsymbol{\theta} y(\boldsymbol{\theta}) \approx 10^{-6}\,\mathrm{arcmin}^2$. With current instruments at arcminute resolution, this requires stacking $\gtrsim 1000$ sources. Thus, the first step to constraining AGN feedback is selecting an appropriate set of objects around which to co-add CMB data. Here we must balance several competing concerns.

At the earliest times, when the most luminous AGNs are in the midst of heating the surrounding gas, tSZ measurements are particularly difficult. This is both because emission from the AGN and its host are likely to contribute in the interesting 100-300 GHz frequency range, as well as because the low number density of such sources

makes it very difficult to co-add them in meaningful numbers using the SPT data we are working with (although with a large field and spectral energy distribution (SED) fitting it is possible to extract a tSZ signal, i.e. Gralla et al., 2014). On the other hand, the cooling times of regions heated by the most luminous AGNs are likely to be longer than the Hubble time (e.g., Scannapieco & Oh, 2004), making the heated gas we are interested in detectable long after the active AGN phase has passed. Furthermore, at the lowest redshifts, the largest bulge galaxies will be absorbed into galaxy clusters, where gravitational heating effects will be sufficiently large as to make AGN feedback processes difficult to distinguish.

For these reasons, we restrict our attention to elliptical galaxies, rather than luminous AGNs or dusty late-type galaxies, and select only galaxies with redshifts greater than $z = 0.5$. The left panel of Figure 2.2 illustrates the g, z, and K_s band magnitudes of ellipticals as a function of age and mass, computed from GALAXEV population synthesis models (Bruzual & Charlot, 2003; for band information see Table 2.1). Here we have taken a star formation history $\propto \exp(-t/\tau)$, where $\tau = 0.51$ Gyr, and ages of 1, 2, and 4 Gyr. Note that in the standard cosmology, the ages of the universe at $z = 0.5$, 1, 1.5, and 2.0 are 8.5, 5.9, 4.3, and 3.3 Gyr, respectively.

In Figure 2.2 we have also plotted the magnitude limits of the BCS and VHS data. By comparing the models and limits we can see that large passive galaxies are indeed detectable in this data at a wide range of redshifts above $z = 0.5$. In particular, galaxies with ages $\approx$1 Gyr with stellar masses above $10^{11}\,M_\odot$ are detectable in both the optical and infrared data from $z = 0.5$ to 1.2 while 1 Gyr galaxies with stellar masses above $10^{11.5}\,M_\odot$ are detectable out to $z = 2$. At ages of 2 Gyr, galaxies with stellar masses above $10^{11}\ M_\odot$ are detectable out to $z = 1.0$ and galaxies with stellar masses above $10^{11.5}\ M_\odot$ are detectable out to $z = 1.6$. Finally, for an age of 4

Gyr, galaxies with stellar masses above $10^{11}\,M_{\odot}$ can be detected out to $z = 0.7$, and galaxies with stellar masses above $10^{11.5}\,M_{\odot}$ can be detected out to $z = 1.2$.

The right panel of Figure 2.2 shows that we can also use $g - z$ vs. $z - K_s$ colors to cleanly separate $\gtrsim 1$ Gyr old galaxies at $0.5 \leq z \leq 1.5$ from stars and star-forming systems, making use of the gzK_s method outlined in Arcila-Osejo & Sawicki (2013) (see also Daddi et al., 2004; Cameron et al., 2011). In particular, by applying a cut

$$(z - K_s) \geq 0.35(g - z) - 0.2, \tag{2.17}$$

where g, z, and K_s are AB magnitudes, we are able to separate the galaxies we are interested in from Galactic stars. Furthermore, by applying a cut

$$(z - K_s) \leq 2(g - z) - 0.7, \tag{2.18}$$

we can also separate passively evolving galaxies from young galaxies over the full redshift range in which we are interested. Taken together, these results make clear that if we focus on the redshift range $0.5 - 1.5$, we should be able to efficiently select a large number of suitable galaxies from the BCS and VHS data that we are using.

2.5 Creating a Catalog of Galaxies

2.5.1 Image Matching

As seen in Figure 2.2, the sources we are interested in are brightest in the K_s band, and thus we use it to make all of our detections. Because the BCS and VHS tiles are different sizes and in different locations (see Figure 2.1), we consider every possible overlap between images when aligning the other data to the K_s tiles. We then match pixel sizes and locations, and to insure that fixed aperture flux measurements are consistent between bands, we also match the seeing between the K_s tiles and the other bands.

If the K_s tile has worse seeing than the other band, we simply degrade the other image with a Gaussian filter until it matches the FWHM of the K_s image. On the other hand, if the K_s image has better seeing, we degrade it to match the other band, compute the ratio of 3 arcsec diameter aperture fluxes between the two bands described below, and finally multiply the ratio by the 3 arcsec diameter flux measured from the unconvolved K_s. That is, we compute and apply an aperture correction as $\mathrm{Flux}_{grizJH} = \mathrm{Flux}_{grizJH,0} \times (\mathrm{Flux}_{K_s,0} \,/\, \mathrm{Flux}_{K_s,\mathrm{degraded}})$, where 0 denotes the non-degraded measurement. This is done to preserve both accurate colors and the best possible K_s flux in every case, since that is the most important band for our purposes. Note that, since the seeing is nearly the same for all tiles ($\approx$1 arcsec, see Table 2.1), this correction is minor, with a mean ratio ($\mathrm{Flux}_{K_s,0}$ / $\mathrm{Flux}_{K_s,\mathrm{degraded}}$) of 1.026 across all tiles.

2.5.2 Detecting and Measuring Sources

To detect and measure every object in our field, we use the SExtractor software package, version 2.8.6 (Bertin & Arnouts, 1996).[4,5] The code detects and measures sources in an image through the following five-step process: (i) it creates a background map that estimates the noise at every pixel in the image; (ii) it detects sources using a thresholding technique; (iii) it uses a multiple isophotal analysis technique to deblend objects; (iv) it throws out spurious detections made in the wings of larger objects; and (v) it estimates the flux of each remaining object. Each of these steps can be adjusted by the user through configuration parameters, and we list our choice of these parameters for both BCS and VHS tiles in Table 2.2.

[4]SExtractor v2.13 User's manual, E. Bertin

[5]http://www.astromatic.net/software/sextractor

Configuration parameter	Value	Configuration parameter	Value
DETECT_TYPE	ccd	PHOT_AUTOPARAMS	2.5,3.5
DETECT_MINAREA	4	PHOT_AUTOAPERS	0.0,0.0
THRESH_TYPE	relative	SATUR_LEVEL	32,000 (VHS)
DETECT_THRESH	3.0	···	20,000 (BCS)
ANALYSIS_THRESH	3.0	GAIN	4.2 (VHS)
FILTER	y	···	0 (BCS)
FILTER_NAME	gauss_3.0_3x3.conv	PIXEL_SCALE	0
DEBLEND_NTHRESH	32	BACKPHOTO_TYPE	local
DEBLEND_MINCONT	0.005	BACKPHOTO_THICK	24
CLEAN	y	BACK_TYPE	auto
CLEAN_PARAM	1.0	BACK_VALUE	3.0
MASK_TYPE	correct	BACK_SIZE	64
WEIGHT_TYPE	map_weight	BACK_FILTERSIZE	3
WEIGHT_GAIN	n	BACK_FILTERTHRESH	0.0
RESCALE_WEIGHTS	y	MEMORY_OBJSTACK	10,000
PHOT_APERTURES	9	MEMORY_PIXSTACK	1,500,000

Table 2.2: SExtractor input parameters for all K_s-aligned tiles.

In all cases, we use SExtractor's dual-image mode, which allows us to make flux measurements in all bands from the same sources detections in the K_s band. This results in a catalog of K_s-detected sources with MAG_AUTO and 3 arcsec diameter aperture flux measurements in every band. We use corrected MAG_AUTO for our final catalogs and the 3 arcsec diameter aperture MAG_APER to compute aperture corrections as described in Section 2.5.1. Finally, the overlap between tiles within both the BCS and VHS images leads to some sources being detected in multiple tiles. To correct for this, we match our catalog with itself and remove multiple occurrences of sources within 1 arcsec of each other. At this point in the analysis, our full catalog contains

565,561 sources, 168,944 (30%) of which are identified as duplicates. This leaves 396,617 total sources.

To confirm the reliability of our measurements, we compare our J, H, and K_s magnitudes with the source catalog released with the public VHS data. In particular, we select stars from our catalog using Equation (2.17), with $<$ instead of $\geq$, and SExtractor `FLAGS` $= 0$ and match them with a random 10,000 source subset of the pre-made VHS catalog, where we define a match as two sources within 0.5 arcsec of each other. Note that our magnitudes are measured within 3 arcsec diameter apertures while the pre-made catalog uses 2.83 arcsec diameter apertures. A plot of the difference in magnitudes between our catalog and the pre-made VHS catalog can be seen in Figure 2.3. To remove extreme outliers, magnitudes from both catalogs are cut at the depths given in Table 2.1. The mean offsets from 0 in the magnitude differences are -0.11, -0.05, and -0.03 mag for J, H, and K_s, respectively. The mean photometric uncertainty in those offsets across all magnitudes are $\pm$0.09, $\pm$0.12, and $\pm$0.18 mag, respectively. The solid lines in Figure 2.3 represent the mean uncertainty within magnitude bins of width 1 mag, and they are plotted as positive offsets from 0 on the y-axis. The uncertainty includes any differences in the measurement process between this paper and McMahon (2012), as well as the inherent uncertainty in the SExtractor measurements. As can be seen, the difference in magnitudes is reasonably within the uncertainty.

We are not able to carry out a similar comparison for the BCS bands because the data do not come with reliable zeropoints, which are required to convert the measured image-level fluxes to actual fluxes. Instead, we compute the BCS band zeropoints ourselves using the stellar locus regression (SLR) code Big MACS (Kelly et al., 2014).[6] This code calibrates the photometric zeropoints by creating a model

[6] code.google.com/p/big-macs-calibrate

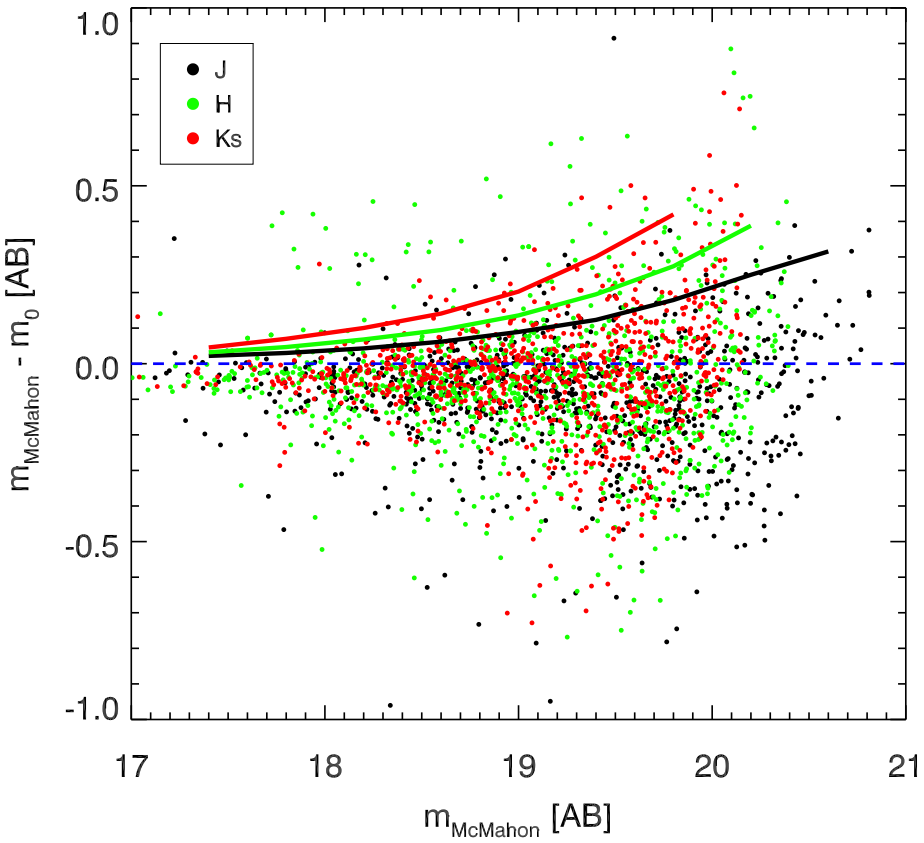

Figure 2.3: Comparison between our VHS-band measurements (m_0) and measurements from the catalog that came with the VHS data ($m_{McMahon}$; McMahon, 2012) for a random subset of ≈900 stars. J is shown in black, H in green, and K_s in red. Solid lines represent the mean y-axis errors (shown as an offset from 0), as a function of $m_{McMahon}$ in bins of 1 mag. These represent the uncertainty expected in comparing the two catalogs.

stellar locus for every input filter and fitting them simultaneously to a selection of input stars. To input the best possible selection of stars for this purpose, we use a combination of several criteria that are fine-tuned for each tile to balance between quality and quantity. These include selecting stars using Equation (2.17), SExtractor `FLAGS` $= 0$, `CLASS_STAR` ≥ 0.9, `A_IMAGE/B_IMAGE` ≥ 0.8, `FWHM_IMAGE` within a certain range from the point-source limit, and selecting bright, but unsaturated fluxes.

Our star selection results in a mean of 525 stars used per tile. We run the code using the BCS bands (g, r, i, z) plus J and H. Since the VHS bands (J, H, K_s)

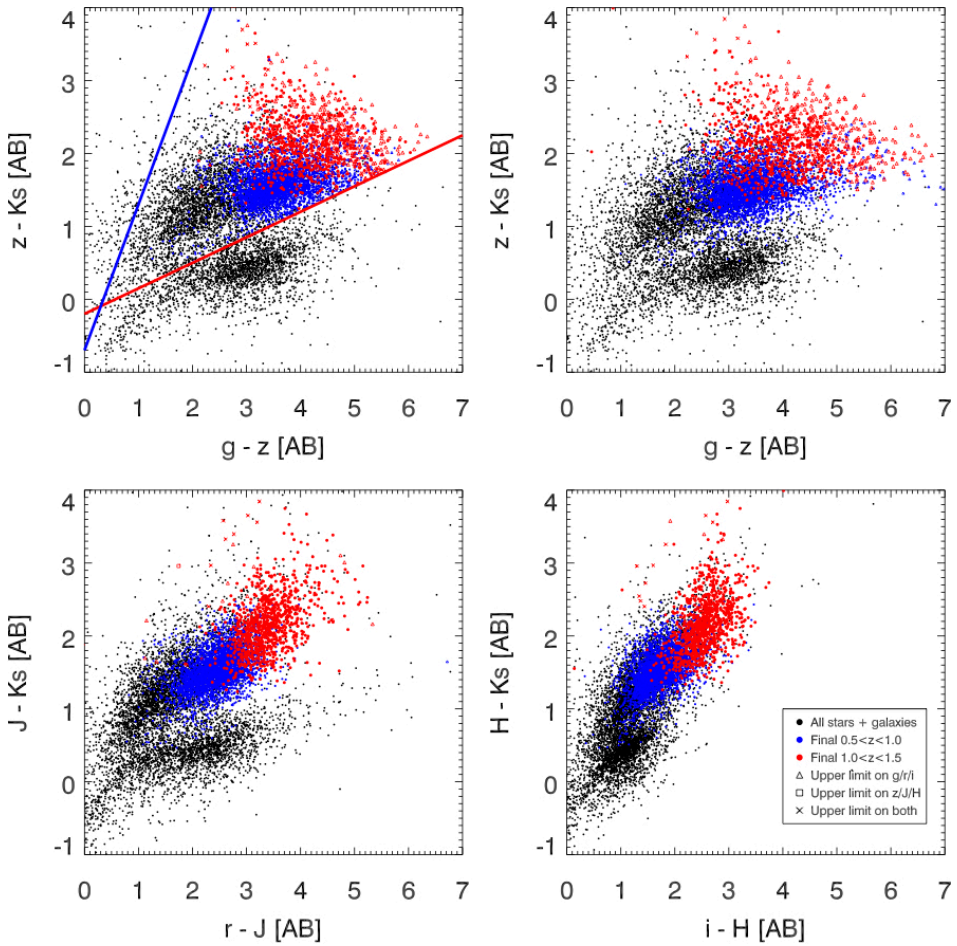

Figure 2.4: Color-color plots of a random 1/50th of the total sources described in Section 2.5.3 (black), our final $0.5 \leq z \leq 1.0$ galaxies (blue), and our final $1.0 \leq z \leq 1.5$ galaxies (red). Upper left: gzK_s plot with no correction for Galactic dust extinction, showing the cuts described in Section 2.4. Notice the clear distinction between stars (sources below the red line) and galaxies (sources above the red line). Upper right: gzK_s plot where galaxies have been corrected for Galactic dust extinction. Lower left: rJK_s plot where galaxies have been corrected for Galactic dust extinction. Lower right: iHK_s plot where galaxies have been corrected for Galactic dust extinction.

already have accurate zeropoints, we use the code to compute the zeropoints of the other 5 bands relative to H. This allows us to do an independent check on the code by comparing the code's value for the J zeropoint with the actual J zeropoint. We find that the mean difference between the two is 0.0078 mag, which is close to the

uncertainty of the code. The mean uncertainties in the derived zeropoint calibrations are 0.043, 0.037, 0.018, 0.012, and 0.0052 mag for g, r, i, z, and J, respectively.

2.5.3 Photometric Fitting

Having obtained a calibrated catalog of sources, we then apply an initial set of cuts to remove cases that are too uncertain to be suitable for stacking. Our goal here is not to select a statistically complete set of large, old, passive, $z \geq 0.5$ galaxies in the survey area, but rather to select a subset of such galaxies that can be cleanly identified. To count any source as reliable, we first require that it triggers no SExtractor output flags (`FLAGS` $= 0$). This choice excludes: (i) sources that have neighbors bright enough to bias the photometry; (ii) sources that were originally blended with another source; (iii) sources with at least one saturated pixel; (iv) sources with incomplete or corrupted data; and (v) sources for which a memory overflow occurred when measuring their flux. Furthermore, we remove all sources with a measured `FLUXERR_APER` ≤ 0 in any band, and any source within $3 \times$ `FWHM_IMAGE` from the edge of a tile, since the data become unreliable near these boundaries due to dithering.

Next, we separate stars from galaxies by making use of the gzK_s method given by Equation (2.17). As in the plot of model galaxies (lower-right panel of Figure 2.2), our data (Figure 2.4) shows a clear division between the galaxy locus and the stellar locus along this limit. Note however that Arcila-Osejo & Sawicki (2013) proposed a star cut of $(z - K_s) < 0.45(g - z) - 0.57$, which differs from ours slightly. Furthermore, we apply Equation (2.18) to separate out young, lower-redshift galaxies from the $z \geq 0.5$ old, passive galaxies we are interested in. After applying these criteria, we are left with a catalog of 332,037 sources consisting of 123,567 stars (37%) and 208,470 galaxies (63%), 195,426 (59%) of which satisfy Equation (2.18). We then correct for Galactic dust extinction using the Schlegel et al. (1998) dust map and the extinction

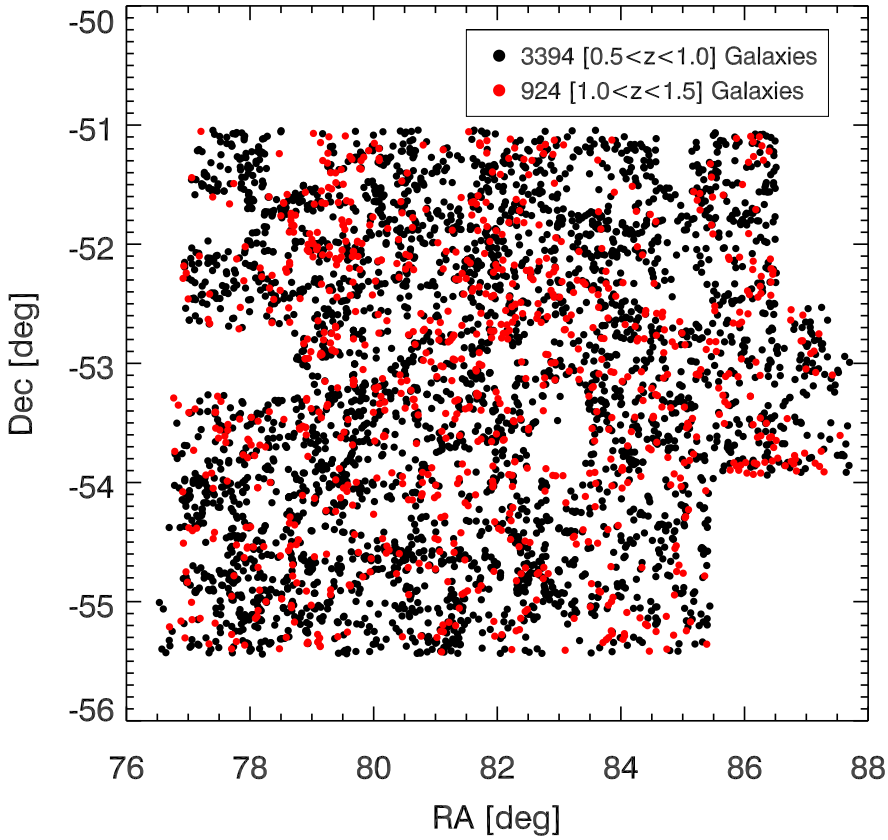

Figure 2.5: Sky distribution of our final selected galaxies for $0.5 \leq z \leq 1.0$ (black) and $1.0 < z \leq 1.5$ (red).

curve of Fitzpatrick & Massa (1999). Source-count histograms of the K_s magnitudes for stars and the corrected K_s magnitudes for galaxies are shown by the solid black and dashed blue lines, respectively, in Figure 2.6.

With our catalog of galaxies we use the EAZY software package (Brammer et al., 2008) to estimate photometric redshifts and the FAST software package (Kriek et al., 2009) to estimate various characteristics such as redshift, age, mass, and star formation rate (SFR). First, EAZY steps through a grid of redshifts, fits linear combinations of template spectra to our photometric data, and ultimately finds the best estimate for redshift, including optional flux- and redshift-based priors. We allow for fits to make use of linear combinations of up to two of the default template spectra, and also apply

the default K-band flux- and redshift-based prior derived from the GOODS-Chandra Deep Field-South (Wuyts et al., 2008).

The resulting redshifts are then fed into the FAST code, along with our seven-band photometric data, to fit for six additional parameters: age, mass, star formation timescale τ, SFR, dust content, and metallicity. FAST allows for a range of parameters when generating model fluxes, and in this analysis we choose: (i) a stellar population synthesis model as in Conroy & Gunn (2010); (ii) a Chabrier (2003) initial stellar mass function; (iii) an exponentially declining star formation history $\propto \exp(-t/\tau)$; and (iv) a dust extinction law as given by Kriek & Conroy (2013). To determine the best-fit parameters, the code simply determines the χ^2 of every point of the model cube and finds the minimum. While the code allows for confidence intervals calibrated using Monte-Carlo simulations, here we simply make use of the best-fit values for each galaxy, recording its χ^2 for use in our final galaxy selections, described in Section 2.6.

2.6 Final Galaxy Selection

To select the final galaxies used to measure the tSZ signal, we first cut out the least reliable FAST model fits by requiring $\chi^2 \leq 5$. Motivated by Sections 2.2.2 and 2.4, we then select galaxies with ages ≥ 1 Gyr and masses $\geq 10^{11} M_{\odot}$. To remove any presently star-forming galaxies, we also require the specific star formation rate SSFR $\equiv$ SFR/mass ≤ 0.01 Gyr^{-1} (Kimm et al., 2012). This insures that we select massive, old, and quiescent galaxies. We further split the resulting galaxies into two redshift ranges, $0.5 \leq z \leq 1.0$ ("low-z") and $1.0 < z \leq 1.5$ ("high-z"). Applying these constraints results in 4537 galaxies at low-z and 1259 galaxies at high-z.

Our final step is to remove any galaxies known to be a likely contamination to the tSZ signal we are interested in, due to: (i) the presence of a dusty Galactic molecular

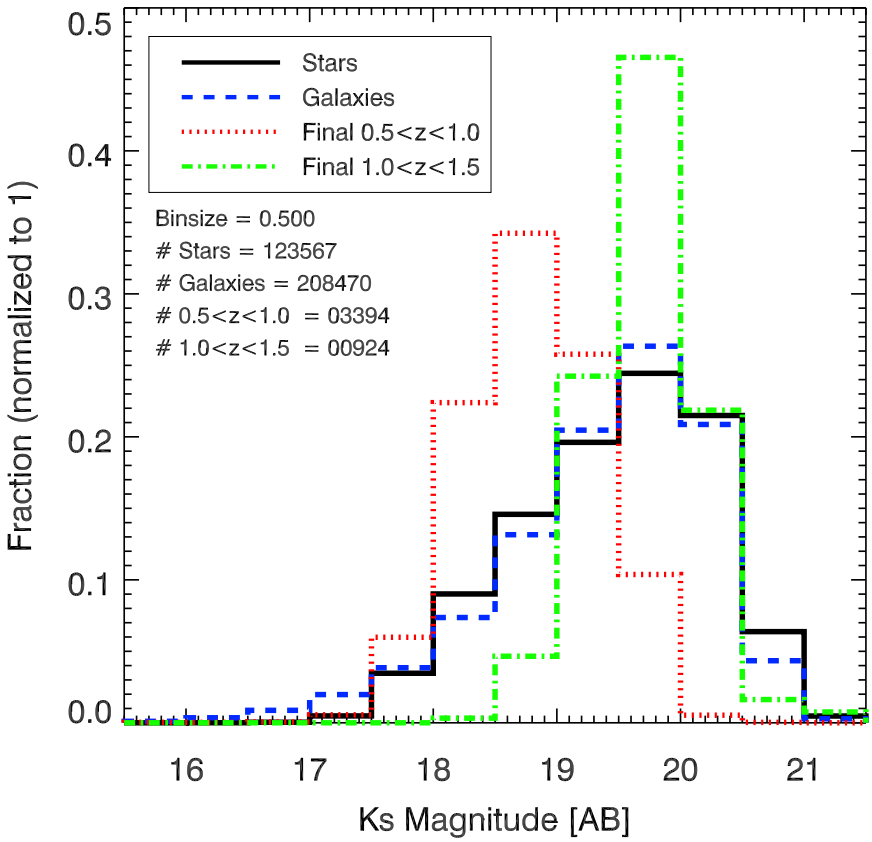

Figure 2.6: Normalized K_s band magnitude histograms of our identified stars (black solid), galaxies (blue dashed), and final selected galaxies at low redshift (dotted red line) and high redshift (dotted-dashed green line). Galaxy magnitudes have been corrected for dust extinction, as discussed in Section 2.5.3.

cloud; (ii) the presence of an AGN; (iii) the presence of a galaxy with strong dust emission; or (iv) the presence of a galaxy cluster, such that the tSZ signal would be dominated by the intracluster medium rather than the circumgalactic medium in which we are interested. Thus, we cut out any galaxy that is within 4 arcmin of any source found within a large number of external source catalogs, chosen to remove all such sources. Regarding these external source catalogs, to exclude the presence of Galactic molecular clouds, we remove sources correlated with the Planck Catalogue of Galactic Cold Clumps (Planck Collaboration et al., 2015f). To exclude the presence of bright AGN, we remove sources correlated with the ROSAT All-Sky

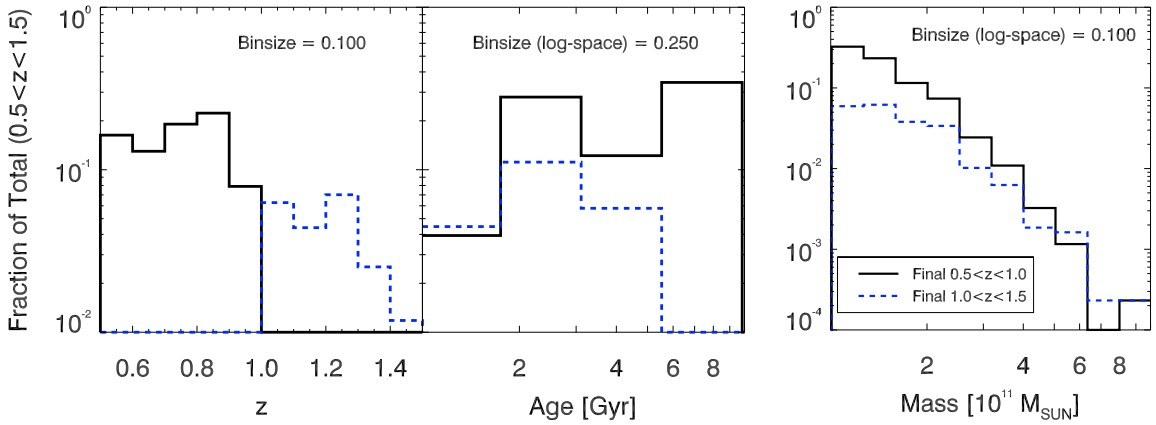

Figure 2.7: Redshift, age, and mass distributions for our final $z = 0.5 - 1.0$ (black solid lines), and $z = 1.0 - 1.5$ (blue dashed lines) galaxies.

Survey Bright Source, Correlation, and Faint Source Catalogs (Voges et al., 1999). To exclude strong dust emitting sources, we remove sources correlated with the Planck Catalogue of Compact Sources (Planck Collaboration et al., 2014), the SPT-SZ Point Source Catalog (Mocanu et al., 2013), the AKARI/FIS All-Sky Survey Bright Source Catalogue (Yamamura et al., 2010), the AKARI/IRC All-Sky Survey Point Source Catalog (Ishihara et al., 2010), the IRAS Point Source Catalog (Helou & Walker, 1988), and all sources classified as Hot DOGs from the WISE All-Sky Data Release Source Catalog (Wright et al., 2010). Hot DOGs are defined as sources detected in WISE bands W3 or W4 but not in either W1 or W2 (e.g., Eisenhardt et al., 2012). Finally, to exclude sources in galaxy clusters, we remove sources correlated with the Planck Catalogue of Sunyaev-Zeldovich Sources (Planck Collaboration et al., 2015e) and the SPT-SZ Cluster Catalog (Bleem et al., 2015).

We also carry out additional co-adds removing sources correlated with three radio surveys in addition to the cuts above, in order to further exclude potential bright AGNs. These are the Australia Telescope 20 GHz Survey Source Catalog (Murphy et al., 2010), the Parkes-MIT-NRAO (PMN) Southern Survey Source Catalog (Wright et al., 1994), and the Sydney University Molonglo Sky Survey (SUMSS) Source Cat-

alog (Mauch et al., 2003). We find that these additional cuts do not significantly change our results, as explained further in Section 2.7.2.

The purpose of using all of these external catalogs is to increase the reliability of our galaxy catalog, which we maximize by aggressively using every external source catalog relevant for potential contamination. This process is imperfect, though, due to the completeness limits of the external catalogs we use as well as the restriction of only using existing publicly available catalogs. We implicitly account for the residual contamination left over from our imperfect contamination removal in Section 2.7.3, where we model what the impact of this undetected contamination is on our measurements.

Applying these cuts results in our final sample of galaxies: 3394 at low-z and 924 at high-z. Their distribution on the sky is shown in Figure 2.5, where we can perhaps start to see signs of large-scale structure. Histograms of the K_s magnitudes for these final two groups are shown in Figure 2.6. Their locations in color-space are plotted in Figure 2.4. Several things are evident in this figure. First, in the gzK_s-plot the stars clearly separate out from the galaxies (red line and Equation (2.17)), showing the quality of our photometry. Secondly, we can see that the blue line (Equation (2.18)) used to pare down the sample and select old and quiescent galaxies is, in fact, a conservative cut with respect to the results of the SED fitting, i.e., there are very few red or blue points near the blue line. The upper two plots show the results before and after correction for Galactic extinction (Schlegel et al., 1998). These plots show that making the color-cuts before applying this correction does not introduce any substantial contamination of our final sample that is selected after the SED fitting stage.

Figure 2.7 shows the redshift, age, and mass distributions of our final galaxy selection. We can see that the number of galaxies as a function of mass is dominated

z	$\langle z \rangle$	$\langle l^2_{\rm ang} \rangle$ (Gpc^2)	$\langle$M$\rangle$ (M$_\odot$)	$\langle$Age$\rangle$ (Gyr)	$\langle$L$_{Ks}\rangle$ (erg s^{-1} Hz^{-1})	$\langle z \rangle_{\rm M}$	$\langle l^2_{\rm ang} \rangle_{\rm M}$ (Gpc^2)
$0.5 - 1.0$	0.72	2.30	1.51×10^{11}	4.34	2.78×10^{30}	0.72	2.30
$1.0 - 1.5$	1.17	3.02	1.78×10^{11}	2.64	4.07×10^{30}	1.19	3.03

Table 2.3: Mean and mass-averaged values for several relevant galaxy parameters in the two final redshift ranges.

by the lowest mass galaxies, although there are fewer of the fainter, lower mass galaxies detected in the higher redshift range. Notice also that the oldest galaxies are found in the lower redshift bin, as expected. To allow for ease of comparison between our results and theoretical models, mean values for redshift, $l^2_{\rm ang}$, mass, age, and K_s-band luminosity, as well as mass-averaged values of redshift and $l^2_{\rm ang}$, are shown for both redshift subsets in Table 2.3. The mean and mass-averaged redshifts and luminosity distances are very close to each other, indicating no strong evolution of the mass distribution within each redshift bin.

2.7 Measuring the tSZ Signal

2.7.1 SPT-SZ Filtering

As discussed in Section 2.2.2, the signal we are looking for occurs on arcminute scales, comparable to the resolution of the SPT-SZ data we are working with. On the other hand, the overall anisotropy of the CMB is dominated by the primary signal, which is strongest on degree scales. For this reason it is essential for us to filter our maps before obtaining our measurements. Since we are making measurements on the smallest scales (approaching the beam size), we apply a filter to the SPT-SZ data in order to optimize point-source measurements. This optimal filter in Fourier-space, ψ,

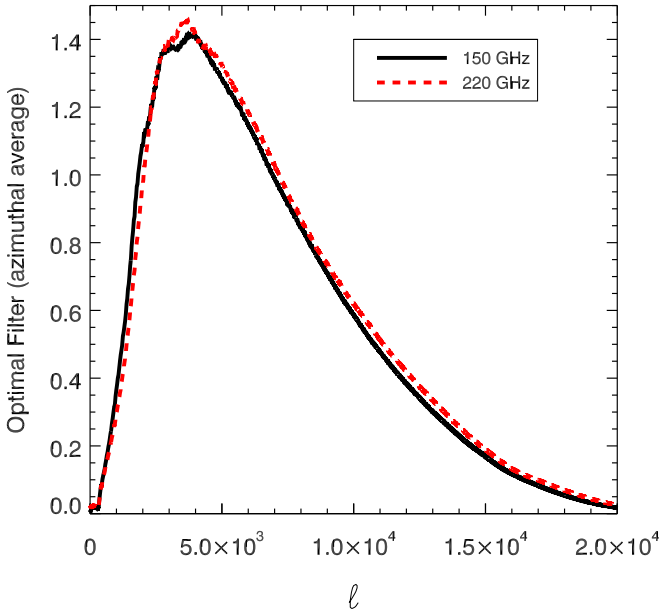

Figure 2.8: Optimal azimuthally-averaged filter curves in ℓ-space for both SPT bands. These are scaled to preserve the flux within a 1 arcmin radius circle in the SPT images.

is (Schaffer et al., 2011)

$$\psi = \frac{\tau}{P}\left[\int d^2k \frac{\tau^2}{P}\right]^{-1}, \tag{2.19}$$

where τ is the Fourier-space source profile and P is the Fourier-space noise power spectrum, which is the sum of the (squared) instrument-plus-atmosphere power spectral density and the primary CMB power spectrum. For a point source $\tau = B \times F$, where B is the Fourier-space beam function and F is the Fourier-space filter transfer function. We then scale ψ in order to preserve the total flux within a 1 arcmin radius circle in each map. Thus we expect our primary signal, which we measure in a 1 arcmin radius aperture around our stacked galaxies, to be minimally affected by our filtering. The resulting optimal point source filters for the 150 and 220 GHz bands are shown in Figure 2.8.

2.7.2 Galaxy Co-adds

We carried out our final co-add measurements by averaging the SPT-SZ maps around the galaxies in both our final low- and high-redshift galaxy samples. Before we are able to measure a signal from these averages, however, we first need to correct for a bias introduced by our removal of all sources within 4 arcmin of contaminating sources. Because the SPT-SZ maps themselves are normalized to a mean of 0, and all of the contaminating sources introduce positive signal into the maps, the average value in the uncontaminated regions of the maps is slightly biased to negative values. We therefore calculate a bias for the "contaminant-free" images by choosing 140,000 random points in our field (chosen so that there are not more random points than possible beams on the sky) and subjecting the points to the same contaminating-source cuts as our galaxies. We then take the resulting 107,561 random points and compute the mean sums within a 1 arcmin radius around each point. With these values we calculate an offset value needed to re-normalize the mean to 0. These offset values are 0.24 ± 0.09 and 0.58 ± 0.13 μK arcmin^2 at 150 and 220 GHz, respectively.

We then sum and average the total signal within 0.5, 1, 1.5, and 2 arcmin radius apertures around our sources and add the offset, scaling them appropriately for the different aperture sizes. The 0.5 arcmin radius aperture represents roughly the size of the 150 and 220 GHz beam FWHMs, which are 1.15 arcmin and 1.05 arcmin, respectively. Additionally, we calculate the standard deviation for each of these measurements by finding the standard deviation of the same size co-added region around an equal number of random points in our field, subjected to the same contaminating source cuts. The offset uncertainties are also included but are negligible. The final co-add values for each aperture size and redshift range are given in Table 2.4. The final galaxy co-add images for both redshift ranges are shown in Figure 2.9.

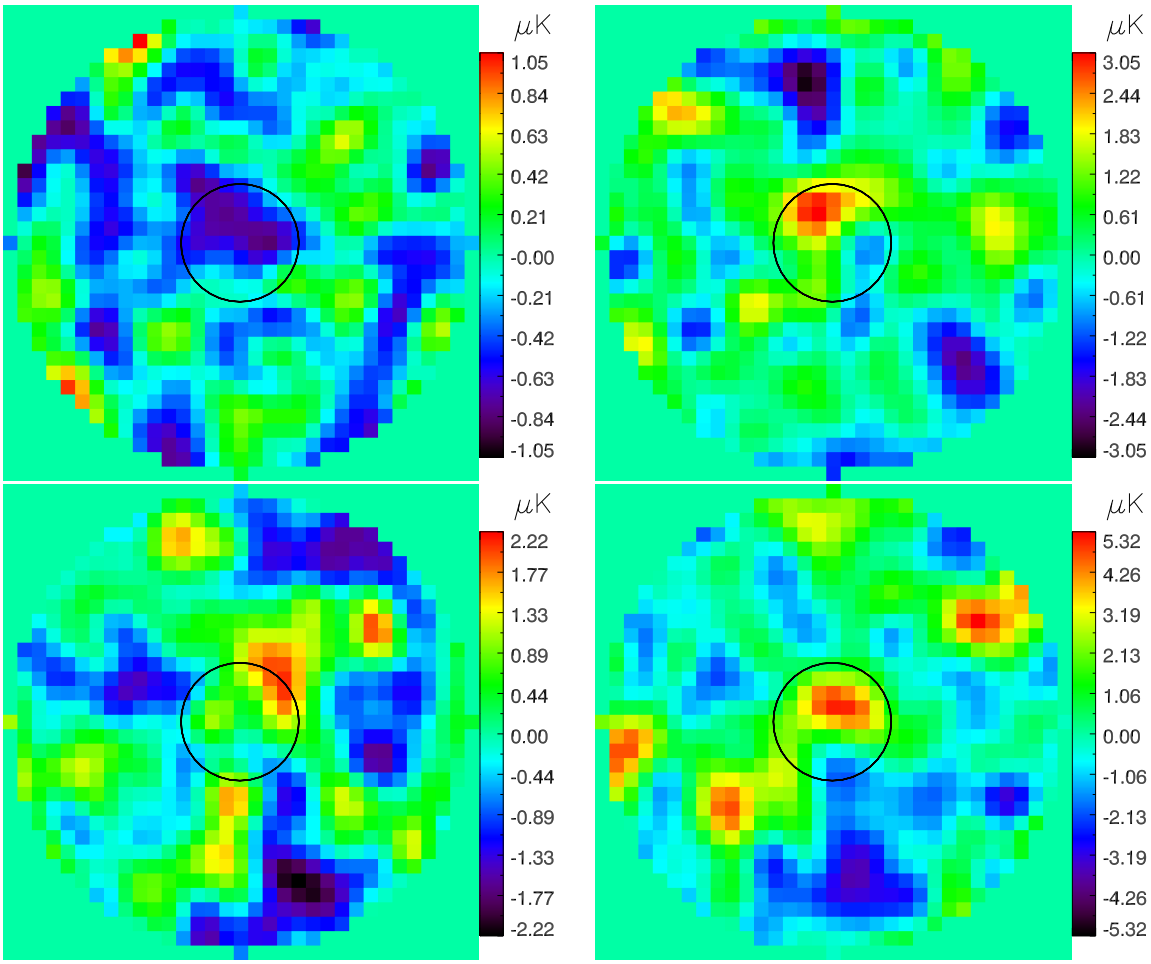

Figure 2.9: Final co-added galaxy images. Left: 150 GHz. Right: 220 GHz. Top: $0.5 \leq z \leq 1.0$. Bottom: $1.0 \leq z \leq 1.5$. The images are 8×8 arcmin (33×33 pixels). They represent the region where we have rejected any contaminating sources (see Section 2.6). The black circles represent a 1 arcmin radius aperture.

The upper left panel of this figure shows a clear $\approx$1 arcmin size $\approx 2\sigma$ negative feature centered directly on our stack of low-z galaxies, with a magnitude consistent with a significant tSZ signal. Moreover, the low-z 220 GHz measurements show a strong positive signal centered on our co-added sources. Because the tSZ effect has a negligible impact at this frequency, this indicates that despite our cuts on detected contaminating sources, there still remains a significant positive contaminating signal at 220 GHz, made up of the sum of fainter sources. Looking at the emission by

the typical range of dust temperatures at $z = 1$ (light blue and dark blue curves in Figure 2.10), the CMB spectrum (green curve in Figure 2.10), and the frequencies of our SPT measurements (rightmost red hatched regions in Figure 2.10), it appears likely that this contaminating signal at 220 GHz extends into the 150 GHz band, meaning that the true tSZ signal for the lower-redshift galaxies we have selected is even more negative than the values in Table 2.4.

Moving to the higher redshift stacks shown in the bottom panel of Figure 2.9, we find that the stacked emission of our galaxies in the 150 GHz map is consistent with zero signal. However, as this band measures the sum of the (negative) tSZ and the (positive) contaminating sources, it is difficult to interpret these results without also considering the high-z measurements at 220 GHz. As in the lower redshift case, this band shows a clear excess, but now at a magnitude that is roughly twice that seen in the low-z stack. This suggests that, because it is more difficult to identify contaminating sources at higher redshift, the high-z 150 GHz measurement is more contaminated than the lower-redshift measurement, covering up the negative signal in which we are interested. In both redshift ranges, however, it is clear that obtaining the best possible constraints on AGN feedback requires making the best possible separation between the tSZ signal and the contaminating signal, a topic we address in detail below. Finally, we can convert our co-added ΔT signal into gas thermal energy using Equation (2.16). These values (using a 1 arcmin radius aperture) are shown in Table 2.6, under "Data only".

As mentioned in Section 2.6, we performed the same co-adding method while also removing galaxies near bright radio sources. After these additional cuts, the number of final galaxies becomes 2,219 for our low-z subset and 614 for our high-z subset. The resulting co-add values for a 1 arcmin radius aperture are: -1.7 ± 0.9 μK arcmin^2 for 150 GHz low-z, 2.4 ± 1.7 μK arcmin^2 for 220 GHz low-z, 0.9 ± 1.7 μK arcmin^2

z	Band (GHz)	0.5 arcmin (μK arcmin^2)	1 arcmin (μK arcmin^2)	1.5 arcmin (μK arcmin^2)	2 arcmin (μK arcmin^2)
0.5 - 1.0	150	-0.53 $\pm$ 0.26	-1.5 $\pm$ 0.7	-2.3 $\pm$ 1.3	-2.7 $\pm$ 1.9
0.5 - 1.0	220	0.85 $\pm$ 0.53	3.0 $\pm$ 1.4	5.4 $\pm$ 2.3	6.4 $\pm$ 3.0
1.0 - 1.5	150	0.39 $\pm$ 0.49	1.6 $\pm$ 1.4	2.8 $\pm$ 2.5	3.2 $\pm$ 3.7
1.0 - 1.5	220	2.6 $\pm$ 1.0	6.3 $\pm$ 2.7	7.9 $\pm$ 4.4	7.4 $\pm$ 5.7

Table 2.4: Final co-added signals. The columns show four different aperture sizes by radius. The smallest aperture represents roughly the beam FWHM.

for 150 GHz high-z, and 10.4 ± 3.3 μK arcmin^2 for 220 GHz high-z. We find that the additional radio source cuts do not significantly change our results except for an increased positive signal at 220 GHz in the high-z subset, though they do increase the noise in our measurements because we are co-adding a smaller number of galaxies. As a result, we do not use the radio source cuts in our modeling and analysis below, though the higher 220 GHz signal in the high-z subset may suggest a more significant tSZ detection in our high-z results.

2.7.3 Removing Residual Contamination

In order to constrain the impact that undetected contaminating sources have on our tSZ measurements, we build a detailed model of contaminants based on an extrapolation of the SPT source counts measured in Mocanu et al. (2013). Our approach is to extend these counts to fainter values by modeling a random population of undetected sources that follow the trend of the detected sources into the unresolved region, which we then relate to the contaminating signal in both our 150 and 220 GHz measurements.

To be clear about this process, the initial motivation is the observed contamination signal in the 150 and 220 GHz measurements. Since we have cut out galaxies

near all possible known contaminating sources that we could find, we associate the contamination signal with undetected contaminants. We therefore want to find out what types of undetected contaminants produce signals across the 150 and 220 GHz bands that best fit our measurements. Since we do not know how the undetected contaminants behave across the 150 and 220 GHz bands, we cannot just do a simple subtraction of the 220 GHz pure contamination signal from the 150 GHz contamination + tSZ signal. This leads to the main strategy used here: we vary the number of undetected contaminants, whether the contaminants have a dust spectrum or a synchrotron spectrum, the fraction of our measured galaxies that are affected by contamination, and the underlying 150 GHz tSZ signal. We do this using a range of values for each of these parameters that reflects the most likely value and its corresponding uncertainty. For every combination of these parameter ranges, we find out how well the observed signals are duplicated, and ultimately we hope to find out what combination of parameters best reflects the observed signals.

Following Mocanu et al. (2013) we separate contaminants into synchrotron sources, which emit most at lower frequencies, and dusty sources, which emit most at higher frequencies. For each source population we model the number counts as a power law,

$$\frac{dN}{dS} = \frac{N_0}{S_{\rm max}} \left(\frac{S}{S_{\rm max}} \right)^{\alpha}, \tag{2.20}$$

where dN/dS is the number of sources between flux S and $S + dS$, N_0 is an overall amplitude, α is the power-law slope, and $S_{\rm max}$ is the flux at which all brighter sources have a 100% completeness level in the source count catalog. We then compute a range of allowed source count slopes from the Mocanu et al. (2013) data, by carrying out a χ^2 fit in log-space. Our best-fit slopes at 150 GHz were $\alpha_s = -2.05 \pm 0.04$ for the synchrotron sources and $\alpha_d = -2.70 \pm 0.19$ for the dusty sources.

Note that our calculated values for α_d are much steeper than α_s, meaning that while the number density of detected sources is dominated by synchrotron sources, the number density of undetected sources is likely to be dominated by dusty emitters. Note also that α_d and α_s are sufficiently steep that the number of sources diverges as S goes to 0, meaning that the source count distribution must fall off below some as-yet undetected flux. For simplicity, we model this fall-off as a minimum flux $S_{\rm min}$ below which there are no contaminating sources associated with the galaxies we are stacking.

For any choice of α_d, α_s, and $S_{\rm min}$ (which we will call a "source-count model"), we are then able to construct a model population of contaminating source fluxes through a four-step procedure as follows: (i) for each model source, we randomly decide whether it is a synchrotron source or a dusty source, such that the overall fraction of detectable dusty sources to synchrotron sources matches the observed source counts; (ii) we then assign the source a random 150 GHz flux, $S_{150,\rm rand}$, by inverting

$$\int_{S_{150,\rm min}}^{S_{150,\rm rand}} dS\,\frac{dN}{dS} = R\int_{S_{150,\rm min}}^{S_{150,\rm max}} dS\,\frac{dN}{dS}, \tag{2.21}$$

where $R \in [0,1]$ is a random number, such that their overall population matches the source count slopes. This gives

$$S_{150,\rm rand} = \left[(1-R)\,S_{150,\rm min}^{\alpha+1} + R\,S_{150,\rm max}^{\alpha+1}\right]^{\frac{1}{\alpha+1}}; \tag{2.22}$$

(iii) to obtain a corresponding flux for the source at 220 GHz we use the α_{220}^{150} spectral index distributions from Mocanu et al. (2013), which we assume to have normalized Gaussian shapes with the properties (center, σ) = (-0.55, 0.55) for synchrotron sources and (3.2, 0.89) for dusty sources. We then randomly choose α_{220}^{150} values that fit these distributions and calculate the 220 GHz flux (following Mocanu et al., 2013) as

$$S_{220,\rm rand} = S_{150,\rm rand} \times 0.82 \times 1.43^{\alpha_{220}^{150}}, \tag{2.23}$$

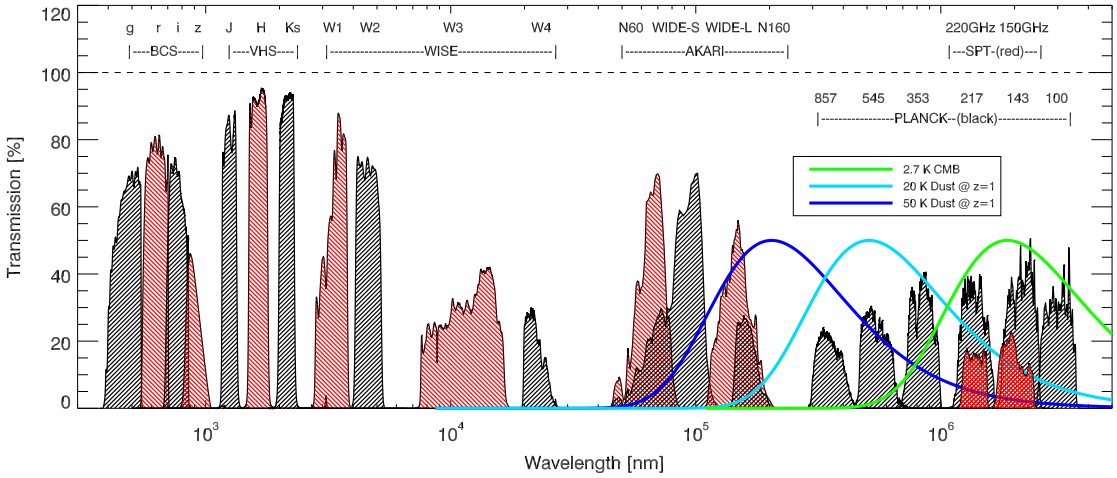

Figure 2.10: The filter curves for several of the data sets used in this paper are shown. From left to right: BCS and VHS bands used for galaxy selection, Wide-Field Infrared Survey Explorer (WISE), AKARI, and Planck bands used for identifying and constraining the signal from dusty contaminating sources, and SPT-SZ bands used for measuring the tSZ effect. The first four surveys alternate between black and red for each band, while Planck bands are all black and SPT-SZ bands are all red to distinguish between the two. Also shown are blackbody curves for the CMB (green), 20 K dust at $z = 1$ (light blue), and 50 K dust at $z = 1$ (dark blue), all normalized to 50% on the plot. The horizontal dashed line indicates 100% transmission.

where we use units of μK arcmin^2 for all S; and (iv) finally, if the source had a detectable 150 or 220 GHz flux, we randomly discard it with a probability chosen to match the completeness percentages in the source count catalog.

For any single source-count model, we repeat the process 100,000 times, resulting in a large catalog of contaminating fluxes in both bands. From these, we compute the mean flux per contaminating source in each band, $\langle S_{150,\mathrm{cont}} \rangle$ and $\langle S_{220,\mathrm{cont}} \rangle$, which represents the contamination we are measuring in our stacks. To account for variations in the input parameters, we compute model contamination signals for a wide range of source-count models, with $S_{150,\mathrm{max}} = 260\,\mu$K arcmin^2. We vary both α_d and α_s from -2σ to $+2\sigma$ in steps of σ, and we let $\log_{10}(S_{\mathrm{min}})$ vary from $\log_{10}(0.01\ \mu$K arcmin^2) to $\log_{10}(30\ \mu$K arcmin^2) in steps of 0.2 in log-space.

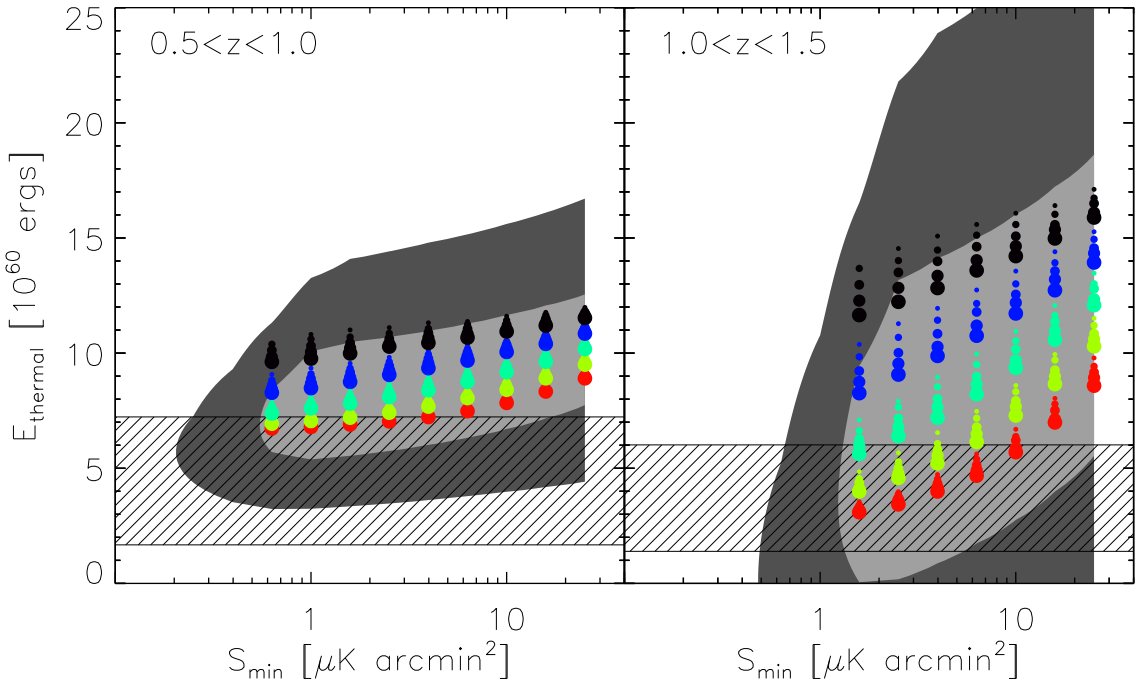

Figure 2.11: Plot of the contaminant-corrected $E_{\rm therm}$ (see Equation (2.16)) for different choices of $\alpha_{\rm dust}$, $\alpha_{\rm sync}$, and $S_{\rm min}$. Points are located at the peak χ^2 probability for each model. Increasing size represents increasing (i.e. more positive) α_s, and changing color from red to black represents increasing α_d. The light and dark gray regions represent the complete span of $\pm1\sigma$ and $\pm2\sigma$, respectively, for all points. The hatched regions represent the $\pm1\sigma$ range for $E_{\rm grav}$ (see Equation (2.12)).

For each source-count model, we compute best-fit tSZ values by varying our two free parameters, tSZ signal ($S_{\rm SZ}$) and the fraction of our measured sources that are contaminated ($f_{\rm cont}$). We vary the tSZ signal from -50 to 50 μK arcmin^2 in steps of 0.1 μK arcmin^2, and we vary the fraction contaminated from -3 to 9 in steps of 0.01. For every combination of these parameters we compute

$$\chi^2(f_{\rm cont}, S_{\rm SZ}) = \mathcal{B} \times \mathcal{A}^{-1} \times \mathcal{B}^T, \tag{2.24}$$

where $\mathcal{B}$ is the signal array,

$$\mathcal{B} = \begin{pmatrix} f_{\rm cont} \times \langle S_{150,{\rm cont}} \rangle + S_{\rm SZ} - S_{150} \\ f_{\rm cont} \times \langle S_{220,{\rm cont}} \rangle - S_{220} \end{pmatrix}, \tag{2.25}$$

and $\mathcal{A}$ is the noise matrix containing the noise for each band plus the covariance terms between each band,

$$\mathcal{A} = \begin{pmatrix} \sigma_{150}^2 & \sigma_{150}\sigma_{220} \\ \sigma_{150}\sigma_{220} & \sigma_{220}^2 \end{pmatrix}. \tag{2.26}$$

Here, S_{150}, S_{220}, σ_{150}, and σ_{220} are our measured 1 arcmin radius values from Table 2.4. As discussed in Section 2.7.2, the σ values are computed using random point measurements. To be explicit here,

$$\sigma_i \sigma_j = \frac{\sum_{a=0}^{N_{\rm rand}} (S^a_{i,\rm rand} - \langle S_{i,\rm rand} \rangle) \times (S^a_{j,\rm rand} - \langle S_{j,\rm rand} \rangle)}{N_{\rm rand} N_{\rm source}}, \tag{2.27}$$

where i and j represent the bands, $S_{a,\rm rand}$ and $S_{b,\rm rand}$ represent the 1 arcmin radius aperture values for the random points, $N_{\rm rand} = 107,561$ is the number of random points used, and $N_{\rm source}$ is the number of galaxies used (3394 for low-z and 924 for high-z). We then convert the χ^2 values to Gaussian probabilities P by taking

$$P(S_{\rm SZ}) = \frac{\sum_{f_{\rm cont} \in [0,1]} \exp[-\chi^2(f_{\rm cont}, S_{\rm SZ})/2]}{\sum_{f_{\rm cont}} \sum_{S_{\rm SZ}} \exp[-\chi^2(f_{\rm cont}, S_{\rm SZ})/2]}, \tag{2.28}$$

where the lower sum over $f_{\rm cont}$ runs from -3 to 9 and the lower sum over $S_{\rm SZ}$ runs from -50 to 50 μK arcmin^2. Our approach is thus to marginalize over values of $f_{\rm cont}$ in the full physical range from 0 to 1, but normalize the overall probability by the sum of $f_{\rm cont}$ over a much larger range, including unphysical values. This excludes models in which a good fit to the data can only be achieved by moving $f_{\rm cont}$ outside the range of physically possible values.

Equation (2.28) then gives us a function $P(S_{\rm SZ})$ for each combination of α_d, α_s, and $S_{\rm min}$. We can convert the corresponding $S_{\rm SZ}$ value to the gas thermal energy, $E_{\rm therm}$, using Equation (2.16) and the average $l^2_{\rm ang}$ from Table 2.3. Note that a positive detection of the tSZ effect is seen as a negative ΔT signal at 150 GHz, and it represents a positive injection of thermal energy into the gas around the galaxy. Additionally,

we compute a corresponding range for $E_{\rm grav}$ using Equation (2.12) and values from Table 2.3. The peak of each $P(S_{\rm SZ})$ curve is shown as the colored points in Figure 2.11, where α_s (represented by point size) is increasing (i.e. becoming more positive) downwards, and α_d (represented by point color) is increasing upwards. The 1σ and 2σ contours are computed for each $S_{\rm min}$ by averaging $P(S_{\rm SZ})$ across α_d and α_s. The resulting probability distribution depends only on $E_{\rm therm}$ and $S_{\rm min}$, and 1σ and 2σ are represented by the values $P(S_{\rm SZ}) = 0.61$ and 0.13, respectively (i.e. $\exp[-\sigma^2/2]$). These contours are shown in Figure 2.11, along with the $\pm 1\sigma$ range for $E_{\rm grav}$. From this figure we see that there is a $> 2\sigma$ tSZ detection for every source model at low-z, and a $\approx 1\sigma$ detection of a signal exceeding the range that can be explained without feedback. At high-z, where the contaminants are harder to constrain, there is a $\approx 1\sigma$ tSZ detection for every source model.

Finally, we average the probability distribution across $S_{\rm min}$ to get a final distribution as a function of only $E_{\rm therm}$. The significance values of this curve are shown in the "SPT only" part of Table 2.6. We see a $> 3\sigma$ total tSZ detection at low-z, and a nearly 1σ tSZ detection at high-z. Furthermore, in both redshift bins, the best fit values are higher than expected from models that do not include AGN energy input.

2.7.4 Removing Residual Contamination Using Planck Data

In order to better constrain the impact of dusty contaminating sources on our measurements, we made use of the 2015 public data release from the Planck mission, focusing on the high-frequency bands at 857, 545, 353, and 217 GHz (see the rightmost black hatched regions in Figure 2.10). While the FWHM beam size for this data is about 5 arcmin (Planck Collaboration et al., 2015a), and thus too low-resolution to detect the tSZ signal in which we are interested, the data provides information at the higher frequencies at which the dusty sources should be much brighter (i.e. the light

blue and dark blue curves in Figure 2.10). Therefore these measurements have the potential to discriminate between contaminant models, allowing us to better remove this contribution from the tSZ signal.

Our goal is to use this data to add terms to our χ^2 fit that quantify, for each source model, how consistent a given choice of $f_{\rm cont}$ is with the Planck measurements. In addition to the parameters used in the previous section, we also now vary our models over reasonable values for contaminating dust temperature and residual CMB primary signal. Since there are now several more terms to fit, we can weight our final probabilities by the best fitting χ^2 values for each model. To compute these extra χ^2 terms, we again construct stacks of the data over each of our galaxies, but now, because of the lower resolution of the Planck data, we extend our contaminant source cuts to within 10 arcmin of known potentially contaminating sources. This results in a decreased number of final galaxies, now 937 at low-z and 240 at high-z. In order to filter out the primary CMB signal, we convolve each map with a 7 arcmin FWHM Gaussian and subtract the resulting map from the original. We then stack the central pixels of every source to get co-added values for our galaxies in each of the Planck bands. In addition, we degrade the SPT 150 and 220 GHz maps to match the beam size of Planck, apply the same 7 arcmin FWHM filtering, and stack the galaxies on those images as well.

As was the case in Section 2.7.2, in all of these stacks there is an offset we need to correct for since we are purposely avoiding positive contaminations in the maps. To do this we also make measurements at 3,000 random points on the sky that were restricted to the same contaminating-source cuts as our galaxies. These measurements allow us to compute offset values needed to re-normalize each band to a mean of 0, which we applied to our final measurements.

Finally, we compute our measurement errors by using the random point measurements (since the proper noise covariance matrix is not provided, i.e. Planck Collaboration et al., 2015b), corrected in two ways. First, because we account for the residual CMB primary signal in the χ^2 calculations as discussed below, we remove the error due to the CMB primary itself. To estimate this contribution, we take 95% of the minimum covariance between the SPT 150 and 220 GHz bands (filtered to match the Planck bands) and the Planck 217 GHz band, since these are mostly dominated by the CMB primary signal which will therefore be correlated between them. The minimum covariance is between the two SPT bands, and it is 7.85 μK. Second, there is an error introduced due to our offset corrections because they are made from a large, but finite number of points. We then get the corrected error from

$$(\sigma_i\sigma_j)_{\rm corr} = \sqrt{\frac{\sigma_i\sigma_j - \sigma_{\rm cov}^2}{\rm N_{source}} + \frac{\sigma_i\sigma_j}{\rm N_{random}}}, \tag{2.29}$$

where $\sigma_i\sigma_j$ is given by Equation (2.27) with i and j representing the various bands used, $\sigma_{\rm cov} = 7.85\,\mu$K is the minimum CMB covariance discussed above, $\rm N_{source}$ is the number of sources used for the measurements (937 for low-z and 240 for high-z), and $\rm N_{random} = 3000$ is the number of random points used.

Note that this represents both the error due to detector noise in each band, as well as the error due to contributions from foregrounds on the sky. In fact, the majority of the variance at the highest frequencies is correlated between the bands and likely due to contributions from Galactic dust emission. However, unlike the primary CMB signal, the spectral shape of this foreground is similar to that of the dusty sources we are trying to constrain, and it cannot be removed by fitting it separately.

In the same manner as the previous section, we model SPT-SZ 150 and 220 GHz contaminant source fluxes using a range of different source-count models (i.e. α_d, α_s, and $S_{\rm min}$), resulting again in 100,000 modeled contaminating source fluxes in

each SPT band, $S_{150,\mathrm{cont}}$ and $S_{220,\mathrm{cont}}$. We also model what the contaminating signal would be in the Planck bands and the SPT bands filtered to match Planck. For each modeled contaminating source, if it is chosen to be a synchrotron source we simply extrapolate the Planck-based fluxes as

$$S_{\nu,\mathrm{sync}} = S_{150,\mathrm{cont}} \times \left(\frac{\nu}{150}\right)^{\alpha_{220}^{150}} \times C_\nu \times F, \tag{2.30}$$

where α_{220}^{150} is the same used in the previous section, C_ν is a frequency-dependent factor involved in the conversion from Jy/sr to μK, and $F = 0.021$ is the factor required to preserve the signal within a 1 arcmin radius aperture after applying the Planck filtering we used.

In order to accurately describe thermal dust emission across the Planck frequencies, we adopt a modified blackbody with a free emissivity index, β, and dust temperature, T_{dust}, often referred to as a graybody (Planck Collaboration et al., 2015c). This requires us to add another free parameter, the temperature of the contaminant dust, T_{dust}. This slope of each dusty source as a function of frequency is then

$$\left.\frac{\mathrm{d}\ln S_\nu}{\mathrm{d}\ln \nu}\right|_{\nu=185\mathrm{GHz}} = 3 + \beta - x_{185}[1-\exp(-x_{185})]^{-1}, \tag{2.31}$$

where $x_{185} \equiv (185\ \mathrm{GHz}) \times h/(kT) = (185/416)(1+z)/T_{20}$ and T_{20} is T_{dust} in units of 20 K, and we use the slope of the blackbody function at $\nu = 185$ GHz because it is halfway between our two SPT bands (150 and 220 GHz). This can be related, in turn, to the power law index α_{220}^{150}, from Section 2.7.3, as

$$\beta + 3 = \alpha_{220}^{150} + x_{185}[1-\exp(-x_{185})]^{-1}. \tag{2.32}$$

This then gives

$$\begin{aligned} S_{\nu,\mathrm{dust}} = S_{150,\mathrm{cont}} &\times \left(\frac{\nu}{150}\right)^{\alpha_{220}^{150} + x_{185}[1-\exp(-x_{185})]^{-1}} \\ &\times \frac{\exp[(150/416)(1+z)/T_{20}] - 1}{\exp[(\nu/416)(1+z)/T_{20}] - 1} \times C_\nu \times F, \end{aligned} \tag{2.33}$$

where we vary $T_{\rm dust}$ from 20 K to 50 K in steps of 3 K (equivalently, T_{20} from 1 to 2.5 in steps of 0.15).

With these expressions, we are able to compute χ^2 values for each source-count model accounting for the Planck measurements. This time, in addition to varying $f_{\rm cont}$ and $S_{\rm SZ}$, we also vary $\rm T_{dust}$ (as discussed above) and a parameter Δ, which represents the offset due to the CMB primary signal, which we vary from -3 μK to 3 μK in steps of 0.1 μK. Computing χ^2 now involves the original SPT terms plus the new Planck terms, and it follows the same process as in the previous section (e.g. Equation (2.24)),

$$\chi^2(f_{\rm cont}, S_{\rm SZ}, T_{\rm dust}, \Delta) = \mathcal{B} \times \mathcal{A}^{-1} \times \mathcal{B}^T, \tag{2.34}$$

where $\mathcal{B}$ is the signal array and $\mathcal{A}$ is the noise matrix containing the noise for each band plus the covariance terms between each band. We will denote each element of the signal array $\mathcal{B}_i$, where i runs over the two SPT bands (i.e. 150 and 220 GHz) and then every Planck-filtered band (i.e. the Planck bands at 857, 545, 353, and 217 GHz, plus the SPT bands at 220 and 150 GHz filtered to match the Planck images). We then have $\mathcal{B}_1 = f_{\rm cont} \times \langle S_{150,\rm cont} \rangle + S_{\rm SZ} - S_{150}$, $\mathcal{B}_2 = f_{\rm cont} \times \langle S_{220,\rm cont} \rangle - S_{220}$, and $\mathcal{B}_{3-8} = f_{\rm cont} \times \langle S_{3-8,\rm cont} \rangle + \Delta - S_{3-8}$. As before, S_i represents the final values of our galaxy stacks for each band. We similarly define the elements of the noise matrix as $\mathcal{A}_{ij} = \sigma_i \sigma_j$, where i and j run over all of the bands and $\sigma_i \sigma_j$ is given by Equation (2.29).

As in the previous section, we then convert the χ^2 values to Gaussian probabilities by taking

$$P(S_{\rm SZ}) = \sum_{f_{\rm cont} \in [0,1], T_{\rm dust}, \Delta} \frac{\exp[-\chi^2(f_{\rm cont}, S_{\rm SZ}, T_{\rm dust}, \Delta)/2]}{\sum_{\rm all} \exp[-\chi^2/2]}, \tag{2.35}$$

where the whole function is normalized to a total of 1, and each final SZ value contains the sum over the corresponding $T_{\rm dust}$, Δ, and fractions from 0 to 1. Since in this case

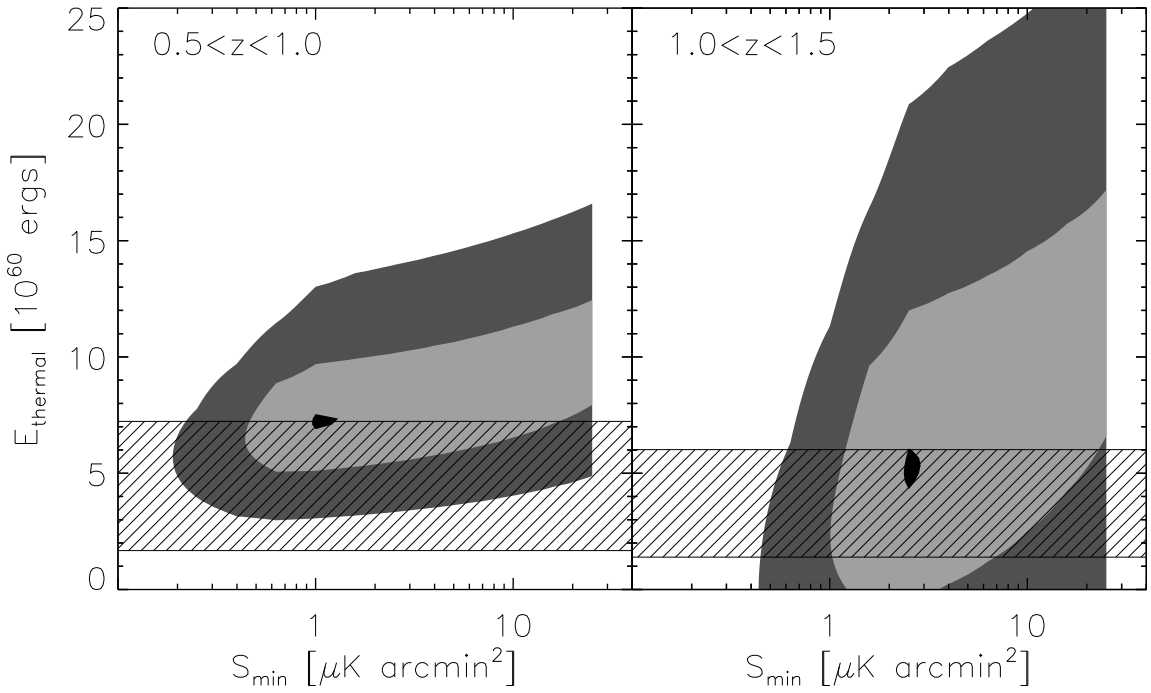

Figure 2.12: Plot of the contaminant-corrected $E_{\rm therm}$ (see Equation (2.16)) for different choices of $\alpha_{\rm dust}$, $\alpha_{\rm sync}$, and $S_{\rm min}$, incorporating the Planck bands. The light and dark gray regions represent the complete span of $\pm 1\sigma$ and $\pm 2\sigma$, respectively, for all points, and the black regions represent the peak of the χ^2 probability distributions, i.e. the most favorable models. The hatched regions represent the $\pm 1\sigma$ range for $E_{\rm grav}$ (see Equation (2.12)).

there are 8 terms contributing to χ^2 and 4 fit parameters, this leaves us with 4 degrees of freedom. Thus the minimum χ^2 will not be 0 in every case as they were previously with just 2 parameters and 2 fit parameters, and so for each model we scale the final probabilities by $\exp(-\chi^2_{\rm min}/2)$, where $\chi^2_{\rm min}$ is the minimum χ^2 value for that model. We find that the the best fit χ^2 values are smaller than expected for 4 degrees of freedom (with some minimum values < 2) due to the correlations between the errors of the various frequency bands due primarily to foreground contamination by Galactic dust. We still expect the results to provide relative confidence levels indicating which models fit the data the best.

This again gives us a function $P(S_{\rm SZ})$ for each combination of α_d, α_s, and $S_{\rm min}$, which we can convert to an energy $E_{\rm therm}$. The 1σ and 2σ contours are created for

Study	N	Type	z	Mass ($M_\odot$)	tSZ Measurement	Type
Chatterjee et al. (2010)	500,000	SDSS quasars	$0.08 - 2.82$	–	$(7.0\pm3.4)\times10^{-7}$	y
Chatterjee et al. (2010)	1,000,000	SDSS LRGs	$0.4 - 0.6$	–	$(5.3\pm2.5)\times10^{-7}$	y
Hand et al. (2011)	1732	SDSS radio-quiet LRGs	0.30 (mean)	8.0×10^{13}	$(7.9\pm6.2)\times10^{-7}$ Mpc^2	$Y_{200\bar{\rho}}$
Gralla et al. (2014)	667	SDSS radio-loud AGN	0.3 (median)	2×10^{13}	$(1.5\pm0.5)\times10^{-7}$ Mpc^2	Y_{200}
Gralla et al. (2014)	4,352	FIRST AGN	1.06 (median)	–	$(5.7\pm1.3)\times10^{-8}$ Mpc^2	Y_{200}
Greco et al. (2015)	188,042	SDSS LBGs	$0.05 - 0.3$	$1.4\times10^{11}\star$	$(0.6^{+5.4}_{-0.6})\times10^{-6}$ arcmin^2	$\tilde{Y}_c^{cyl}$
Ruan et al. (2015)	≈14,000	SDSS quasars	1.96 (median)	5.0×10^{12}	$(4.8\pm0.8)\times10^{-6}$ Mpc^2	Y
Ruan et al. (2015)	≈14,000	SDSS quasars	0.96 (median)	5.0×10^{12}	$(2.2\pm0.9)\times10^{-6}$ Mpc^2	Y
Ruan et al. (2015)	81,766	SDSS LBGs	0.54 (median)	$3.2\times10^{11}\star$	$(1.4\pm0.4)\times10^{-6}$ Mpc^2	Y
Crichton et al. (2016)	17,468	SDSS radio-quiet quasars	$0.5 - 3.5$	–	$(6.2\pm1.7)\times10^{60}$ erg	E_{th}

Table 2.5: Previous tSZ measurements. LRGs = luminous red galaxies; LBGs = locally brightest galaxies. Masses refer to halo masses, except for those of Greco et al. (2015) and Ruan et al. (2015) LBGs which refer to stellar masses ($\star$). We select Hand et al. (2011) and Greco et al. (2015) values that have the most similar masses to our galaxies.

each $S_{\rm min}$ by averaging $P(S_{\rm SZ})$ across α_d and α_s and then dividing the final result by the single maximum value. 1σ and 2σ are again represented by the values 0.61 and 0.13, respectively, with peak probability values represented by $P(S_{\rm SZ}) > 0.99$. These contours are shown in Figure 2.12, along with the $\pm1\sigma$ range for $E_{\rm grav}$. From this figure we can see that the σ values have slightly decreased at both low-z and high-z, especially at higher $S_{\rm min}$ values for high-z. This is where the contaminants are hardest to constrain with just SPT, and where Planck data helps us the most.

Finally, we average the probability distribution across $S_{\rm min}$, divided by the maximum value again, and get a final distribution as a function of only $E_{\rm therm}$. The significance (σ) values of this curve are shown in the "With Planck" part of Table 2.6. Planck has helped to constrain the tSZ signal, especially at high-z, although it is clear that the gain in sensitivity has been limited by the decrease in the number of galaxies in each redshift bin due to the much larger beam size of Planck compared to SPT.

Model	N	z	$\int \Delta T_{150}(\boldsymbol{\theta}) d\boldsymbol{\theta}$ (μK arcmin^2)	Y (10^{-7} Mpc^2)	$E_{\rm therm}(\pm 1\sigma)$ (10^{60} erg)	$E_{\rm therm}(\pm 2\sigma)$ (10^{60} erg)	S/N (S/σ)
Data only	3394	$0.5-1.0$	-1.5 ± 0.7	1.2 ± 0.6	4.1 ± 1.9	4.1 ± 3.8	2.2
	924	$1.0-1.5$	1.6 ± 1.4	-1.7 ± 1.5	-5.8 ± 5.1	-5.8 ± 10.2	-1.1
χ^2 (SPT only)	3394	$0.5-1.0$	$-2.9^{+0.9}_{-1.1}$	$2.3^{+0.9}_{-0.7}$	$8.1^{+3.0}_{-2.5}$	$8.1^{+6.8}_{-4.8}$	3.5
	924	$1.0-1.5$	$-1.8^{+1.9}_{-2.3}$	$1.9^{+2.4}_{-2.0}$	$6.7^{+8.3}_{-7.0}$	$6.7^{+18.6}_{-13.3}$	0.9
χ^2 (With Planck)	937	$0.5-1.0$	$-2.8^{+0.8}_{-1.1}$	$2.2^{+0.9}_{-0.7}$	$7.6^{+3.0}_{-2.3}$	$7.6^{+7.1}_{-4.3}$	3.6
	240	$1.0-1.5$	$-1.7^{+1.7}_{-2.1}$	$1.7^{+2.2}_{-1.8}$	$6.0^{+7.7}_{-6.3}$	$6.0^{+18.0}_{-12.3}$	0.9

Table 2.6: Our final tSZ measurements using various methods for removing contamination. The last three columns represent the best fit $E_{\rm therm}$ values with $\pm 1\sigma$ values and $\pm 2\sigma$ values and the $E_{\rm therm}$ signal-to-noise ratio (S/σ), respectively.

Alternatively, we can also characterize the total tSZ signal for our coadds with the angularly integrated Compton-y parameter, Y (e.g., Ruan et al., 2015). While we cannot directly compare peak Compton-y values with past measurements, as these are beam-dependent quantities, we can compare the angularly integrated Y values between our results and past experiments (see Table 2.5). Using Equation (2.15) at 150 GHz, this is

$$Y \equiv l_{\rm ang}^2 \int y(\boldsymbol{\theta}) d\boldsymbol{\theta} = -3.5 \times 10^{-8}\,{\rm Mpc}^2 \left(\frac{l_{\rm ang}}{\rm Gpc}\right)^2 \frac{\int \Delta T_{150}(\boldsymbol{\theta}) d\boldsymbol{\theta}}{\mu{\rm K\ arcmin}^2}, \tag{2.36}$$

such that $Y = 2.9 \times 10^{-8}\,{\rm Mpc}^2 E_{60}$, where E_{60} is $E_{\rm therm}$ in units of 10^{60} erg. In these units, the mean Y values computed directly from the 150 GHz maps from our co-added galaxies are $1.2(\pm 0.6) \times 10^{-7}$ Mpc^2 for low-z and $-1.7(\pm 1.5) \times 10^{-7}$ Mpc^2 for high-z. When these measurements are corrected for contamination using the 220 GHz SPT data, the mean Y values become $2.3^{+0.9}_{-0.7} \times 10^{-7}$ Mpc^2 for low-z and $1.9^{+2.4}_{-2.0} \times 10^{-7}$ Mpc^2 for high-z, and once the Planck data is incorporated, the mean Y values become $2.2^{+0.9}_{-0.7} \times 10^{-7}$ Mpc^2 for low-z and $1.7^{+2.2}_{-1.8} \times 10^{-7}$ Mpc^2 for high-z. These values are also given in Table 2.6.

Our $0.5 \leq z \leq 1.0$ value of $2.2^{+0.9}_{-0.7} \times 10^{-7}$ Mpc^2 is more than 3 times smaller than the Hand et al. (2011) $z \approx 0.3$ SDSS radio-quiet LRG result. If we estimate the stellar mass for the Hand et al. (2011) results using Table 2.5 and Equation (2.11) we get $1.7 \times 10^{12} M_{\odot}$, which is about an order of magnitude greater than the average stellar mass of our galaxies. Our smaller values could be indicative of the relation that tSZ signal increases with halo (and stellar) mass (i.e., Gralla et al., 2014). Our low-z result is within about 1σ of the Gralla et al. (2014) $z \approx 0.3$ SDSS radio-loud AGN result, though our $1.0 < z \leq 1.5$ result of $1.7^{+2.2}_{-1.8} \times 10^{-7}$ Mpc^2 is $> 3\sigma$ higher than their $z \approx 1.1$ FIRST AGN result. This discrepancy is not too significant because our high-z detection is only at a 0.9σ confidence. Our results are also within $\approx 1\sigma$ of Greco et al. (2015) when comparing their results for galaxies with masses similar to ours. At smaller masses our results are consistent with theirs while at larger masses they find even greater tSZ signal, following the relation that tSZ signal increases with stellar mass. Ruan et al. (2015) also obtain values from stacks of SDSS quasars about an order of magnitude ($> 2\sigma$) higher than ours, although, according to Cen & Safarzadeh (2015b), the maximum AGN feedback signal from Ruan et al. (2015) can only be 25% of their quoted values. Furthermore, the $\approx 10^{11} M_{\odot}$ galaxy results from Ruan et al. (2015) are consistent with zero signal, while their $\approx 3 \times 10^{11} M_{\odot}$ galaxy results are $> 2\sigma$ larger than ours. Their high mass sample represents almost 3 times the mean mass of our galaxies, though, so the larger values may be indicative of the stellar mass$-$tSZ signal relation as well as the potential overestimation of the tSZ signal. We can compare our results to Cen & Safarzadeh (2015b) by multiplying their average Compton-y values over 1 arcmin by $\pi \times l^2_{\rm ang}$ (where $l^2_{\rm ang} = 3.18\,{\rm Gpc}^2$ for $z = 1.5$) to get Y values of $\approx 6.8{\times}10^{-7}$ Mpc^2 for their halo occupation distribution (HOD) model, and $\approx 4.2{\times}10^{-7}$ Mpc^2 for their Cen & Safarzadeh (2015a, CS) model, which places quasars in lower mass dark matter halos. This CS model value is within

$\approx 2\sigma$ of our results, and our measurements would favor the lower estimates of their CS model over their HOD model. Finally, both our low-z and high-z $E_{\rm therm}$ results are well within 1σ of the Crichton et al. (2016) SDSS radio-quiet quasar results.

With Equations (2.12) and (2.14) and the redshifts and masses from Table 2.3, we can also investigate theoretical thermal energies of the gas around elliptical galaxies due to both gravity and AGN feedback. We estimate the gravitational heating energy to be $E_{\rm therm,grav} = 3.6^{+3.6}_{-1.9} \times 10^{60}$ erg for our low-z sample and $E_{\rm therm,grav} = 3.0^{+3.0}_{-1.6} \times 10^{60}$ erg for our high-z sample. We therefore measure excess non-gravitational energies (for our results using Planck) of $E_{\rm therm,feed,dat} = 4.0^{+3.6}_{-4.3} \times 10^{60}$ erg for low-z and $E_{\rm therm,feed,dat} = 3.0^{+7.9}_{-7.0} \times 10^{60}$ erg for high-z. Plugging these into Equation (2.14) and solving for ϵ_k, we get feedback efficiencies of $7.5^{+6.5}_{-8.0}\%$ for low-z and $6.5^{+17.5}_{-15.5}\%$ for high-z. These values are very uncertain, though they are consistent with the suggested 5% (i.e., Scannapieco et al., 2005; Ruan et al., 2015).

2.7.5 Anderson-Darling Goodness-of-fit Test

The measurements described above depend on co-adding data from a large number of sources. In principle, however, there is additional information in the distribution of measured values that is lost through this process. For example, imagine a set of 1001 150 GHz measurements, 1000 of which contributed a negative signal of -2 μK arcmin^2 and one of which contributed a positive signal of 2000 μK arcmin^2. While the average value of these measurements would be zero, looking at the distribution of values would indicate strong evidence of a negative tSZ signal, offset by contamination from a single, overpowering positive source.

To quantify the additional information available by the full distribution of SPT data, we apply the same contaminant source modeling described above (i.e. Section 2.7.3) and use a goodness-of-fit test, the Anderson-Darling (A-D) test (Anderson &

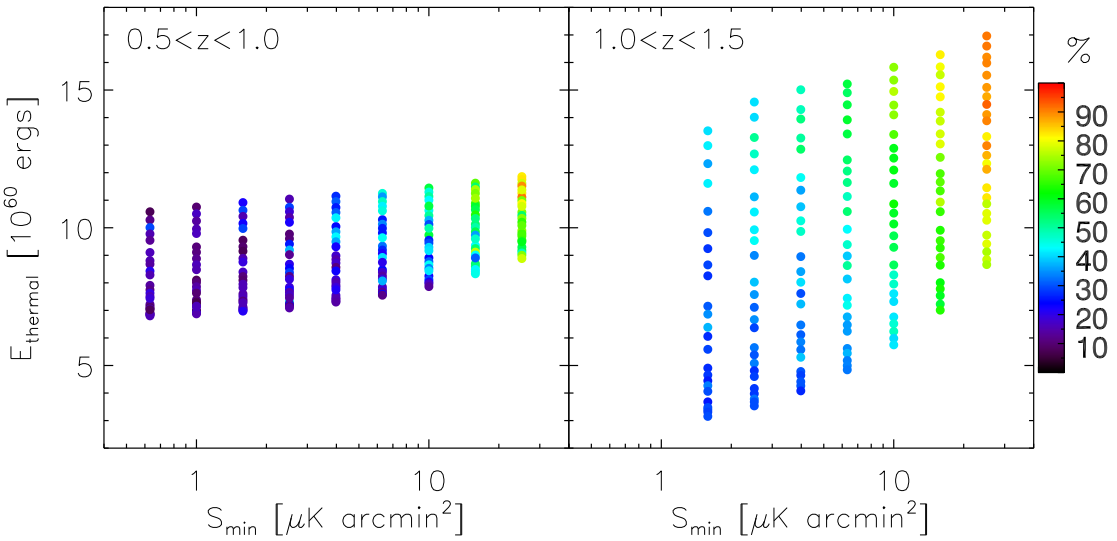

Figure 2.13: Same data points as Figure 2.11, but with the points colored according to the A-D statistics.

Darling, 1954), to find models that poorly fit the data. In this case we restrict our attention purely to the 1 arcmin resolution data used to construct Figure 2.9, without folding in the lower resolution Planck data as described in Section 2.7.4. To perform the test, we run through every pair of galaxy measurements (i.e., the 1 arcmin radius aperture sums at both 150 and 220 GHz) and find the fraction of galaxy measurements in each of the four quadrants around the pair of measurements (i.e., $(x < x_i, y < y_i)$; $(x < x_i, y > y_i)$; $(x > x_i, y < y_i)$; $(x > x_i, y > y_i)$; where x and y represent the co-add sum in each band, and i runs through all the galaxies). We will call these fractions $f_{i,j}$ where i specifies the galaxy ($i = [1, 2, \ldots, n]$, with n being the number of galaxies) and j specifies the quadrant ($j = [1, 2, 3, 4]$). In the same four quadrants we also find the fraction of model measurements, $F_{i,j}$. We therefore define our A-D statistic as:

$$S_{AD} = n \sum \frac{(f_{i,j} - F_{i,j})^2}{F_{i,j}(1 - F_{i,j})}, \tag{2.37}$$

where a smaller S_{AD} indicates a better fit between the model and the data.

Each model, as a function of $S_{\rm min}$, $\alpha_{\rm dust}$, and $\alpha_{\rm sync}$, will have a corresponding S_{AD}. In order to interpret our results, we follow the same process, but instead of using data

from our selected galaxies we use a random subset of the modeled sources, with the subset containing the same number of elements as the number of galaxies we are using for both redshift ranges. We do this 200 times each for four different combinations of $S_{\rm min}$, $\alpha_{\rm dust}$, and $\alpha_{\rm sync}$. We then define our confidence of the model fits, $P(< S_{AD})$, as the fraction of these subset calculations that are less than the corresponding S_{AD}. When defined in this way, P indicates our confidence that the model is not a good fit with the data. The fractions correspond to σ in the standard way (i.e., $1\sigma = 0.68$, $2\sigma = 0.95$, etc.).

As mentioned above, we only do these subset calculations for four sets of model parameters, which is due to the time-intensive nature of these computations. To get confidence values for every other set of model parameters, we simply do a linear interpolation between the four sets of model parameters we did use. The results are shown in Figure 2.13. They reveal that models with both the highest $S_{\rm min}$ and the highest $\alpha_{\rm dust}$ are disfavored up to $\approx 1.5\sigma$ (87%) confidence, with the trend much more pronounced in the high-z range. On the other hand, unlike the analysis using the Planck data, the A-D test primarily serves to constraint $S_{\rm min}$ rather than $E_{\rm thermal}$, meaning that it does not allow us to obtain significantly better constraints on feedback itself. Finally, we note that we also carried out a two-dimensional Kolmogorov-Smirnov test (e.g., Peacock, 1983) but it was far less constraining than the A-D test, and so we do not present it here.

2.8 Discussion

Since $z \approx 2$, star formation has occurred in progressively less massive galaxies, and AGNs have occurred around progressively less massive black holes. While these are fundamental observations of galaxy evolution, a consensus has yet to be reached about the physical processes that dictate them. The anti-hierarchical quenching of

galaxies and AGNs might be partially caused by stable virial shocks and gravitational heating due to infalling galaxies (e.g., Feldmann & Mayer, 2015), but most successful models invoke additional energy input, most likely from AGNs. In fact, strong quasar activity is known to launch rapid outflows of gas, and powerful radio jets are observed to play an important role in galaxy clusters, but the total energy released by these processes as a function of redshift and environment remains largely unknown. As our understanding of galaxy formation increasingly relies on understanding this feedback, it is apparent that we need increasingly sensitive observations to constrain it.

An extremely promising approach to making these constraints is co-adding the microwave background around a large number of sources to measure the signal imprinted by the tSZ effect. Several recent studies have applied this approach, making detections of galaxies at low redshifts ($z \lesssim 0.5$) and AGNs from $z = 0$ to 3, as summarized in Table 2.5. There are potential issues with each of these approaches, though. At low redshifts the additional gravitational heating from structure formation obscures the additional energy input from AGNs, while working with AGNs directly leads to problems of strong contamination from dust and synchrotron emission. These have motivated us to choose massive ($> 10^{11} M_{\odot}$) elliptical galaxies at moderate redshifts ($0.5 \leq z \leq 1.5$), where we expect these various limitations on the AGN feedback signal to be minimal, and to make our measurements using data from the South Pole Telescope, which has a ≈ 1 arcmin beam size well matched to the expected sizes of heated regions.

To construct a catalog of such large, $0.5 \leq z \leq 1.5$ elliptical galaxies, we made use of data from the BCS in the g, r, i, and z bands, as well as VHS data in the J, H, and K_s bands over a ≈ 43 deg^2 area overlapping with the public SPT fields. We separated galaxies from stars using a gzK_s color cut, and for each of the galaxies, we fit stellar population synthesis models to limit the sample to the most massive, $z \geq 0.5$ passive

galaxies. Furthermore, to limit the contamination of the tSZ signal, we removed all galaxies if they were within 4 arcmin of a galaxy cluster, an active AGN, a dusty Galactic molecular cloud, or a galaxy with strong dust emission. Finally, around the remaining sources, we co-added 150 and 220 GHz SPT maps that were optimally filtered for point sources. This alone gave us a tSZ detection in our low-z subset ($0.5 \leq z \leq 1.0$) 150 GHz band of $> 2\sigma$ significance. At the same time, we also had a $> 2\sigma$ contaminant signal in our low-z 220 GHz band, which is expected to also extend to and contaminate the 150 GHz band.

In order to account for this contamination, we modeled the potential contaminating sources using the SPT point source number counts from Mocanu et al. (2013), extrapolated them between the two bands, and used χ^2 statistics to get best-fit values across all reasonable parameter choices. This improved our low-z subset tSZ detection to 3.5σ significance. To even further constrain the contamination in our measurements, we stacked our galaxies in the four highest Planck bands as well, rejecting galaxies within 10 arcmin of potential contaminant sources. We again used χ^2 statistics to get best-fit values across all reasonable parameter choices, and found a low-z subset tSZ detection at 3.6σ significance, as well as a 0.9σ measurement of the tSZ signal in the high-z subset ($1.0 \leq z \leq 1.5$). A summary of all our results is found in Table 2.6.

In comparison with previous work measuring the tSZ signal around AGNs, we find a similar and slightly larger ($\approx 1\sigma$) tSZ signal than the lower redshift results of Gralla et al. (2014), and a significantly larger ($> 3\sigma$) signal than their higher redshift results. However, we find a much smaller tSZ signal than both the high and low redshift results of Ruan et al. (2015), although it is suspected that their values are significantly overestimated (e.g., Cen & Safarzadeh, 2015b). We also find a slightly smaller tSZ signal than the simulated results of Cen & Safarzadeh (2015b), and our

results favor their CS model, which associates quasars with lower mass dark matter halos. Our $E_{\rm therm}$ results are consistent with Crichton et al. (2016). In comparison with previous work measuring the tSZ signal around galaxies, we find a signal that is about 3.5 times less than the more massive galaxies used by Hand et al. (2011) which may be indicative of the stellar mass−tSZ signal relation. We find a signal within $\approx 1\sigma$ of the similar-mass galaxy stacks of Greco et al. (2015), though our results are consistent with their results at lower masses. The lower mass Ruan et al. (2015) galaxy signal is consistent with zero, while the higher mass (≈ 3 times our mean mass) results are $> 2\sigma$ larger than ours. This may again reflect the mass−tSZ signal relation as well as their potential overestimation of the tSZ signal. Finally, our low redshift results suggest an AGN feedback efficiency of $7.5^{+6.5}_{-8.0}\%$, which is consistent with the 5% value found in Ruan et al. (2015) and suggested by, for example, Scannapieco et al. (2005).

Measurements such as the one described here are likely to improve significantly in the near future. While the first public SPT-SZ data release (2011) covers a 95 deg^2 field with the 150 and 220 GHz bands, the upcoming full survey release will include a 2500 deg^2 field using bands at 95, 150, and 220 GHz. The much larger field will allow for a much larger set of galaxies to be co-added, vastly improving the signal-to-noise of the measurements, while the additional 95 GHz band will also allow for further constraints on contaminating signals. In addition to SPT, the Atacama Cosmology Telescope (ACT) has observed for four seasons from 2007 to 2011 using the Millimeter Bolometric Array Camera (MBAC) with bands at 148, 218, and 277 GHz, producing more than 90 TB of data (Dünner et al., 2013). In 2012 they released a 780 deg^2 temperature map at 148 GHz,[7] in 2014 they released a few thousand deg^2 at 148 and

[7]http://lambda.gsfc.nasa.gov/product/act/act_tmaps_info.cfm

218 GHz,[8] and more fields using all 3 bands will be released in the future. Measuring galaxies using ACT can compliment work using SPT because they observe both different and overlapping regions of the sky. Furthermore, the higher frequency 277 GHz band can also provide important help in constraining contaminant signal. In the future, separating out such contaminants will become even more practical, through surveys such as those to be undertaken by the upgraded ACT telescope (Advanced ACTPol) and the proposed Cerro Chajnantor Atacama Telescope (CCAT).[9]

Another approach to constraining AGN feedback is through deep measurements of smaller samples of galaxies identified as the most interesting using large radio telescopes. In this case rather than co-adding as many galaxies as possible, one would select a handful of the most promising galaxies for detecting AGN feedback. The Goddard IRAM Superconducting Two Millimeter Camera (GISMO) and the New IRAM KIDs Array (NIKA) are powerful new instruments mounted on the Institute de Radioastronome Millimetrique (IRAM) 30 meter telescope[10] that may prove useful for this purpose. Also promising is the National Radio Astronomy Observatories (NRAO) Green Bank Telescope (GBT), whose Continuum Backend operates at lower frequencies where the tSZ signal is roughly three times larger. On the other hand, interferometers appear to be less suited to constraining AGN heating, because they are more likely to resolve the affected regions and thus be limited by surface brightness concerns. Nevertheless, several interferometers may prove useful for AGN feedback studies, including the IRAM interferometer, the Combined Array for Research in Millimeter-wave Astronomy (CARMA), and the Atacama Large Millimeter/submillimeter Array (ALMA).

[8] http://lambda.gsfc.nasa.gov/product/act/act_maps2013_info.cfm

[9] http://www.ccatobservatory.org/

[10] http://www.iram-institute.org/EN/30-meter-telescope.php

Finally, tSZ simulations and observations can be combined to produce weighted stacks that are adapted to be as sensitive as possible to the differences between feedback models. This is because with a suite of simulations in hand, one can not only perform stacks of the tSZ signal around simulated galaxies with exactly the same mass, redshift, and age distribution as in a given observational sample, but also vary the weights applied to such stacks so as to arrive at the combination that allows for the observations to best discriminate between competing models. We are only now beginning to map out the history of AGN feedback through measurements of the tSZ effect.

Chapter 3

SEARCHING FOR FOSSIL EVIDENCE OF AGN FEEDBACK IN WISE-SELECTED STRIPE-82 GALAXIES BY MEASURING THE THERMAL SUNYAEV-ZEL'DOVICH EFFECT WITH THE ATACAMA COSMOLOGY TELESCOPE

3.1 Introduction

Galaxy formation was long expected to proceed hierarchically, with larger galaxies forming at later times when larger dark matter halos coalesce and gas has longer to cool and condense (e.g. Rees & Ostriker, 1977; White & Frenk, 1991; Richstone et al., 1998; Cattaneo et al., 1999; Kauffmann & Haehnelt, 2000; Menci, 2006). However, an increasing amount of observational evidence suggests recent anti-hierarchical trends in both galaxy and active galactic nucleus (AGN) evolution (Kang et al., 2016; Rosas-Guevara et al., 2016; Siudek et al., 2016). For example, beyond $z \approx 2$ the typical mass of star-forming galaxies has dropped by more than a factor of $\approx$3 (Cowie et al., 1996; Brinchmann et al., 2004; Kodama et al., 2004; Bauer et al., 2005; Bundy et al., 2005; Feulner et al., 2005; Treu et al., 2005; Papovich et al., 2006; Noeske et al., 2007; Cowie & Barger, 2008; Drory & Alvarez, 2008; Vergani et al., 2008), while the characteristic AGN luminosity has dropped by more than a factor of $\approx$10 (Pei, 1995; Ueda et al., 2003; Barger et al., 2005; Buchner et al., 2015). To explain these trends, it is widely suggested that galaxy evolution models require additional heating of the circumgalactic medium by energetic AGN feedback (Merloni, 2004; Scannapieco & Oh, 2004; Scannapieco et al., 2005; Bower et al., 2006; Neistein et al., 2006; Thacker et al., 2006; Sijacki et al., 2007; Merloni & Heinz, 2008; Chen et al., 2009; Hirschmann

et al., 2012; Mocz et al., 2013; Hirschmann et al., 2014; Lapi et al., 2014; Schaye et al., 2015; Keller et al., 2016). This typically involves an energetic AGN outflow caused by radiation pressure or jets that blow material out of the galaxy, heating the nearby intergalactic medium enough to suppress further generations of stars and AGNs.

In fact, there is abundant observational evidence of AGN feedback in action in galaxy clusters (Schawinski et al., 2007; Rafferty et al., 2008; Fabian, 2012; Farrah et al., 2012; Page et al., 2012; Teimoorinia et al., 2016). Most notably, the centers of clusters are more likely to contain galaxies that host large radio-loud jets of AGN-driven material (Burns, 1990; Best et al., 2005; McNamara et al., 2005), whose energies are comparable to those needed to stop the gas from cooling (e.g. Simionescu et al., 2009). Furthermore, AGN feedback from the central cD galaxies in clusters increases in proportion to the cooling luminosity, as expected in an operational feedback loop (e.g. Bîrzan et al., 2004; Rafferty et al., 2006).

Direct measurements of AGN feedback in less dense environments are much less common, primarily because of the relatively high redshifts and faint signals involved, although evidence of AGN feedback has also been seen in relatively nearby galaxies (Tombesi et al., 2015; Lanz et al., 2016; Schlegel et al., 2016). For example, broad absorption-line outflows are observed as blueshifted troughs in the rest-frame spectra of $\approx$20% of all of quasars (Hewett & Foltz, 2003; Ganguly & Brotherton, 2008; Knigge et al., 2008), but quantifying AGN feedback requires estimating mass-flow and the energy released by these outflows (e.g. Wampler et al., 1995; de Kool et al., 2001; Hamann et al., 2001; Feruglio et al., 2010; Sturm et al., 2011; Veilleux et al., 2013). These quantities can only be computed in cases for which it is possible to estimate the distance to the outflowing material from the central source, which is often highly uncertain. While these measurements have been carried out for a select set of objects (e.g. Chartas et al., 2007; Moe et al., 2009; Dunn et al., 2010; Greene et al., 2012;

Borguet et al., 2013; Chamberlain et al., 2015), it is still unclear how these results generalize to AGNs as a whole. Furthermore, it is still an open question as to whether AGN outflows triggered by galaxy interactions in massive, high-redshift galaxies actually quench star formation (e.g. Fontanot et al., 2009; Pipino et al., 2009; Debuhr et al., 2010; Ostriker et al., 2010; Faucher-Giguère & Quataert, 2012; Newton & Kay, 2013; Feldmann & Mayer, 2015; Bongiorno et al., 2016).

One way to get around the high redshifts and faint signals involved in AGN feedback measurements is to stack measurements of the cosmic microwave background (CMB) radiation. At angular scales smaller than $\approx$5 arcmin, Silk damping washes out the primary CMB anisotropies (Silk, 1968; Planck Collaboration et al., 2015d), leaving room for secondary anisotropies such as the Sunyaev-Zel'dovich (SZ) effect, where CMB photons interact with hot, ionized gas (Sunyaev & Zeldovich, 1970, 1972). When the gas has a bulk velocity, CMB photons interacting with electrons in the gas experience a Doppler boost, resulting in frequency-independent fluctuations in the CMB temperature, known as the kinematic Sunyaev-Zel'dovich (kSZ) effect. Although the kSZ effect does not measure the energy of the gas, it can be used to detect the ionized gas profile within dark matter halos, thereby providing information on where hot gas is located around galaxies. This can be useful for understanding how AGN feedback heats up gas and moves it around (Battaglia et al., 2010). Several recent studies have made significant measurements of the kSZ effect in galaxy clusters by stacking CMB observations (e.g. Planck Collaboration et al., 2016; Schaan et al., 2016; Soergel et al., 2016).

If the gas is sufficiently heated, inverse Compton scattering coupled with the thermal motions of electrons will shift the CMB photons to higher energies. This thermal Sunyaev-Zel'dovich (tSZ) effect directly depends on the temperature of the free electrons that the CMB radiation passes through, and it has a unique redshift-

independent spectral signature that makes it well suited for measuring the gas heated through AGN feedback (Voit, 1994; Birkinshaw, 1999; Natarajan & Sigurdsson, 1999; Platania et al., 2002; Lapi et al., 2003; Chatterjee & Kosowsky, 2007; Chatterjee et al., 2008; Scannapieco et al., 2008; Battaglia et al., 2010). Individual tSZ distortions per source are very small, however, so a stacking analysis must be performed on many measurements in order to derive a significant signal.

This method has been used previously by a handful of studies in relation to AGNs and galaxies. Chatterjee et al. (2010) found a tentative detection of quasar feedback using the Sloan Digital Sky Survey (SDSS) and Wilkinson Microwave Anisotropy Probe (WMAP), though the significance of AGN feedback in their measurements is disputed (Ruan et al., 2015). Hand et al. (2011) stacked >2300 SDSS-selected "luminous red galaxies" in data from the Atacama Cosmology Telescope (ACT) and found a $2.1\sigma - 3.8\sigma$ tSZ detection after selecting radio-quiet galaxies and binning them by luminosity. Planck Collaboration et al. (2013) investigated the relationship between tSZ signal and stellar mass using $\approx 260,000$ "locally brightest galaxies" with significant results, especially with stellar masses $\gtrsim 10^{11} M_{\odot}$. Gralla et al. (2014) stacked data from the ACT at the positions of a large sample of radio AGNs selected at 1.4 GHz to make a 5σ detection of the tSZ effect associated with the haloes that host active AGNs. Greco et al. (2015) used Planck full-mission temperature maps to examine the stacked tSZ signal of 188,042 "locally brightest galaxies" selected from the SDSS Data Release 7, finding a significant measurement of the stacked tSZ signal from galaxies with stellar masses above $\approx 2 \times 10^{11} M_{\odot}$. Ruan et al. (2015) stacked Planck tSZ Compton-y maps centered on the locations of 26,686 spectroscopic quasars identified from SDSS to estimate the mean thermal energies in gas surrounding such $z \approx 1.5$ quasars to be $\approx 10^{62}$ erg, although the significance of AGN feedback in their measurements has also been disputed (Cen & Safarzadeh, 2015b). Crichton

et al. (2016) stacked >17,000 radio-quiet quasars from the SDSS in ACT data and found 3σ evidence for the presence of associated thermalized gas and 4σ evidence for the thermal coupling of quasars to their surrounding medium. Spacek et al. (2016) stacked 937 massive elliptical galaxies using the South Pole Telescope (SPT) and made a 3.6σ detection of the tSZ effect at a magnitude suggesting an excess of non-gravitational thermal energy, possibly due to AGN feedback. These tSZ AGN feedback measurements continue to be promising, and in this paper we will especially focus on the methods and results from Spacek et al. (2016).

As evidenced above, quasars are a popular target for measuring AGN feedback due to their brightness and their active feedback processes, but they have drawbacks due to their relative scarcity and the contaminating emission they contain that obscures the tSZ signatures of AGN feedback. In this paper, we follow Spacek et al. (2016) and focus on measuring co-added tSZ distortions in the CMB around massive ($\geq 10^{11} M_{\odot}$) quiescent elliptical galaxies at moderate redshifts ($0.5 \leq z \leq 1.5$). To accomplish this, we use data from the Wide-Field Infrared Survey Explorer (WISE; Wright et al., 2010), SDSS (Alam et al., 2015), and ACT (Dünner et al., 2013). These galaxies contain almost no dust and are numerous on the sky, making them well-suited for co-adding in large numbers in order to obtain good constraints on the energy stored in the surrounding gas.

The structure of this paper is as follows: in Section 3.2, we explain our method of measuring the thermal energy around galaxies using the tSZ effect and how that might relate to non-gravitational heating by AGN feedback. In Section 3.3, we discuss the data that we use to both select galaxies and make our tSZ measurements. In Section 3.4, we outline our galaxy selection process and how we estimate the physical parameters of the galaxies. In Section 3.5, we explain how we filter the ACT images. In Section 3.6, we discuss our stacking procedure and results. In Section 3.7, we use

a χ^2 analysis to model and remove contaminant signal, and in Section 3.8 we do the same but with data from Planck included. In Section 3.9, we summarize our results, discuss the implications for AGN feedback, and provide conclusions.

Throughout this work, we adopt a ΛCDM cosmological model with parameters (from Planck Collaboration et al., 2015d), $h = 0.68$, $\Omega_0 = 0.31$, $\Omega_\Lambda = 0.69$, and $\Omega_b = 0.049$, where h is the Hubble constant in units of 100 km s^{-1} Mpc^{-1}, and Ω_0, Ω_Λ, and Ω_b are the total matter, vacuum, and baryonic densities, respectively, in units of the critical density. All of our magnitudes are quoted in the AB system (i.e. Oke & Gunn, 1983).

3.2 Methods

The tSZ effect is the process by which CMB photons gain energy when passing through ionized gas (Sunyaev & Zeldovich, 1970, 1972) through inverse Compton scattering with energetic electrons. The resulting CMB anisotropy has a distinctive frequency dependence, which causes a deficit of photons at frequencies below $\nu_{\rm null} = 217.6\,{\rm GHz}$ and an excess of photons above $\nu_{\rm null}$. The change in CMB temperature ΔT as a function of frequency due to the (nonrelativistic) tSZ effect is

$$\frac{\Delta T}{T_{\rm CMB}} = y\left(x\frac{e^x+1}{e^x-1} - 4\right), \tag{3.1}$$

where the dimensionless Compton-y parameter is defined as

$$y \equiv \int dl\, \sigma_T \frac{n_e k\,(T_e - T_{\rm CMB})}{m_e c^2}, \tag{3.2}$$

where σ_T is the Thomson cross section, k is the Boltzmann constant, m_e is the electron mass, c is the speed of light, n_e is the electron number density, T_e is the electron temperature, $T_{\rm CMB}$ is the CMB temperature (we use $T_{\rm CMB} = 2.725$ K), the integral is performed over the line-of-sight distance l, and the dimensionless frequency x is

given by $x \equiv \frac{h\nu}{kT_{\rm CMB}} = \frac{\nu}{56.81\,{\rm GHz}}$, where h is the Planck constant. We can calculate the total excess thermal energy $E_{\rm therm}$ associated with a source by integrating Equation (3.2) over a region of sky around the source, as detailed in Spacek et al. (2016), and combining the result with Equation (3.1) to get $E_{\rm therm}$ as a function of x and ΔT. This gives

$$E_{\rm therm} = \frac{1.1 \times 10^{60}{\rm ergs}}{x\frac{e^x+1}{e^x-1} - 4} \left(\frac{l_{\rm ang}}{\rm Gpc}\right)^2 \frac{\int \Delta T(\boldsymbol{\theta}) d\boldsymbol{\theta}}{\mu{\rm K\ arcmin}^2}. \tag{3.3}$$

To compare the measured energies above with the expectations from models of feedback, we use the simple models of gas heating with and without AGN feedback worked out in Spacek et al. (2016). For purely gravitational heating, we can assume that the gas collapses and virializes along with an encompassing spherical halo of dark matter. The gas is shock-heated during gravitational infall to a virial temperature $T_{\rm vir}$, and if we approximate the gas as isothermal at this temperature we can estimate its total thermal energy as

$$\begin{aligned} E_{\rm therm,gravity} &= \frac{3kT_{\rm vir}}{2}\frac{\Omega_b}{\Omega_0}\frac{M}{\mu m_p} \\ &= 1.5 \times 10^{60}\,{\rm erg}\, M_{13}^{5/3}(1+z), \end{aligned} \tag{3.4}$$

where m_p is the proton mass, $\mu = 0.62$ is the average particle mass in units of m_p, and M_{13} is the mass of the halo in units of $10^{13}M_\odot$. We can convert from halo mass to the stellar mass of the galaxies we will be measuring if we use the observed relation between black hole mass and halo circular velocity v_c from Ferrarese (2002), convert the black hole mass to its corresponding bulge dynamical mass using a factor of 400 (Marconi & Hunt, 2003), use the fact that $v_c = (GM/R_{\rm vir})^{1/2} = 254\,{\rm km\,s^{-1}}\, M_{13}^{1/3}(1+z)^{1/2}$, where G is the gravitational constant, and take $M_{\rm stellar} \propto v_c^5$. As shown in Spacek et al. (2016), this gives $M_{\rm stellar} = 2.8^{+2.4}_{-1.4} \times 10^{10} M_\odot\, M_{13}^{5/3}(1+z)^{5/2}$, and substituting this into Equation (3.4) yields

$$E_{\rm therm,gravity} = 5.4^{+5.4}_{-2.9} \times 10^{60}\,{\rm erg}\,\frac{M_{\rm stellar}}{10^{11}M_\odot}(1+z)^{-3/2}. \tag{3.5}$$

This is the total thermal energy expected around a galaxy of stellar mass $M_{\rm stellar}$ ignoring both radiative cooling, which will decrease $E_{\rm therm}$, and AGN feedback, which will increase it.

For heating due to AGN feedback it is difficult to be precise because little is known about the dominant mechanism by which AGN feedback operates, and as a result there are many models, each of which leads to somewhat different signatures in our data. We can, however, try to estimate the overall magnitude of AGN feedback heating by making use of the simple model described in Scannapieco & Oh (2004). This is characterized as the heating of gas by a fraction ϵ_k of the total bolometric luminosity of the AGN, where the black hole shines at the Eddington luminosity (1.2×10^{38} erg s^{-1} $M_\odot^{-1}$) for a time $0.035\, t_{\rm dynamical}$, with $t_{\rm dynamical} \equiv R_{\rm vir}/v_c = 2.6\,{\rm Gyr}\,(1+z)^{-3/2}$, where $R_{\rm vir}$ is the halo virial radius. This gives

$$E_{\rm therm,feedback} = 4.1 \times 10^{60}\,{\rm erg}\,\epsilon_{k,0.05}\,\frac{M_{\rm stellar}}{10^{11} M_\odot}\,(1+z)^{-3/2}, \tag{3.6}$$

where $\epsilon_{k,0.05} \equiv \epsilon_k/0.05$. In this case, 5% is a typical, though still very uncertain, efficiency needed to achieve anti-heirarchical galaxy evolution through effective feedback (e.g. Scannapieco & Oh, 2004; Thacker et al., 2006; Costa et al., 2014).

It is evident that our simple model of feedback energy falls within the errors of our model for gravitational energy, indicating that the differences between models with and without AGN feedback are subtle. Detailed simulations beyond the scope of this paper will be needed to make precise predictions regarding particular AGN feedback models. Even so, our models above are roughly consistent with more sophisticated models (e.g. Thacker et al., 2006; Chatterjee et al., 2008), and we will therefore use them to provide a general context for our results.

3.3 Data

In order to select a large number of galaxies for our stacking analysis, we wanted to use a large region of the sky that was covered with a wide wavelength range of telescope surveys and included microwave data for our tSZ measurements. We therefore chose the SDSS Stripe-82 region, which is covered by many surveys, including ultraviolet, visible, and infrared data from the SDSS, infrared data from the WISE All-Sky Data Release, and microwave data from the ACT. We also used the extensive pre-existing source catalogs corresponding to the SDSS and WISE data.

Our SDSS data were taken from Data Release 12 (DR12) of the third generation of the Sloan Digital Sky Survey (SDSS-III; Alam et al., 2015). Since 2000 the SDSS has used a 2.5 m wide-field telescope at Apache Point Observatory in New Mexico to image roughly one-third of the sky (31,637 $\deg^2$), and the catalog contains information on over 1 billion objects. The SDSS bands we used are u, g, r, i, and z, with average wavelengths of 355.1, 468.6, 616.5, 748.1, and 893.1 nm, respectively, and an average point spread function (PSF) width of 1.4 arcsec in r-band.[11] Stripe-82 is a 2.5° wide stripe along the celestial equator that was imaged multiple times, resulting in deeper SDSS data than the main survey. The general Stripe-82 region runs from $-1.25°$ to $1.25°$ decl. and $-65°$ to $60°$ R.A., with an area of $\approx$312 $\deg^2$.[12]

The WISE All-Sky Data Release contains data from the full WISE mission in 2010 using the 0.4 m space telescope (Wright et al., 2010). The four WISE infrared bands are labelled $W1$, $W2$, $W3$, and $W4$, and are centered at 3.4, 4.6, 12, and 22 μm, respectively, with average PSF full-width-at-half-maximum (FWHM) values of

[11] http://classic.sdss.org/dr7/

[12] http://classic.sdss.org/dr7/coverage/sndr7.html

6.1, 6.4, 6.5, and 12.0 arcsec, respectively. The corresponding source catalog contains over 500 million sources with a signal-to-noise ratio (S/N) >5.[13]

The ACT is a 6 m telescope on Cerro Toco in Chile which started observing in 2007. It was equipped with the Millimeter Bolometric Array Camera (MBAC), with bands at 148, 220, and 277 GHz (Dünner et al., 2013). The data used in this paper covering the equatorial Stripe-82 region are from ACT seasons 3 and 4 (2009 and 2010) using the 148 and 220 GHz bands.[14] These have beam FWHM values of ≈1.44 and ≈1.08 arcmin, respectively. We used the data designated as "src_free," where flux from point sources has been removed. Since both seasons cover the same region of sky, we are able to average them together to increase our S/N.

The ACT bands at 148 and 220 GHz are ideal for our tSZ measurements because 148 GHz is close to the peak of the undistorted CMB spectrum (160 GHz) and will see a significant decrement, while 220 GHz is very close to a frequency where the tSZ effect has no effect ($\nu_{\rm null} = 217.6\,{\rm GHz}$). Equation (3.1) can be rewritten for the ACT bands after integrating over their filter curves and solving for the Compton-y parameter. The filter curves are taken from Swetz et al. (2011). This gives

$$y = -0.38\,\frac{\Delta T_{148}}{1{\rm K}} \qquad \text{and} \qquad y = 5.4\,\frac{\Delta T_{220}}{1{\rm K}}, \tag{3.7}$$

where ΔT_{148} and ΔT_{220} are the temperature anisotropies at 148 and 220 GHz. We can similarly integrate Equation (3.3) over the ACT 148 GHz filter curve to get the total thermal energy surrounding a galaxy as a function of the 148 GHz tSZ decrement,

$$E_{\rm therm} = -1.1 \times 10^{60}{\rm ergs}\left(\frac{l_{\rm ang}}{\rm Gpc}\right)^2 \frac{\int \Delta T_{148}(\boldsymbol{\theta}) d\boldsymbol{\theta}}{\mu{\rm K\ arcmin}^2}. \tag{3.8}$$

[13]http://wise2.ipac.caltech.edu/docs/release/allsky/

[14]http://lambda.gsfc.nasa.gov/product/act/act_prod_table.cfm

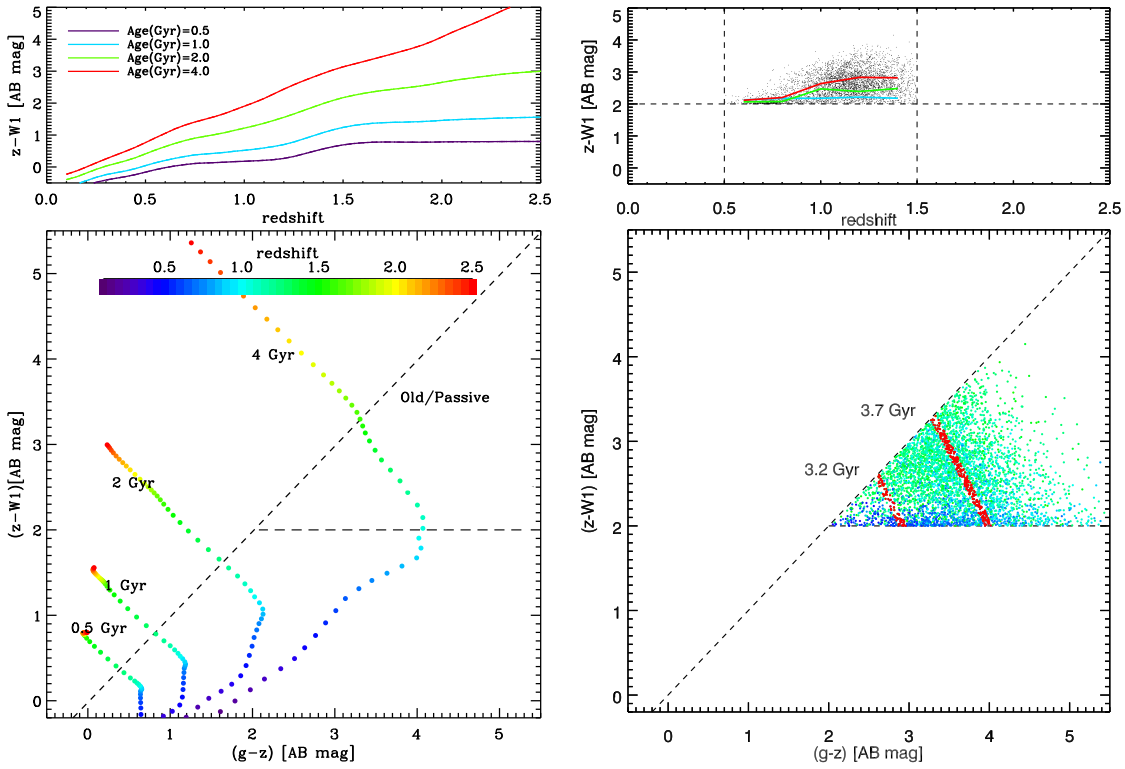

Figure 3.1: (Left) These two plots show expected galaxy tracks according to models from Bruzual & Charlot (2003). The bottom plot shows the color-color selection of our $gzW1$ diagram in analogy to the BzK selection of Daddi et al. (2004), with dashed lines corresponding to Equations (3.9) and (3.10). Shown are tracks in redshift for fixed ages and assuming a star formation timescale $\tau \simeq 0.5$ Gyr. In the absence of extinction, our selection region will choose $\gtrsim 2$ Gyr population with $1 \lesssim z \lesssim 2$. The top plot shows the $z - W1$ evolution as a function of age and redshift. (Right) The same plots as on the left with the same scales and colors, but with our actual data. The colored lines in the top plot represent mean $z - W1$ values for 0.1-width redshift bins for each age. The red regions in the bottom plot represent roughly the slopes of the age lines in the left plot, and the ages given are mean ages for each red region.

3.4 Galaxy Selection and Characterization

In order to select galaxies best suited for our tSZ measurements, we have followed the selection criteria in Spacek et al. (2016). We therefore have restricted our attention to massive elliptical galaxies with redshifts $0.5 \leq z \leq 1.5$. Galaxies are initially selected from the WISE catalog to have equatorial coordinates that lie within SDSS

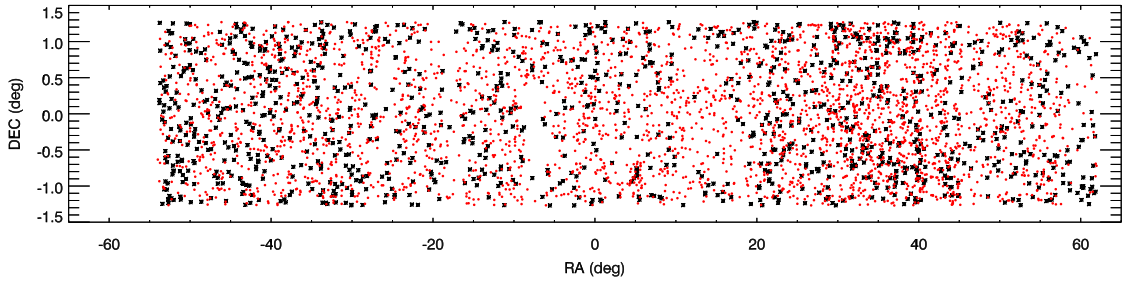

Figure 3.2: Location on the sky of our final selection of galaxies. Black represents $0.5 \leq z \leq 1.0$ (1179 galaxies) and red represents $1.0 \leq z \leq 1.5$ (3274 galaxies). Note that this image has been stretched vertically for clarity, as the true aspect ratio of the field is $\approx 1/60$.

Stripe-82 ($306^\circ < \alpha_{2000} < 62^\circ$ and $-1.27^\circ < \delta_{2000} < 1.27^\circ$). A cut was made requiring S/N > 5 in both $W1$ and $W2$.

We incorporated the SDSS bands in order to perform a color selection analogous to the passive BzK selection of Daddi et al. (2004) using $g - z$ and $z - W1$ colors. This $gzW1$-selection is illustrated for several example spectral energy distributions (SEDs) from Bruzual & Charlot (2003) in the left plots of Figure 3.1. The selection lines (in the AB magnitude system) are

$$(z - W1) \leq (g - z) - 0.02, \tag{3.9}$$

and

$$(z - W1) \geq 2.0, \tag{3.10}$$

which define the wedge in the upper right of the bottom plots in Figure 3.1. The color-selection was necessary to reduce the sample to a useable size. Galaxies whose colors lie in this wedge should be old and passively evolving galaxies at $1 \lesssim z \lesssim 2$. Following the WISE and $gzW1$ criteria, and selecting only WISE sources with unique SDSS-DR12 matches, we arrived at a sample of ≈30,000 galaxies which were further pared down using redshift and SED parameters. We emphasize that we are after a highly reliable sample and are willing to sacrifice completeness in the interest of purity.

Cut	z	N	$\langle z \rangle$	$\langle l^2_{\rm ang} \rangle$ (Gpc^2)	$\langle$M$\rangle$ (M$_\odot$)	$\langle$Age$\rangle$ (Gyr)	$\langle$L$_{W1}\rangle$ (erg s^{-1} Hz^{-1})	$\langle z \rangle_{\rm M}$	$\langle l^2_{\rm ang} \rangle_{\rm M}$ (Gpc^2)
All	$0.5-1.0$	1179	0.83	2.56	7.81×10^{11}	3.80	7.83×10^{30}	0.86	2.61
All	$1.0-1.5$	3274	1.20	3.04	10.1×10^{11}	3.56	12.8×10^{30}	1.21	3.05
Planck	$0.5-1.0$	227	0.83	2.55	6.93×10^{11}	3.63	7.04×10^{30}	0.86	2.60
Planck	$1.0-1.5$	529	1.21	3.05	9.68×10^{11}	3.44	12.4×10^{30}	1.21	3.05

Table 3.1: Mean and mass-averaged values for several relevant galaxy parameters in the two final redshift ranges. "All" represents our complete, final galaxy sample, and "Planck" represents our final galaxy sample with further cuts applied, as discussed in Section 3.8.

Photometric redshifts were computed with extinction-corrected SDSS *ugriz* and WISE $W1$ and $W2$ photometry using EAZY (Brammer et al., 2008). The $W3$ and $W4$ bands were omitted since they are not comparably deep and are dominated by a warm/hot dust component that obscures the stellar component of the target galaxies that we are after. We then applied the constraint that $0.5 \leq z \leq 1.5$. The seven-band SEDs were fit with Bruzual & Charlot (2003) exponentially declining star formation rate (with timescale τ) models. We only used those objects with reliable SED fits by selecting galaxies with reduced $\chi^2 \leq 5$. We applied further selections based on the results of the SED fits by taking only galaxies with ages ≥ 1 Gyr and specific star formation rates ≤ 0.01 Gyr^{-1}. This ensured that we were choosing older galaxies that were not actively forming stars, especially excluding dusty starbursts which made it through the color-cuts. This gave a sample of ≈10,000 galaxies, which were then pruned of known contaminants to the tSZ signal.

In order to estimate the possible contamination of our sample, we can appeal to morphological measurements where the same SED selection criteria as above are applied. Unfortunately, we cannot use the sample we have selected from Stripe-82 because Hubble Space Telescope (HST) resolution is required to classify galaxies at

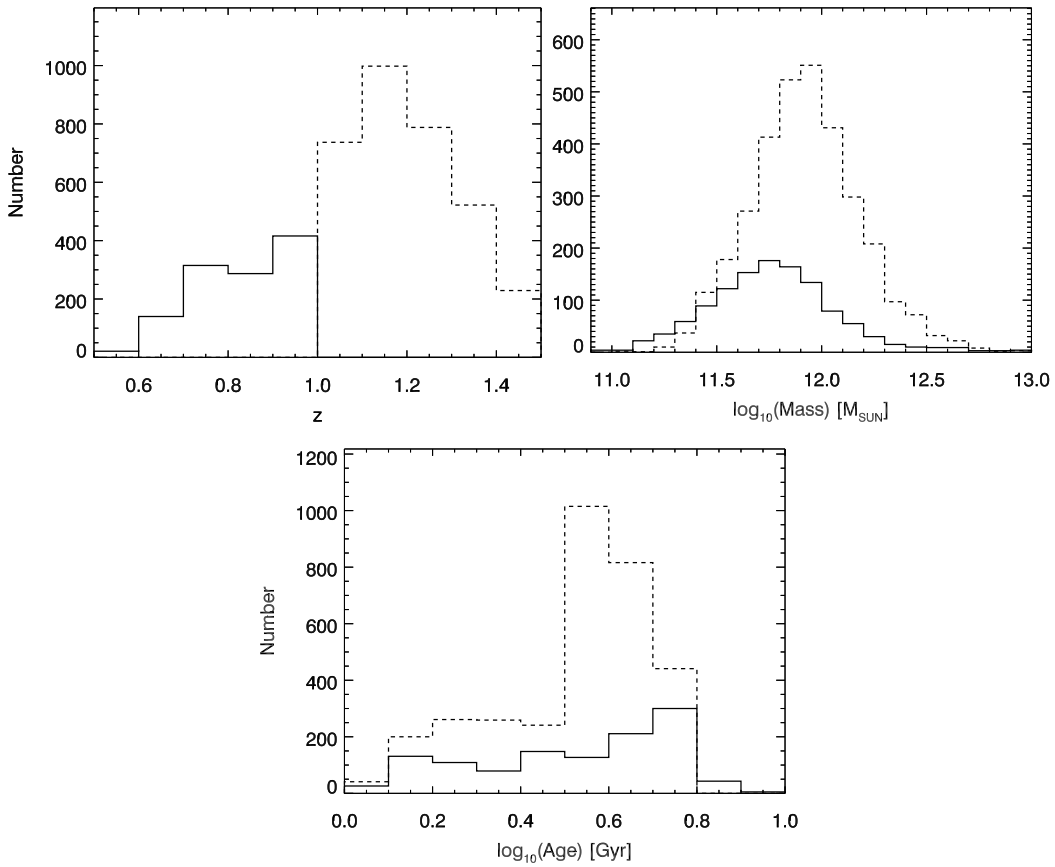

Figure 3.3: Redshift, mass, and age distributions of our final selection of galaxies. Solid lines represent $0.5 \leq z \leq 1.0$ (1179 galaxies) and dashed lines represent $1.0 \leq z \leq 1.5$ (3274 galaxies). The redshift histogram has a bin size of 0.1, and the mass and age histograms have bin sizes of 0.1 in log-space.

$0.5 \lesssim z \lesssim 1.5$. Instead we use the largest HST survey available, CANDELS (Grogin et al., 2011; Koekemoer et al., 2011). We use the SED fit parameters from Skelton et al. (2014) and Sersic function fits from van der Wel et al. (2012), who used GALFIT (Peng et al., 2002) to fit the 2D light profiles to the CANDELS HST images in the H_{F160W}-band. Since galaxies with stellar mass greater than $10^{11} M_{\odot}$ are rare on the sky and even the largest HST survey is significantly smaller than the $\approx$300 deg^2 Stripe-82 survey, we lower our mass limit to $M \geq 10^{10} M_{\odot}$ for this exercise. We choose all galaxies with age greater than 1 Gyr and SSFR < 0.01 Gyr^{-1}. Additionally, we require a reliable Sersic fit from van der Wel et al. (2012) and choose Sersic index

$n > 2.5$ to be representative of "elliptical" galaxies. For samples of 364 and 346 galaxies, we find that 82% and 78% are $n > 2.5$ galaxies at $0.5 \leq z \leq 1.0$ and $1.0 \leq z \leq 1.5$, respectively. If we remove the age and SSFR requirements we get only 45% and 30% $n > 2.5$ ellipticals at low and high redshift, respectively. Therefore, assuming morphology and SED parameters are correlated in this way, we estimate that our sample of old galaxies that are not actively forming stars is $\simeq 80\%$ pure. Removing this 20% contamination is part of the focus of Sections 3.7 and 3.8.

The most significant contaminants that must be removed are known AGN and galaxy clusters. We therefore removed sources from the ROSAT Bright and Faint Source catalogs (BSC and FSC; Voges et al., 1999). We additionally removed known clusters from ROSAT (Piffaretti et al., 2011). Clusters selected via the SZ effect would completely counter our measurements, so we removed both known Planck (Planck Collaboration et al., 2015e) and ACT (Marriage et al., 2011; Hasselfield et al., 2013) clusters. X-ray sources from XMM-Newton and Chandra (LaMassa et al., 2013), sources from the AKARI/FIS Bright Source Catalog (Yamamura et al., 2010), and sources from the AKARI/IRC Point Source Catalog (Ishihara et al., 2010) were also removed. We also removed Galactic molecular clouds by cross-matching with the Planck Catalogue of Galactic Cold Clumps (Planck Collaboration et al., 2015f), compact sources from the nine-band Planck Catalog of Compact Sources (Planck Collaboration et al., 2014), and removed all sources from the IRAS Point Source Catalog (Helou & Walker, 1988, pp. 1-265) and radio sources from Best & Heckman (2012). We also verified that none of our sources satisfied the "$W1W2$-dropout" criteria for extremely luminous infrared galaxies of Eisenhardt et al. (2012). In all cases, sources with a possible contaminant within 4.0 arcmin, approximately double our region of interest around each source, were flagged and those sources were removed

from further consideration. This left ≈7200 massive, quiescent, $0.5 \leq z \leq 1.5$ galaxies that are away from known potential contaminants.

Finally, to make sure we were selecting galaxies with the most reliable parameters, we limited the AB magnitude errors in the SDSS bands ($ugriz$), with mag_error < 1.5 mag, required $\log_{10}$(SSFR) to be finite, and limited the galaxy stellar mass as $M < 10^{13} M_{\odot}$. This resulted in a final selection of 4453 galaxies to include in our tSZ stacks. To narrow down our measurements in redshift space we split our galaxy sample into two redshift bins: a "low-z" bin with 1179 $0.5 \leq z < 1.0$ galaxies and a "high-z" bin with 3274 $1.0 \leq z \leq 1.5$ galaxies. We show how our final galaxy selection fits in with our original SED color selection in the right plots of Figure 3.1. The locations of the final selection of galaxies is shown in Figure 3.2. The mass, redshift, and age distribution of the final sample is shown in Figure 3.3. Mean and mass-averaged values for redshift, angular diameter distance, mass, age, and $W1$ luminosity in both redshift bins are given in Table 3.1.

3.5 Filtering

Before stacking the ACT data around our selected galaxies, we needed to filter the ACT maps to remove the primary CMB anisotropy and maximize the signal-to-noise at the spatial scales we are measuring. An ideal Fourier-space point source filter is given by $\psi = \frac{\tau}{P} \left[\int d^2k \frac{\tau^2}{P} \right]^{-1}$, where τ is the Fourier-space source profile and P is the Fourier-space noise covariance matrix (e.g. Haehnelt & Tegmark, 1996). For the source profile we assumed a slightly extended source such that $\tau = B \times G$, where B is the Fourier-space beam function and G is a Fourier-space Gaussian function. We have also approximated the noise P as the ACT noise power spectra given in Das et al. (2014) for seasons 3 and 4 plus the CMB power spectrum. We therefore have approximated the filter as

$$\psi \approx \frac{B \times G}{N} \left[\int d^2k \frac{(B \times G)^2}{N} \right]^{-1}, \tag{3.11}$$

where N is the Fourier-space CMB+noise power spectrum. We did this for each band in each season and then averaged the two seasons together, resulting in an averaged filter for each band. For G we chose a Gaussian with a FWHM of 1.5 arcmin to represent a slightly extended source. This is because our signal of interest is from hot gas within and surrounding the galaxies that likely represents the cumulative heating due to multiple cycles of AGN activity. We have no way of knowing the true shape of this gas but we expect the tSZ signal to be greatest near the galaxy and decrease away from it, meaning it is simplest to assume a slightly extended Gaussian profile. We note that this Gaussian we use is slightly larger than the ACT 148 GHz beam, which has a FWHM of 1.44 arcmin.

We then scaled the filters so that the flux within a 1 arcmin radius aperture is preserved in our maps after filtering, representing the regions of interest we measure around the selected galaxies. This choice of aperture follows from Spacek et al. (2016), where it is noted that the energy input from AGN feedback is unlikely to affect scales much larger than twice the dark matter halo virial radius, which corresponds to about 2 arcmin at the redshifts we are investigating. Although the gas surrounding the galaxies will have both intrinsically different angular sizes and different angular sizes due to their differing redshifts, we have no way of knowing these sizes and the best we can do is take an aperture that is not unnecessarily large and that we expect to contain most of the signal in all cases. Additionally, we want these measurements to be comparable with cosmological AGN feedback simulations, and that is easiest to do with a constant measurement aperture. The factors used to scale the filters are 0.0167 and 0.0162 for 148 and 220 GHz, respectively. The final averaged, scaled filters are applied to the corresponding ACT maps for both seasons. Pictures of the

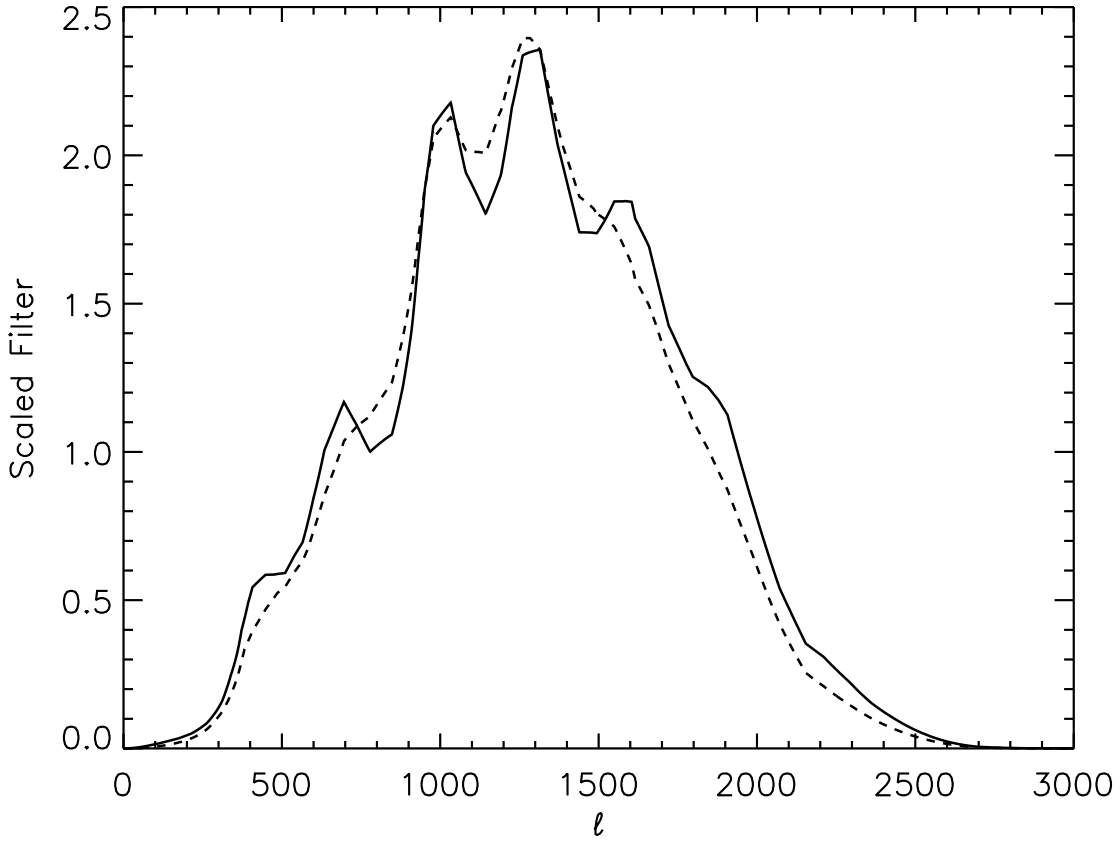

Figure 3.4: Scaled filters for both bands, averaged between seasons, in Fourier-space. The solid line represents 148 GHz and the dashed line represents 220 GHz.

final scaled Fourier-space filters are shown in Figure 3.4. The lack of smoothness is due primarily to the CMB power spectrum.

3.6 Stacking

To stack the CMB data we first made a 8.4×8.4 arcmin (17×17 pixel) stamp around each galaxy at 148 and 220 GHz in the filtered ACT data for seasons 3 and 4. Then we averaged the individual stamps together to make two stacked stamps for each band in each season, split into low-z and high-z galaxies. Finally, we averaged the seasons together. The resulting stamps are shown in Figure 3.5, with scales centered around 0 in units of μK. Any pixels > 4 arcmin away from the center were set to 0 since that was the distance of our potential contaminant cuts. We get our

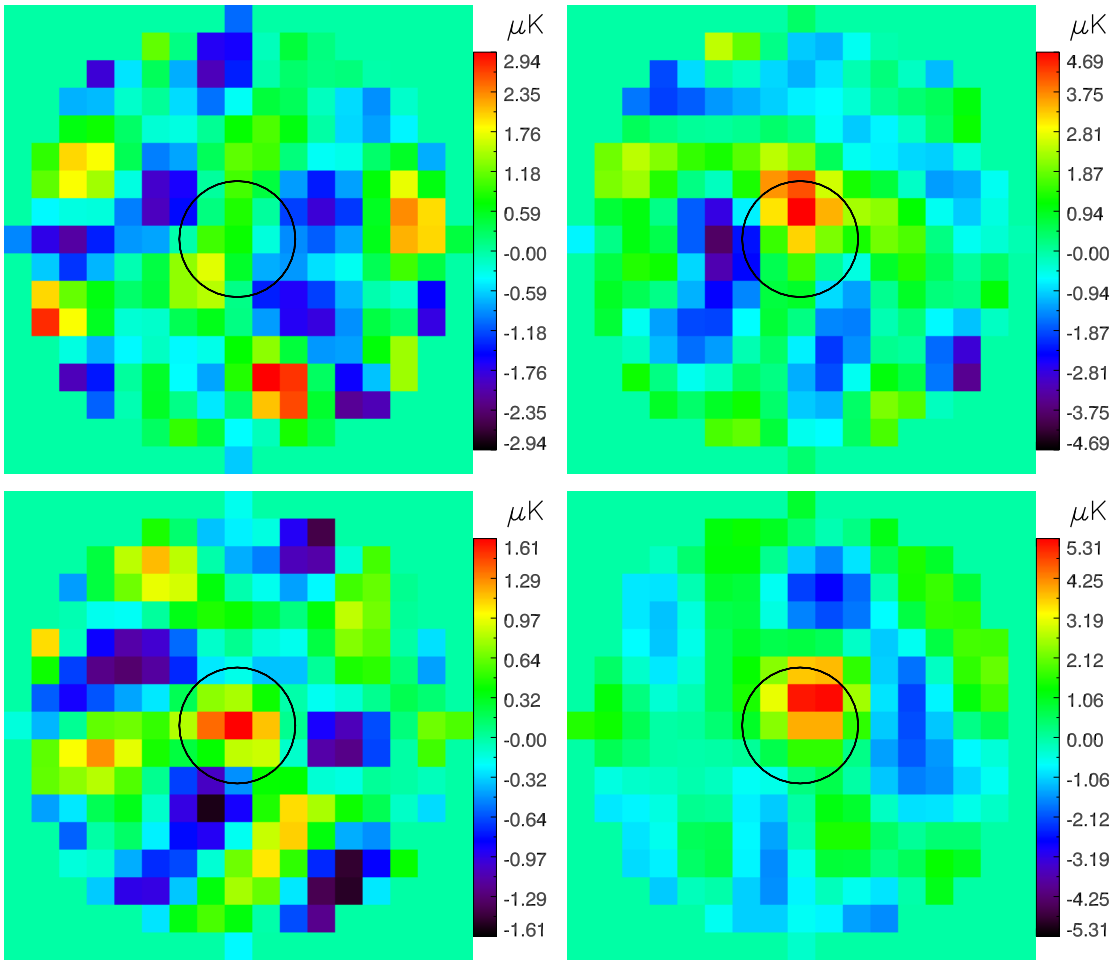

Figure 3.5: Season-averaged stacked galaxy stamps. Left is 148 GHz, right is 220 GHz, top is low-z (1179 galaxies), bottom is high-z (3274 galaxies). Units are μK, with black circles representing the 1 arcmin radius aperture we use for our final values.

final measurements integrated over the sky by summing the stacked signal within a 1 arcmin radius aperture (corresponding to a 2 pixel radius), shown as black circles in Figure 3.5.

The upper left panel of this figure shows a signal close to zero, while the lower left panel shows a clear positive signal in the center. These are the low-z and high-z 148 GHz stamps, respectively, and there is no tSZ detection in our initial stacks, which would be a negative signal at 148 GHz. In fact, at least at high-z, there is a significant contaminant signal. Looking at the right panels, at 220 GHz, we see

that the stamps are even more dominated by positive contaminant signals. Since the tSZ effect has a negligible impact at this frequency, indicated by Equation (3.7), this indicates that our galaxy selection process was imperfect, and there still remains a positive contaminating signal composed of faint sources that we were unable to account for. Looking at a typical range of emission by dust at $z = 1$ (light and dark blue curves in Figure 3.6), the CMB spectrum (green curve in Figure 3.6), and the ACT bands (rightmost red hatched region in Figure 3.6), it seems likely that this contaminating signal at 220 GHz also extends into the 148 GHz band. It is therefore likely that we are in fact seeing a significant tSZ signal that is obscured by contaminant emission.

In order to estimate the uncertainty in our final measurements we generated 429,571 random points in our field on the sky, a number chosen by dividing the area of our field by the area of the 148 GHz beam which we approximated as $2\pi\sigma^2$, where σ is the Gaussian beam standard deviation. We then applied the same 4 arcmin contaminant source cuts as we applied to our galaxy selection, leaving us with 294,176 random points. We stacked these random points on the sky for each band in the same way as we stacked our galaxies, and we computed the corresponding 1 arcmin radius aperture sums. First we computed an overall offset from the random points by getting the mean value of these sums. Since we remove galaxies anywhere near potential contaminants that might have positive or negative signal, we inherently bias the zeropoint of the ACT maps. We therefore corrected our aperture sums by subtracting off these mean offset values. These season-averaged offsets are 0.014 and -0.35 μK arcmin^2 for 148 and 220 GHz, respectively. Next we used the random point sums to compute the variance for an individual measurement in each case. If we first

define the normal variance of N random values x as

$$\text{var} = \frac{1}{N-1}\sum_{i=1}^{N}\left(x_i - \langle x \rangle\right)^2, \tag{3.12}$$

where $N = 294{,}176$, we can then define our overall uncertainty σ as a combination of measurement error and offset error, given by

$$\sigma = \left(\frac{\text{var}}{n} + \frac{\text{var}}{N}\right)^{1/2}, \tag{3.13}$$

where n is the number of galaxy measurements (1179 for low-z and 3274 for high-z). The result is final co-added sums and uncertainties for each individual season-averaged band and redshift bin, and these are given in Table 3.2.

From this table, we can directly see that there is a $\approx 1-2\sigma$ contaminant signal at 148 GHz, and a $\approx 3-6\sigma$ contaminant signal at 220 GHz. It is clear that obtaining the best possible constraints on non-gravitational heating and AGN feedback requires making the best possible separation between the tSZ signal and the contaminating signal, which is addressed in the following sections. Finally, we convert our co-added ΔT signal into gas thermal energy using Equation (3.8). These values are shown in Table 3.3, under "Data only."

3.7 Modeling and Removing Dusty Contamination

As evidenced by Table 3.2, there appears to still be a significant contamination signal indicated by the large positive 220 GHz values, which is likely contributing to the 148 GHz values that we are interested in for our tSZ measurements. This is illustrated by the blue lines in Figure 3.6, where it is clear that dust at reasonable temperatures around $z = 1$ will have significant emission in the ACT bands we are using. In order to constrain and subtract out this undetected contamination, we have followed the process described in Spacek et al. (2016) and built a detailed model of

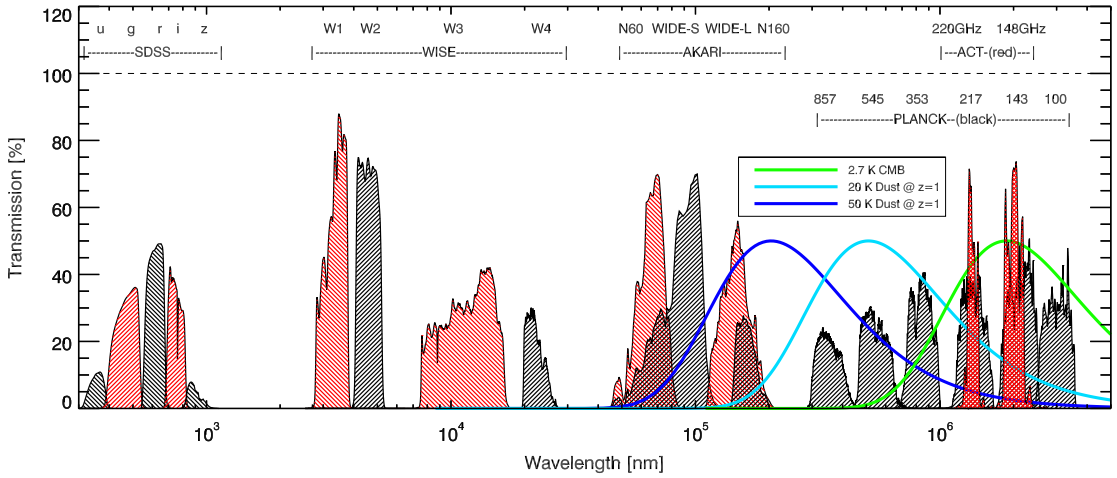

Figure 3.6: The filter curves for several of the data sets used in this paper. From left to right: SDSS and WISE bands used for galaxy selection, AKARI and Planck bands used for identifying and constraining the signal from dusty contaminating sources, and ACT bands used for measuring the tSZ effect. The first three surveys alternate between black and red for each band for clarity, while Planck bands are all black and ACT bands are all red to distinguish between the two. Also shown are blackbody curves for the CMB (green), 20 K dust at $z = 1$ (light blue), and 50 K dust at $z = 1$ (dark blue), all normalized to 50% on the plot. The horizontal dashed line indicates 100% transmission.

contaminants based on extrapolations of the source counts measured for SPT data in Mocanu et al. (2013). We extended these source counts to fainter values by modeling a random population of undetected sources that follow the trend of the detected sources into the unresolved region. We then related these models to the contaminating signal in our 148 and 220 GHz measurements.

To be clear about this process, the initial motivation is the observed contamination signal in the 148 and 220 GHz measurements. Since we have cut out galaxies near all possible known contaminating sources that we could find, we associate the contamination signal with undetected contaminants. We therefore want to find out what types of undetected contaminants produce signals across the 148 and 220 GHz bands that best fit our measurements. Since we do not know how the undetected contaminants behave across the 148 and 220 GHz bands, we cannot just do a simple

subtraction of the 220 GHz pure contamination signal from the 148 GHz contamination + tSZ signal. This leads to the main strategy used here: we vary the number of undetected contaminants, whether the contaminants have a dust spectrum or a synchrotron spectrum, the fraction of our measured galaxies that are affected by contamination, and the underlying 148 GHz tSZ signal. We do this using a range of values for each of these parameters that reflects the most likely value and its corresponding uncertainty. For every combination of these parameter ranges, we find out how well the observed signals are duplicated, and ultimately we hope to find out what combination of parameters best reflects the observed signals.

Following Mocanu et al. (2013) we then separated contaminants into synchrotron sources, which emit mostly at lower frequencies, and dusty sources, which emit mostly at higher frequencies. For each source population we modeled the number counts as a power law,

$$\frac{dN}{dS} = \frac{N_0}{S_{\rm max}} \left(\frac{S}{S_{\rm max}} \right)^{\alpha}, \tag{3.14}$$

where dN/dS is the number of sources between flux S and $S + dS$, N_0 is an overall amplitude, α is the power-law slope, and $S_{\rm max}$ is the flux at which we expect all brighter sources to have a 100% completeness level in the source count catalog. We then computed a range of allowed source count slopes from the Mocanu et al. (2013) data, by carrying out a χ^2 fit in log-space. Our best-fit slopes at 220 GHz were $\alpha_s = -2.08 \pm 0.09$ for the synchrotron sources and $\alpha_d = -2.91 \pm 0.17$ for the dusty sources.

Note that our calculated values for α_d are much steeper than α_s, meaning that while the number density of detected sources is dominated by synchrotron sources, the number density of undetected sources is likely to be dominated by dusty emitters. Note also that α_d and α_s are sufficiently steep that the number of sources diverges as S goes to 0, meaning that the source count distribution must fall off below some

Redshift z	Band (GHz)	1-arcmin-radius sum (μK arcmin^2)
0.5 - 1.0	148	1.0 ± 1.4
0.5 - 1.0	220	6.2 ± 2.3
1.0 - 1.5	148	2.1 ± 0.9
1.0 - 1.5	220	8.7 ± 1.4

Table 3.2: Final season-averaged co-added signals. The columns show redshift bin, band, and integration over a 1 arcmin radius region around the galaxies.

as-yet undetected flux. For simplicity, we modeled this fall-off as a minimum flux $S_{\rm min}$ below which there are no contaminating sources associated with the galaxies we are stacking.

For any choice of α_d, α_s, and $S_{\rm min}$ (which we will call a "source-count model"), we are then able to construct a model population of contaminating source fluxes through a four-step procedure as follows. (i) For each model source, we randomly decided whether it is a synchrotron source or a dusty source, such that the overall fraction of detectable dusty sources to synchrotron sources matches the observed source counts. We used a maximum flux cutoff of 305.7 μK arcmin^2, corresponding to the faintest bin of detected sources found by Mocanu et al. (2013). (ii) We then assigned the source a random 220 GHz flux, $S_{220,\rm rand}$, by inverting

$$\int_{S_{220,\rm min}}^{S_{220,\rm rand}} dS\,\frac{dN}{dS} = R\int_{S_{220,\rm min}}^{S_{220,\rm max}} dS\,\frac{dN}{dS}, \tag{3.15}$$

where $R \in [0,1]$ is a random number, such that their overall population matched the source count slopes. This gives

$$S_{220,\rm rand} = \left[(1-R)\,S_{220,\rm min}^{\alpha+1} + R\,S_{220,\rm max}^{\alpha+1}\right]^{\frac{1}{\alpha+1}}. \tag{3.16}$$

(iii) To obtain a corresponding flux for the source at 148 GHz we used the α_{220}^{150} spectral index distributions from Mocanu et al. (2013), which we assume to have normalized Gaussian shapes with the properties (center, σ) = (-0.55, 0.55) for synchrotron sources and (3.2, 0.89) for dusty sources. We then randomly chose α_{220}^{150} values that fit these distributions and calculated the 148 GHz flux (following Mocanu et al., 2013) as

$$S_{148,\mathrm{rand}} = \frac{S_{220,\mathrm{rand}}}{C_1 \times C_2}, \tag{3.17}$$

where C_1 is the conversion factor between Jy and μK arcmin^2 integrated over the band filter curves, C_2 is the relating factor $(\nu_{220}/\nu_{148})^{\alpha_{220}^{150}}$ integrated over the band filter curves, and we used units of μK arcmin^2 for all S. (iv) Finally, we estimated the completeness of our 220 GHz measurements and randomly discarded modeled sources to match the estimated fraction of 220 GHz sources detected per flux. To do the estimation, we assumed a cutoff S_{cut} of 250 μK arcmin^2, representing the 3σ limit of our 220 GHz source measurements. We discarded galaxies with signals greater than S_{cut} or signals less than $-S_{\mathrm{cut}}$. We then determined the completeness fractions for the modeled sources, and accounted for our measurement uncertainty, by adding the 220 GHz random point distribution onto S_{cut} in a cumulative manner using the fraction of random point measurements below a given flux. This means S_{cut} has a 50% completeness, while fainter fluxes are increasingly less complete and brighter fluxes are increasingly more complete.

For each source-count model, we repeated the process 100,000 times, resulting in a large catalog of contaminating fluxes in both bands. From these, we computed the mean flux per contaminating source in each band, $\langle S_{148,\mathrm{cont}} \rangle$ and $\langle S_{220,\mathrm{cont}} \rangle$, which represents the contamination we are measuring in our stacks. To account for variations in the input parameters, we computed model contamination signals for a wide range of source-count models, with $S_{220,\mathrm{max}} = 305.7\,\mu$K arcmin^2. We varied α_s from

Model	N	z	$\int \Delta T_{148}(\boldsymbol{\theta}) d\boldsymbol{\theta}$ (μK arcmin^2)	Y (10^{-7} Mpc^2)	$E_{\rm therm}(\pm 1\sigma)$ (10^{60} erg)	$E_{\rm therm}(\pm 2\sigma)$ (10^{60} erg)	S/N ($E_{\rm therm}/1\sigma$)
Data only	1179	$0.5-1.0$	1.0 ± 1.4	-0.8 ± 1.1	-2.8 ± 3.9	-2.8 ± 7.9	-0.72
	3274	$1.0-1.5$	2.1 ± 0.9	-1.9 ± 0.8	-7.0 ± 3.0	-7.0 ± 6.0	-2.33
χ^2 (ACT only)	1179	$0.5-1.0$	$-1.6^{+1.8}_{-1.9}$	$1.2^{+1.4}_{-1.4}$	$4.5^{+5.4}_{-5.1}$	$4.5^{+11.0}_{-10.7}$	0.85
	3274	$1.0-1.5$	$-2.1^{+1.1}_{-1.2}$	$1.9^{+1.1}_{-1.0}$	$7.0^{+4.0}_{-3.7}$	$7.0^{+8.4}_{-7.7}$	1.78
χ^2 (With Planck)	227	$0.5-1.0$	$-2.0^{+2.0}_{-2.1}$	$1.5^{+1.6}_{-1.5}$	$5.6^{+5.9}_{-5.6}$	$5.6^{+12.4}_{-11.6}$	0.97
	529	$1.0-1.5$	$-2.1^{+1.3}_{-1.4}$	$1.9^{+1.3}_{-1.2}$	$7.0^{+4.7}_{-4.4}$	$7.0^{+9.7}_{-9.4}$	1.50

Table 3.3: Our final tSZ measurements using various methods for removing contamination. The last three columns represent the best fit $E_{\rm therm}$ values with $\pm 1\sigma$ values and $\pm 2\sigma$ values and the $E_{\rm therm}$ signal-to-noise ratio ($E_{\rm therm}/1\sigma$), respectively.

-2.26 to -1.90 in steps of 0.09 and we varied α_d from -3.25 to -2.57 in steps of 0.17, representing ranges of $\pm 2\sigma$ in steps of σ. We let $\log_{10}(S_{\rm min})$ vary from $\log_{10}(0.01$ μK arcmin^2) to $\log_{10}(30$ μK arcmin^2) in steps of 0.2 in log-space.

For each source-count model, we computed best-fit tSZ values by varying our two free parameters, tSZ signal ($S_{\rm SZ}$) and the fraction of our measured sources that are contaminated ($f_{\rm cont}$). We varied the tSZ signal from -50 to 50 μK arcmin^2 in steps of 0.1 μK arcmin^2, and we varied the fraction contaminated from -3 to 9 in steps of 0.01. For every combination of these parameters we computed a χ^2 value,

$$\chi^2(f_{\rm cont}, S_{\rm SZ}) = \mathcal{B} \times \mathcal{A}^{-1} \times \mathcal{B}^T, \tag{3.18}$$

where $\mathcal{B}$ is the signal array,

$$\mathcal{B} = \begin{pmatrix} f_{\rm cont} \times \langle S_{148,{\rm cont}} \rangle + S_{\rm SZ} - S_{148} \\ f_{\rm cont} \times \langle S_{220,{\rm cont}} \rangle - S_{220} \end{pmatrix}, \tag{3.19}$$

and $\mathcal{A}$ is the noise matrix containing the noise for each band plus the covariance terms between each band,

$$\mathcal{A} = \begin{pmatrix} \sigma_{148}^2 & \sigma_{148}\sigma_{220} \\ \sigma_{148}\sigma_{220} & \sigma_{220}^2 \end{pmatrix}. \tag{3.20}$$

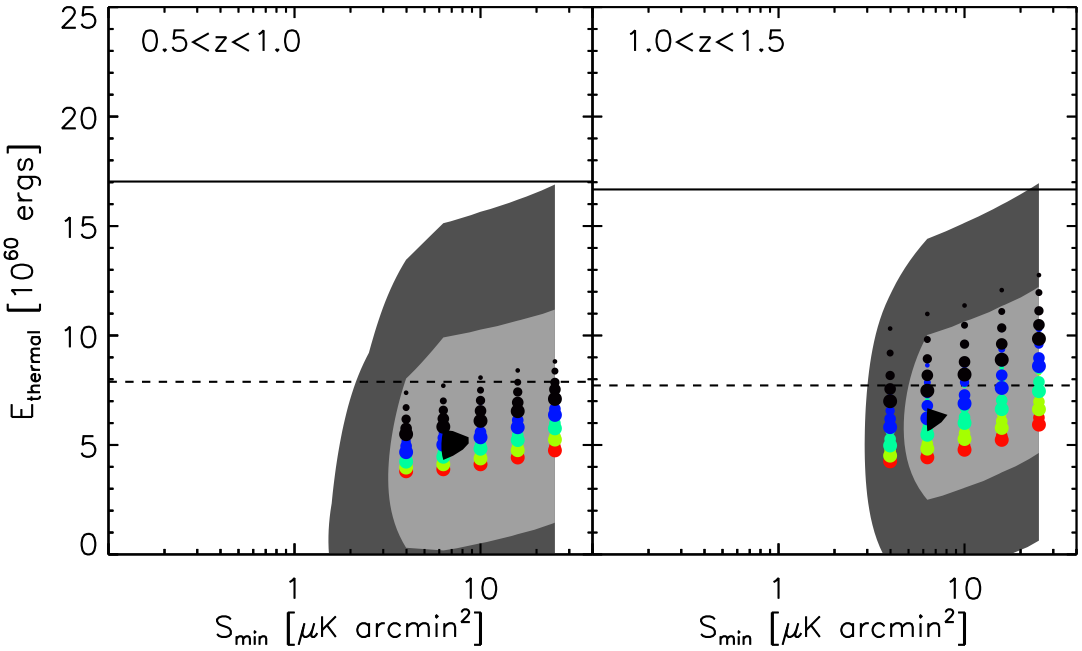

Figure 3.7: Plot of the contaminant-corrected $E_{\rm therm}$ (see Equation (3.8)) for different choices of $\alpha_{\rm dust}$, $\alpha_{\rm sync}$, and $S_{\rm min}$. Points are located at the peak χ^2 probability for each model. Increasing size represents increasing (i.e. more positive) α_s, and changing color from red to black represents increasing α_d. The light and dark gray regions represent the complete span of $\pm1\sigma$ and $\pm2\sigma$, respectively, for all points. Black regions represent the most favorable models with peak χ^2 probability. The horizontal solid black lines represent the best estimates for $E_{\rm grav}$, and the horizontal dashed black lines represent the -1σ values for $E_{\rm grav}$ (see Equation (3.5)).

Here, S_{148}, S_{220}, σ_{148}, and σ_{220} are our measured 1 arcmin radius values from Table 3.2. The σ values are computed using random point measurements, given by

$$\sigma_i\sigma_j = \frac{\sum_{a=0}^{N_{\rm rand}}(S^a_{i,\rm rand} - \langle S_{i,\rm rand}\rangle) \times (S^a_{j,\rm rand} - \langle S_{j,\rm rand}\rangle)}{N_{\rm rand}N_{\rm source}}, \tag{3.21}$$

where i and j represent the bands, $S_{a,\rm rand}$ and $S_{b,\rm rand}$ represent the 1 arcmin radius aperture values for the random points, $N_{\rm rand} = 294{,}176$ is the number of random points used, and $N_{\rm source}$ is the number of galaxies used (1179 for low-z and 3274 for high-z). We then converted the χ^2 values to Gaussian probabilities P by taking

$$P(S_{\rm SZ}) = \frac{\sum_{f_{\rm cont}\in[0,1]} \exp[-\chi^2(f_{\rm cont}, S_{\rm SZ})/2]}{\sum_{f_{\rm cont}}\sum_{S_{\rm SZ}} \exp[-\chi^2(f_{\rm cont}, S_{\rm SZ})/2]}. \tag{3.22}$$

where the lower sum over $f_{\rm cont}$ runs from -3 to 9 and the lower sum over $S_{\rm SZ}$ runs from -50 to 50 μK arcmin^2. Our approach was thus to marginalize over values of $f_{\rm cont}$ in the full physical range from 0 to 1, but normalize the overall probability by the sum of $f_{\rm cont}$ over a much larger range, including unphysical values. This excludes models in which a good fit to the data can only be achieved by moving $f_{\rm cont}$ outside the range of physically possible values.

Equation (3.22) then gives us a function $P(S_{\rm SZ})$ for each combination of α_d, α_s, and $S_{\rm min}$. We can convert the corresponding $S_{\rm SZ}$ value to the gas thermal energy, $E_{\rm therm}$, using Equation (3.8) and the average $l^2_{\rm ang}$ from Table 3.1. Note that a positive detection of the tSZ effect is seen as a negative ΔT signal at 148 GHz, and it represents a positive injection of thermal energy into the gas around the galaxy. Additionally, we compute a corresponding range for $E_{\rm grav}$ using Equation (3.5) and values from Table 3.1. The peak of each $P(S_{\rm SZ})$ curve is shown as the colored points in Figure 3.7, where α_s (represented by point size) is increasing (i.e. becoming more positive) downwards, and α_d (represented by point color) is increasing upwards. The 1σ and 2σ contours are computed for each $S_{\rm min}$ by averaging $P(S_{\rm SZ})$ across α_d and α_s. The resulting probability distribution depends only on $E_{\rm therm}$ and $S_{\rm min}$, and 1σ and 2σ are represented by the values $P(S_{\rm SZ}) = 0.61$ and 0.13, respectively (i.e. $\exp[-\sigma^2/2]$). These contours are shown in Figure 3.7, along with the -1σ range for $E_{\rm grav}$. Peak probability values are chosen using $P(S_{\rm SZ}) > 0.99$, shown as the black regions in Figure 3.7. From this figure we see that there is a $\approx 1\sigma$ tSZ detection for $S_{\rm min} \gtrsim 3\mu$K arcmin^2 at low-z. At high-z we see a $\approx 2\sigma$ tSZ detection for $S_{\rm min} \gtrsim 5\mu$K arcmin^2.

Finally, we average the probability distribution across $S_{\rm min}$ to get a final distribution as a function of only $E_{\rm therm}$. The significance values of this curve are shown in Table 3.3 under "ACT only." We see a 0.9σ tSZ detection at low-z and a 1.8σ detection at high-z.

3.8 Modeling and Removing Dusty Contamination With Planck

As indicated by Figure 3.6, we should be able to better constrain the contamination due to undetected dusty sources by incorporating data at higher frequencies than the ACT bands we are using to make our measurements. We therefore made use of the 2015 public data release from the Planck mission, and focused on the high-frequency bands at 217, 353, 545, and 857 GHz. These data, with a ≈5 arcmin FWHM beam (Planck Collaboration et al., 2015a), is too low-resolution to be useful in our direct tSZ measurements, but can still provide useful information about our galaxies at higher frequencies where the contaminant emission should be much brighter (see the light blue and dark blue curves in Figure 3.6). By incorporating these Planck measurements we should be able to better discriminate between contaminant models, allowing us to better identify the true tSZ signal.

To utilize the Planck data, we followed the same process as in the previous section by computing χ^2 values for a number of modeled contaminants, but now we had several extra terms in each computed χ^2 relating to the Planck measurements. In addition to the parameters used in the previous section, we also varied our models over reasonable values for contaminating dust temperature and residual CMB primary signal. Since there were now several more terms to fit, we could weight our final probabilities by the best fitting χ^2 values for each model. In order to stack our galaxies in the Planck data, we first extended our contaminant source cut distance from 4 to 10 arcmin due to the much lower resolution. This resulted in a significant decrease in our number of galaxies, with 227 at low-z and 529 at high-z. In order to filter out the primary CMB signal, we convolved each Planck map with a 7 arcmin FWHM Gaussian and subtracted the resulting image from the original. We then stacked the central pixels of each galaxy to get co-added values in each of the Planck

bands. In addition, we degraded the ACT 148 and 220 GHz maps to match the Planck beam, applied the same 7 arcmin FWHM filtering, and stacked the central pixels of galaxies in those images as well.

As was the case in Section 3.6, in all of these stacks there is an offset we needed to correct for since we are purposely avoiding positive contaminations in the maps. To do this we also made measurements at 54,962 random points on the sky that were restricted to the same contaminating-source cuts as our galaxies. These measurements allowed us to compute offset values needed to shift each band to a mean of 0, which we applied to our final measurements.

Finally, we computed our measurement errors by using the random point measurements (since the proper noise covariance matrix is not provided, i.e. Planck Collaboration et al., 2015b), corrected in two ways. First, because we account for the residual CMB primary signal in the χ^2 calculations, discussed below, we removed the corresponding uncertainty term, taken to have a covariance of 7.85 μK as used in Spacek et al. (2016). Second, there is an error introduced due to our offset corrections because they are made from a large, but finite, number of points. We then get the corrected error from

$$(\sigma_i\sigma_j)_{\rm corr} = \sqrt{\frac{\sigma_i\sigma_j - \sigma^2_{\rm cov}}{N_{\rm source}} + \frac{\sigma_i\sigma_j}{N_{\rm random}}}, \tag{3.23}$$

where $\sigma_i\sigma_j$ is given by Equation (3.21) with i and j representing the various bands used, $\sigma_{\rm cov} = 7.85\,\mu$K is the minimum CMB covariance discussed above, $N_{\rm source}$ is the number of sources used for the measurements (227 for low-z and 529 for high-z), and $N_{\rm random} = 54{,}962$ is the number of random points used. This represents both the error due to detector noise in each band as well as the error due to contributions from foregrounds on the sky. The majority of the variance at the highest frequencies is correlated between the bands and likely due to contributions from Galactic

dust emission. However, unlike the primary CMB signal, the spectral shape of this foreground is similar to that of the dusty sources we are trying to constrain, and it cannot be removed by fitting it separately.

In the same manner as the previous section, we modeled ACT 148 and 220 GHz contaminant source fluxes using a range of different source-count models (i.e. α_d, α_s, and $S_{\rm min}$), resulting again in 100,000 modeled contaminating source fluxes in each ACT band, $S_{148,\rm cont}$ and $S_{220,\rm cont}$. We also modeled what the contaminating signal would be in the Planck bands and the ACT bands filtered to match Planck. For each modeled contaminating source, if it was chosen to be a synchrotron source we simply extrapolated the Planck-based fluxes as

$$S_{\nu,\rm sync} = S_{148,\rm cont} \times \left(\frac{\nu}{\nu_{148}}\right)^{\alpha_{220}^{150}} \times C_\nu \times F, \tag{3.24}$$

integrated over the relevant band filter curves, where α_{220}^{150} is the same used in the previous section, C_ν is a frequency-dependent factor involved in the conversion from Jy to μK arcmin^2, and $F = 0.021$ is the factor required to preserve the signal within a 1 arcmin radius aperture after applying the Planck filtering we used.

In order to accurately describe thermal dust emission across the Planck frequencies, we adopted a modified blackbody with a free emissivity index, β, and dust temperature, $T_{\rm dust}$, often referred to as a gray-body (Planck Collaboration et al., 2015c). This requires us to add another free parameter, the temperature of the contaminant dust, $T_{\rm dust}$. This slope of each dusty source as a function of frequency is then

$$\left.\frac{d\ln S_\nu}{d\ln\nu}\right|_{\nu=185\,\rm GHz} = 3 + \beta - x_{185}[1-\exp(-x_{185})]^{-1}, \tag{3.25}$$

where $x_{185} \equiv (185\text{ GHz})\times h/(kT) = (185/416)(1+z)/T_{20}$ and T_{20} is the dust temperature in units of 20 K, and we use the slope of the blackbody function at $\nu = 185$ GHz because it is halfway between our two ACT bands (148 and 220 GHz). This can

be related, in turn, to the power law index α_{220}^{150} as

$$\beta + 3 = \alpha_{220}^{150} + x_{185}[1 - \exp(-x_{185})]^{-1}. \tag{3.26}$$

This then gives

$$\begin{aligned} S_{\nu,\mathrm{dust}} = \; & S_{148,\mathrm{cont}} \times \left(\frac{\nu}{\nu_{148}}\right)^{\alpha_{220}^{150} + x_{185}[1-\exp(-x_{185})]^{-1}} \\ & \times \frac{\exp[(\nu_{148}/416)(1+z)/T_{20}] - 1}{\exp[(\nu/416)(1+z)/T_{20}] - 1} \times C_\nu \times F, \end{aligned} \tag{3.27}$$

integrated over the relevant band filter curves, where we vary T_{dust} from 20 to 50 K in steps of 3 K.

With these expressions, we were able to compute χ^2 values for each source-count model accounting for the Planck measurements. This time, in addition to varying f_{cont} and S_{SZ}, we also varied $\mathrm{T_{dust}}$ (as discussed above) and a parameter Δ, which represents the offset due to the CMB primary signal, which we vary from -3 to 3 μK in steps of 0.1 μK. Computing χ^2 now involved the original ACT terms plus the new Planck terms, and it followed the same process as in Equation (3.18),

$$\chi^2(f_{\mathrm{cont}}, S_{\mathrm{SZ}}, T_{\mathrm{dust}}, \Delta) = \mathcal{B} \times \mathcal{A}^{-1} \times \mathcal{B}^T, \tag{3.28}$$

where $\mathcal{B}$ is the signal array and $\mathcal{A}$ is the noise matrix containing the noise for each band plus the covariance terms between each band. We denote each element of the signal array $\mathcal{B}_i$, where i runs over the two ACT bands (i.e. 148 and 220 GHz) and then every Planck-filtered band (i.e. the Planck bands at 857, 545, 353, and 217 GHz, plus the ACT bands at 220 and 148 GHz filtered to match the Planck images), such that $\mathcal{B}_1 = f_{\mathrm{cont}} \times \langle S_{148,\mathrm{cont}} \rangle + S_{\mathrm{SZ}} - S_{148}$, $\mathcal{B}_2 = f_{\mathrm{cont}} \times \langle S_{220,\mathrm{cont}} \rangle - S_{220}$, and $\mathcal{B}_{3-8} = f_{\mathrm{cont}} \times \langle S_{3-8,\mathrm{cont}} \rangle + \Delta - S_{3-8}$. As before, S_i represents the final values of our galaxy stacks for each band. We similarly define the elements of the noise matrix as $\mathcal{A}_{ij} = \sigma_i \sigma_j$, where i and j run over all of the bands and $\sigma_i \sigma_j$ is given by Equation (3.23).

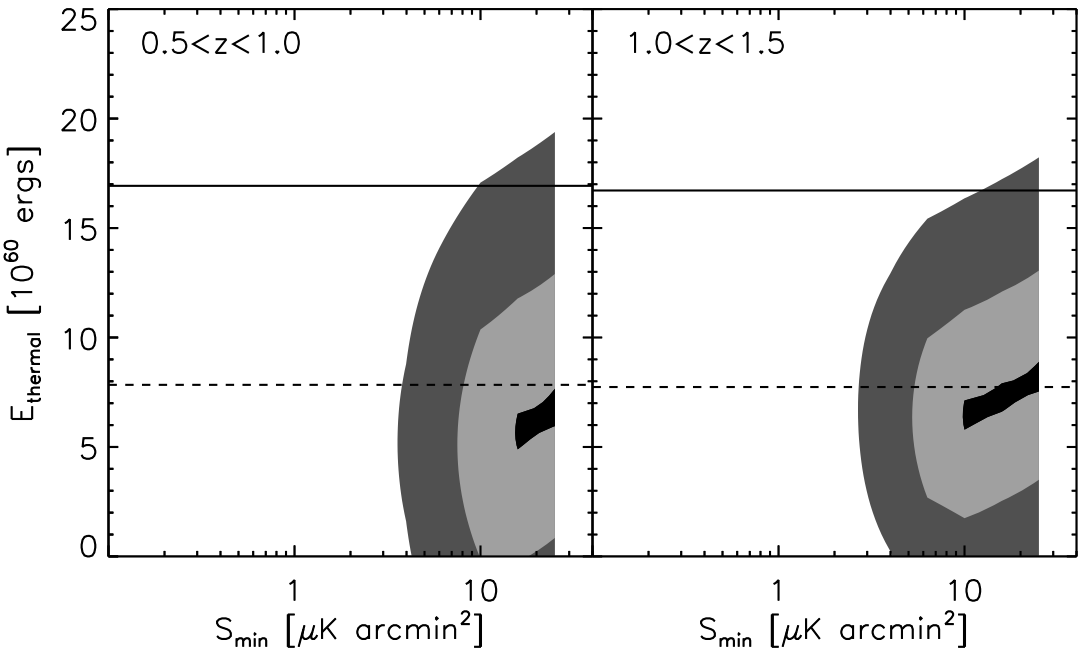

Figure 3.8: Plot of the contaminant-corrected $E_{\rm therm}$ (see Equation (3.8)) for different choices of $\alpha_{\rm dust}$, $\alpha_{\rm sync}$, and $S_{\rm min}$, incorporating the Planck bands. The light and dark gray regions represent the complete span of $\pm 1\sigma$ and $\pm 2\sigma$, respectively, for all points, and the black regions represent the peak of the χ^2 probability distribution, i.e. the most favorable models. The horizontal solid black lines represent the best estimates for $E_{\rm grav}$, and the horizontal dashed black lines represent the -1σ values for $E_{\rm grav}$ (see Equation (3.5)).

As in the previous section, we then converted the χ^2 values to Gaussian probabilities by taking

$$P(S_{\rm SZ}) = \sum_{f_{\rm cont}\in[0,1],T_{\rm dust},\Delta} \frac{\exp[-\chi^2(f_{\rm cont}, S_{\rm SZ}, T_{\rm dust}, \Delta)/2]}{\sum_{\rm all}\exp[-\chi^2/2]}, \tag{3.29}$$

where the whole function is normalized to a total of 1, and each final SZ value contains the sum over the corresponding $T_{\rm dust}$, Δ, and fractions from 0 to 1. Since in this case there are eight terms contributing to χ^2 and four fit parameters, this leaves us with four degrees of freedom. Thus the minimum χ^2 was not 0 in every case as it was above with just 2 measurements and 2 fit parameters, and so for each model we scale the final probabilities by $\exp(-\chi^2_{\rm min}/2)$, where $\chi^2_{\rm min}$ is the minimum χ^2 value for that model.

Study	N	Type	z (mean)	Mass ($M_\odot$)	tSZ $Y(10^{-7}$ Mpc$^2)$
Spacek et al. (2016)	3394	SPT	$0.5-1.0$ (0.72)	1.51×10^{11}	$2.3^{+0.9}_{-0.7}$
Spacek et al. (2016)	924	SPT	$1.0-1.5$ (1.17)	1.78×10^{11}	$1.9^{+2.4}_{-2.0}$
Spacek et al. (2016)	937	SPT+Planck	$0.5-1.0$ (0.72)	1.51×10^{11}	$2.2^{+0.9}_{-0.7}$
Spacek et al. (2016)	240	SPT+Planck	$1.0-1.5$ (1.17)	1.78×10^{11}	$1.7^{+2.2}_{-1.8}$
Current	1179	ACT	$0.5-1.0$ (0.83)	7.81×10^{11}	$1.2^{+1.4}_{-1.4}$
Current	3274	ACT	$1.0-1.5$ (1.20)	10.1×10^{11}	$1.9^{+1.1}_{-1.0}$
Current	227	ACT+Planck	$0.5-1.0$ (0.83)	6.93×10^{11}	$1.5^{+1.6}_{-1.5}$
Current	529	ACT+Planck	$1.0-1.5$ (1.21)	9.68×10^{11}	$1.9^{+1.3}_{-1.2}$

Table 3.4: A comparison between Spacek et al. (2016) and the current work. Y is the angularly integrated Compton-y parameter given by Equation (3.30). Mass refers to stellar mass.

This again gave us a function $P(S_{\rm SZ})$ for each combination of α_d, α_s, and $S_{\rm min}$, which we can convert to an energy $E_{\rm therm}$. The 1σ and 2σ contours are created for each $S_{\rm min}$ by averaging $P(S_{\rm SZ})$ across α_d and α_s and then dividing the final result by the single maximum value. 1σ and 2σ are again represented by the values 0.61 and 0.13, respectively, with peak probability values represented by $P(S_{\rm SZ}) > 0.99$. These contours are shown in Figure 3.8, along with the -1σ range for $E_{\rm grav}$. From this figure we can see that, for low-z, including Planck has slightly increased the estimated tSZ effect, though it now favors higher $S_{\rm min}$ values. The high-z result has not changed much besides an increased uncertainty due to fewer galaxies. For both redshift bins, the σ values have increased due to the large decrease in the number of stacked galaxies because of Planck's much larger beam.

Finally, we average the probability distribution across $S_{\rm min}$, divided by the maximum value again, and get a final distribution as a function of only $E_{\rm therm}$. The significance (σ) values of this curve are shown in the "With Planck" part of Table 3.3. At low-z, the significance of our tSZ detection has increased from 0.9σ to

1.0σ, while at high-z the tSZ detection significance decreases from 1.8σ to 1.6σ. It is clear that the gain in sensitivity with Planck has been limited by the decrease in the number of galaxies in each redshift bin due to the much larger beam size of Planck compared to the ACT. To clearly show this, we followed the methods of Section 3.7 (i.e. only ACT data were used), using this limited galaxy sample. The result is a 0.1σ tSZ detection at low-z and a 0.5σ tSZ detection at high-z. It is apparent, then, that adding the Planck data helps immensely with constraining the tSZ signal when the same number of galaxies are used, but since we have to limit our galaxy sample size so much to avoid contaminants in the Planck beam, the loss of accuracy due to fewer measurements just about offsets the gain in accuracy given by the added Planck data.

Alternatively, we can also characterize the total tSZ signal for our co-adds with the angularly integrated Compton-y parameter, Y. While we cannot directly compare peak Compton-y values with past measurements, as these are beam-dependent quantities, we can compare the angularly integrated Y values between our results and past experiments. Using Equation (3.7) at 148 GHz, this is

$$\begin{aligned} Y &\equiv l_{\rm ang}^2 \int y(\boldsymbol{\theta}) d\boldsymbol{\theta} \\ &= -3.2 \times 10^{-8}\,{\rm Mpc}^2 \left(\frac{l_{\rm ang}}{\rm Gpc}\right)^2 \frac{\int \Delta T_{148}(\boldsymbol{\theta}) d\boldsymbol{\theta}}{\mu{\rm K\ arcmin}^2}, \end{aligned} \tag{3.30}$$

such that $Y = 2.7 \times 10^{-8}\,{\rm Mpc}^2 E_{60}$, where E_{60} is $E_{\rm therm}$ in units of 10^{60} erg. We can use this to compare the results in this paper with the similar work in Spacek et al. (2016), with a detailed comparison shown in Table 3.4. Comparing the two results, we see a decrease in Y at low-z in this work compared to Spacek et al. (2016), and similar Y values at high-z, but we also see a significant increase in the average galaxy mass. This is contrary to the expected trend of higher Y with higher mass seen in

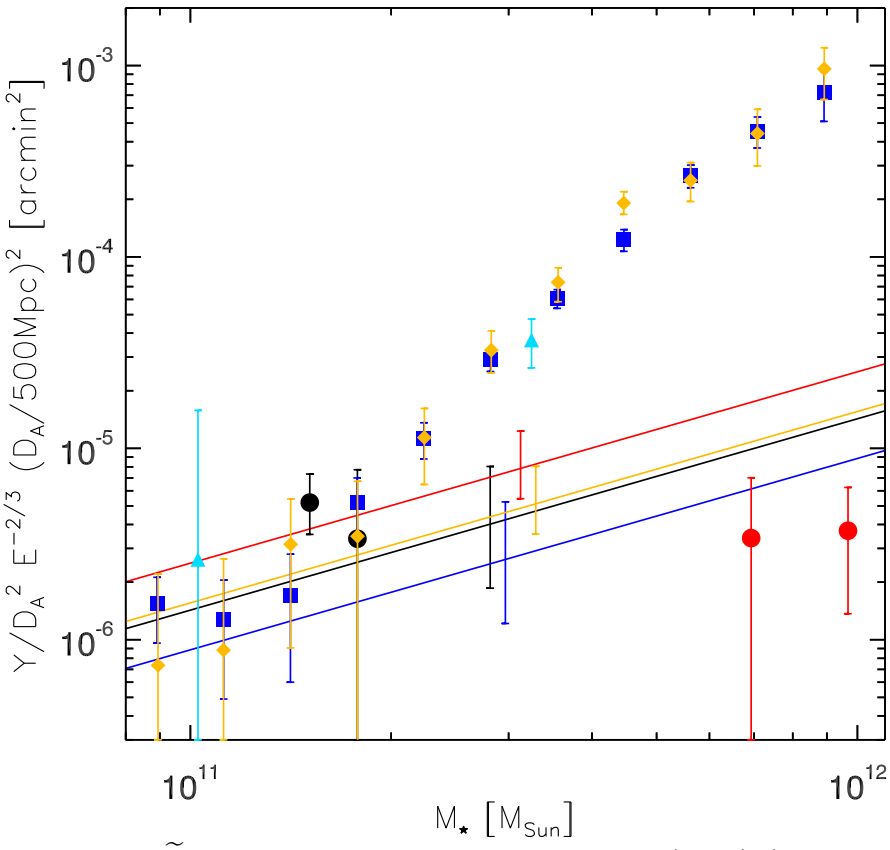

Figure 3.9: Plot of $\widetilde{Y}$ vs. stellar mass for Spacek et al. (2016) (black circles), the current work (red circles), Planck Collaboration et al. (2013) (blue squares), Greco et al. (2015) (orange diamonds), and Ruan et al. (2015) (light blue triangles). Using Equations (3.5), (3.6), and (3.30), we can use our simple models to make estimates of $\widetilde{Y}$ vs. stellar mass. These model estimates are shown for gravitational heating only (black line for $z = 0.8$, blue line for $z = 1.2$) and gravitational plus AGN feedback heating (red line for $z = 0.8$, orange line for $z = 1.2$), with $\pm 1\sigma$ errorbars.

previous work (e.g. Planck Collaboration et al., 2013; Greco et al., 2015; Ruan et al., 2015).

We can compare with this previous work by defining $\widetilde{Y} \equiv \frac{Y}{l_{\mathrm{ang}}^2} \times E^{-2/3} \times \left(\frac{l_{\mathrm{ang}}}{500\ \mathrm{Mpc}}\right)^2$, where $E(z)$ is the Hubble parameter, and this is shown in Figure 3.9. The circles represent Spacek et al. (2016) (black) and this work (red), both using measurements of massive quiescent elliptical galaxies with average redshifts greater than 0.7 for the lower-mass values of either color and 1.1 for the higher-mass values of either color. The blue squares represent Planck Collaboration et al. (2013) measurements

of locally brightest galaxies, with redshifts less than ≈0.3. The orange diamonds represent Greco et al. (2015) measurements of locally brightest galaxies, with redshifts less than ≈0.3. The light blue triangles represent Ruan et al. (2015) measurements of locally brightest galaxies, with median redshifts of ≈0.5 and redshifts less than ≈0.8. Looking at this figure, we see that the results of Spacek et al. (2016) are roughly consistent with the previous tSZ measurements, while the results of this work are over ≈2 orders of magnitude smaller than previous tSZ measurements at the same mass. We note that the measurements of locally brightest galaxies from Planck Collaboration et al. (2013), Ruan et al. (2015), and Greco et al. (2015) are of significantly lower redshifts than our galaxies, with the highest overall redshift being no more than ≈0.8 from Ruan et al. (2015) while our average redshifts range from 0.7 to 1.2. In addition, our selection criteria involve choosing quiescent elliptical galaxies and removing any galaxies in or around all detectable clusters, while the low-redshift locally brightest galaxies of the previous studies are more likely to be found in the centers of massive galaxy groups and clusters. Redshift alone cannot account for the ≈2 orders of magnitude difference in measurements, as is made clear by the black and red lines representing our models at $z = 0.8$ (without and with AGN feedback, respectively) and the blue and orange lines representing our models at $z = 1.2$ (without and with AGN feedback, respectively). However, the differences in redshift combined with the different galaxy selection methods suggest that the galaxies used in this paper could be from fundamentally different populations and environments.

With Equations (3.5) and (3.6) and the redshifts and masses from Table 3.1, we can also investigate theoretical thermal energies of the gas around elliptical galaxies due to both gravity and AGN feedback. Without Planck, we estimate the gravitational heating energy to be $E_{\rm therm,grav} = 17.0^{+17.0}_{-9.1} \times 10^{60}$ erg for our low-z sample

and $E_{\rm therm,grav} = 16.7^{+16.7}_{-9.0} \times 10^{60}$ erg for our high-z sample. We therefore measure excess non-gravitational energies of $E_{\rm therm,feed,dat} = -12.5^{+17.7}_{-10.6} \times 10^{60}$ erg for low-z and $E_{\rm therm,feed,dat} = -9.7^{+17.1}_{-9.8} \times 10^{60}$ erg for high-z, both of these values consistent with zero detection. For completeness, we can plug these into the theoretical AGN feedback energy equation and solving for ϵ_k, we get feedback efficiencies of $-4.8^{+6.8}_{-4.1}\%$ for low-z and $-3.8^{+6.7}_{-3.9}\%$ for high-z.

With Planck, we estimate the gravitational heating energy to be $E_{\rm therm,grav} = 15.1^{+15.1}_{-8.1} \times 10^{60}$ erg for our low-z sample and $E_{\rm therm,grav} = 15.9^{+15.9}_{-8.5} \times 10^{60}$ erg for our high-z sample. We therefore measure excess non-gravitational energies of $E_{\rm therm,feed,dat} = -9.5^{+16.1}_{-10.0} \times 10^{60}$ erg for low-z, and $E_{\rm therm,feed,dat} = -8.9^{+16.5}_{-9.7} \times 10^{60}$ erg for high-z, both consistent with 0. Plugging these into the theoretical AGN feedback energy equation and solving for ϵ_k, we get feedback efficiencies of $-4.1^{+7.0}_{-4.4}\%$ for low-z and $-3.7^{+6.8}_{-4.0}\%$ for high-z. These values are very uncertain and consistent with a detected AGN feedback signal of 0. They also do not rule out the suggested and measured $\approx$5% (e.g. Scannapieco et al., 2005; Ruan et al., 2015; Spacek et al., 2016). We also note that the feedback efficiencies stated in Spacek et al. (2016) are mistakenly off by a factor of 5, and they should be $7.3^{+6.6}_{-7.8}\%$ for low-z and $6.6^{+17.3}_{-15.3}\%$ for high-z.

3.9 Discussion

In this paper we have performed a stacking analysis of the tSZ signal around 4453 massive elliptical galaxies that are promising candidates for containing relic heating due to past episodes of AGN feedback. We split our selected galaxies into two redshifts bins, with 1179 galaxies in our "low-z" bin ($0.5 \leq z \leq 1.0$) and 3274 galaxies in our "high-z" bin ($1.0 \leq z \leq 1.5$). Our initial stacks were dominated by considerable contaminating emission which was much stronger at 220 GHz than at 148 GHz. Since dusty contaminant emission emits at both 148 and 220 GHz,

as suggested by Figure 3.6, the large signals at 220 GHz, where the tSZ effect is expected to be negligible, indicate a corresponding large contaminant signal at 148 GHz, where the tSZ effect causes a decrement. We therefore performed an analysis of the contaminating signal by modeling potential undetected sources and running a χ^2 probability test on the models. This revealed the underlying tSZ signal, with a 0.9σ significance at low-z and a 1.8σ significance at high-z. Finally, in order to better constrain the stacked contaminating signal, we incorporated high-frequency Planck measurements of a subset of 227 low-z galaxies and 529 high-z galaxies. These results indicated tSZ detections with a 1.0σ significance at low-z and a 1.6σ significance at high-z. The values for each of these analyses are given in Table 3.3.

The work done here is complementary to the work done in Spacek et al. (2016), which stacked 4318 galaxies in a southern patch of sky using SPT data, while we stacked 4453 galaxies in the Stripe-82 equatorial band using ACT data. Both analyses used similar galaxy selection criteria, though that of Spacek et al. (2016) favored lower-mass, $0.5 \leq z \leq 1.0$ "low-z" galaxies while our selection favored $1.0 \leq z \leq 1.5$ "high-z" galaxies with higher stellar masses. Their most significant low-z and high-z tSZ detections were at 3.6σ and 0.9σ levels, respectively, while ours were at 1.0σ and 1.8σ, respectively. A detailed comparison between the two studies can be seen in Table 3.4, where we see similar tSZ Y measurements in this work, although we use galaxies with higher masses. A plot comparing these results, as well as results from other previous galaxy tSZ measurements from Planck Collaboration et al. (2013), Greco et al. (2015), and Ruan et al. (2015), is shown in Figure 3.9. These last three results appear to be significantly higher than the results of this paper. This may be due to several factors, including inherent differences in the measurements due to different galaxy populations. The previous studies focus on lower-redshift locally brightest galaxies, while this work looks at quiescent elliptical galaxies at significantly

higher redshifts. We also perform extensive cuts to avoid clusters and dusty galaxies. There is the additional possibility that we are not completely accounting for and removing the contamination signal in this work despite our best efforts, though this seems unlikely to be the main reason for the discrepancy. Also shown in Figure 3.9 are lines representing our simple gravitational and AGN feedback heating models given by Equations (3.5) and (3.6). These simple models indicate that the types of galaxies and redshifts that we are looking at are expected to produce significantly lower tSZ measurements. The measurements presented here are also unique, with a review of the literature revealing no other similar measurements of the tSZ signal around such massive, high-redshift, quiescent elliptical galaxies. It therefore may not be completely appropriate to make direct comparisons between these measurements and measurements of less massive, lower-redshift locally brightest galaxies. While Spacek et al. (2016) estimate AGN feedback efficiencies of around $\approx$7%, close to the suggested 5% (e.g. Scannapieco et al., 2005; Ruan et al., 2015), this work sees an AGN feedback heating signal consistent with 0, with efficiencies of $-4.1^{+7.0}_{-4.4}$% for low-z and $-3.7^{+6.8}_{-4.0}$% for high-z. It is important to note, however, that we use simple, general models of gravitation and AGN feedback in this paper to estimate the corresponding energies, and that specific, detailed galaxy simulations are needed to draw more precise conclusions from these measurements.

tSZ measurements of galaxies and AGNs are likely to improve significantly in the near future. More data and an additional band at 277 GHz will be released from ACT observations (Dünner et al., 2013), while an upcoming full survey release of SPT data will include a 2500 deg^2 field using bands at 95, 150, and 220 GHz (Schaffer et al., 2011). These much larger fields with more bands will allow for a much larger set of galaxies to be co-added at more frequencies, vastly improving the signal-to-noise of the measurements and allowing for further constraints on contaminating signals. Separat-

ing out such contaminants will also become more effective with future surveys such as the upgraded ACT telescope (Advanced ACTPol) and the proposed Cerro Chajnantor Atacama Telescope (CCAT).[15] Another approach to constraining AGN feedback is through deep measurements of smaller samples of galaxies, identified as the most interesting, using large radio telescopes. The Goddard IRAM Superconducting Two Millimeter Camera (GISMO) and the New IRAM KIDs Array (NIKA) are powerful new instruments mounted on the Institute de Radioastronome Millimetrique (IRAM) 30 m telescope[16] that may prove useful for this purpose. Also promising is the National Radio Astronomy Observatories (NRAO) Green Bank Telescope (GBT), whose Continuum Backend operates at lower frequencies where the tSZ signal is roughly three times larger. Finally, although tSZ observations reveal the total thermal heating around galaxies, they must be complimented by theoretical models and simulations in order to best distinguish between heating due to gravitation, AGN feedback, and other effects. Observations can therefore be combined with tSZ simulations of the same types of objects with the same average parameters (e.g. mass, redshift, age) to produce weighted stacks that are adapted to be as sensitive as possible to the differences between AGN feedback models. The tSZ effect provides a promising tool for future measurements to improve our understanding of AGN feedback and galaxy evolution.

[15] http://www.ccatobservatory.org/

[16] http://www.iram-institute.org/EN/30-meter-telescope.php

Chapter 4

USING REAL AND SIMULATED MEASUREMENTS OF THE THERMAL SUNYAEV-ZEL'DOVICH EFFECT TO CHARACTERIZE AND CONSTRAIN MODELS OF AGN FEEDBACK

4.1 Introduction

Galaxies are some of the most common and prominent objects in the Universe. As important as they are, the processes governing their formation and evolution are surprisingly uncertain. Although simple early models favored hierarchical growth in which progressively larger galaxies are expected to form stars at later times (e.g. Rees & Ostriker, 1977; White & Frenk, 1991), an increasing amount of observational evidence reveals galaxy evolution to be more complex (e.g. Cowie et al., 1996). Since $z \approx 2$ the typical mass of star-forming galaxies has decreased by a factor of $\approx$10 or more (Drory & Alvarez, 2008). The same goes for active galactic nucleus (AGN) evolution, where the typical luminosity of AGNs is observed to have decreased by as much as a factor of $\approx$1000 since $z \approx 2$ (Hopkins et al., 2007). This observed downsizing trend of both galaxies and AGNs, combined with other well-known relationships between supermassive black holes and their host galaxies like the $M_{\rm BH}$–$\sigma_\star$ relation (e.g. Shankar et al., 2016), points to a mechanism affecting both the small scale of the supermassive black hole ($\lesssim$ 1 ly) and the large scale of the galaxy ($\gtrsim$ 100 kly).

One such mechanism that has been proposed to resolve many of the problems mentioned above is the AGN phase of the supermassive black hole (e.g. Sijacki et al., 2007). AGNs are energetic enough to drive out enormous, powerful radio jets, as well as extremely luminous radiative winds, causing energetic outflows through the host

galaxy. This feedback has the potential to blow out and heat up cool gas within and around the galaxy, preventing both further star formation in the galaxy and further accretion onto the supermassive black hole. Incorporating AGN feedback into numerical galaxy evolution models has been shown to be very effective in reproducing the observed downsizing (e.g. Scannapieco & Oh, 2004; Sijacki et al., 2007; Hirschmann et al., 2012; Lapi et al., 2014; Kaviraj et al., 2016). However, the specific details of AGN feedback remain uncertain because precise details are very difficult to measure (e.g. Fabian, 2012).

One of the most promising methods for directly measuring the impact of AGN feedback on galaxies and clusters is by looking at anisotropies in the cosmic microwave background (CMB) photons passing through hot, ionized gas, known as the Sunyaev-Zel'dovich (SZ) effect (Sunyaev & Zeldovich, 1972). If the gas is moving with a bulk velocity, there will be frequency-independent fluctuations in the CMB temperature known as the kinematic SZ (kSZ) effect, which can be used to detect the profile of ionized gas within dark matter halos, providing information on where hot gas is located around galaxies. This method is becoming increasingly promising, with some of the first detections of the kSZ effect in galaxy clusters made recently by stacking CMB observations with Planck (Planck Collaboration et al., 2016), the South Pole Telescope (SPT) (Soergel et al., 2016), and the Atacama Cosmology Telescope (ACT) (Schaan et al., 2016).

Additionally, if the gas is sufficiently heated, there will be redshift-independent fluctuations in the CMB temperature known as the thermal SZ (tSZ) effect, which can be integrated over a region of the sky to give a direct measurement of the gas thermal energy (e.g. Scannapieco et al., 2008). Measurements of the tSZ effect have been very useful in detecting massive galaxy clusters (e.g. Reichardt et al., 2013). Simulations

have also shown that the tSZ effect can be effective in distinguishing between models of AGN feedback (e.g. Chatterjee et al., 2008; Scannapieco et al., 2008).

Significant observational work has already been done to try and measure the tSZ effect. For example, Chatterjee et al. (2010) used data from WMAP and SDSS around both quasars and galaxies to find a tentative tSZ signal suggesting AGN feedback; Hand et al. (2011) used data from SDSS and ACT to find a significant tSZ signal around galaxies; Gralla et al. (2014) used ACT to find a significant tSZ signal around AGNs; Greco et al. (2015) used SDSS and Planck to find a significant tSZ signal round galaxies; Ruan et al. (2015) used SDSS and Planck to find significant tSZ signals around both quasars and galaxies; Crichton et al. (2016) used SDSS and ACT to find a significant tSZ signal around quasars; and Hojjati et al. (2016) used data from Planck and RCSLenS to find a tSZ signal suggestive of AGN feedback.

Additionally, recent measurements have been made around quiescent, moderate redshift elliptical galaxies (Spacek et al., 2016, 2017), where a signal due to AGN feedback is expected (e.g. Scannapieco et al., 2008). The signal is very faint, though, so measurements from a large number of galaxies must be stacked. Spacek et al. (2016) performed this type of stacking analysis using the VISTA Hemisphere Survey (VHS) and Blanco Cosmology Survey (BCS) along with the 2011 SPT data release, finding a signal hinting at non-gravitational heating based on simple energy models. Spacek et al. (2017) used the Sloan Digital Sky Survey (SDSS) and Wide-Field Infrared Survey Explorer (WISE) along with the 2008/2009 ACT data, finding a signal consistent with gravitational-only heating based on the same simple energy models. These SPT and ACT results are shown in Figure 4.1 (black and red circles, respectively), along with the simple model predictions and some previous studies. Note the large discrepancy between the higher-mass ACT results and previous measurements using Planck data, which is likely due to the differences in redshift, environment, and

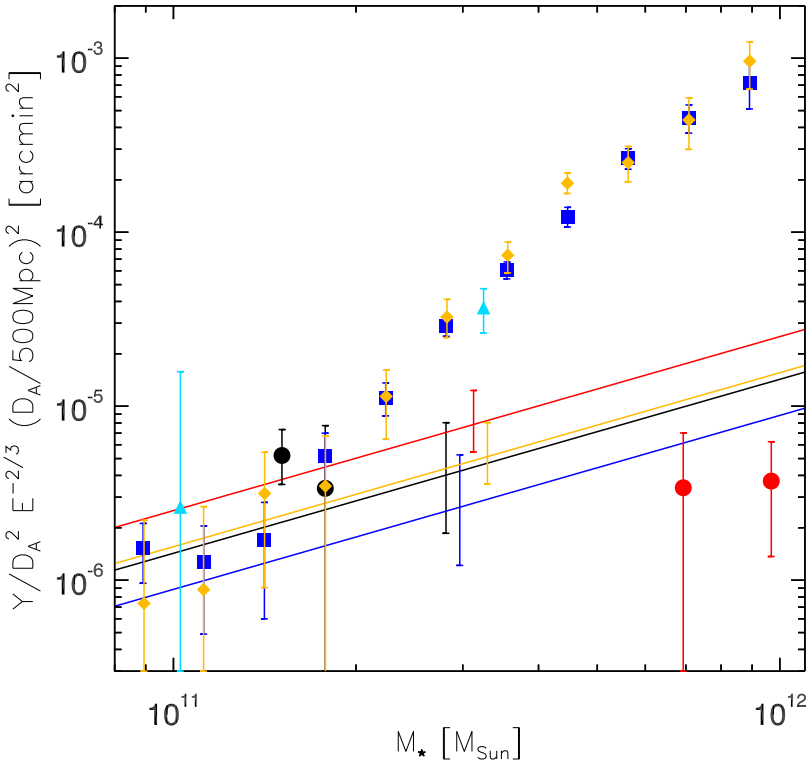

Figure 4.1: Plot of normalized angularly-integrated tSZ signal vs. stellar mass for Spacek et al. (2016) (black circles), Spacek et al. (2017) (red circles), Planck Collaboration et al. (2013) (blue squares), Greco et al. (2015) (orange diamonds), and Ruan et al. (2015) (light blue triangles). Solid lines are estimates using simple models from (Spacek et al., 2016), shown for gravitational heating only (black line for $z = 0.8$, blue line for $z = 1.2$) and gravitational plus AGN feedback heating (red line for $z = 0.8$, orange line for $z = 1.2$), with $\pm 1\sigma$ errorbars.

overall galaxy population being studied in these various papers. This highlights the need to look at a diverse range of galaxies in order to understand the complete picture of thermal heating.

Directly measuring the energy and distribution of hot gas around galaxies can only reveal so much about the specific physical mechanisms resulting in the observations. In order to place constraints on AGN feedback and other non-gravitational heating processes, it is necessary that observational work be complimented by accurate, detailed simulations. There is a rich history of complementing tSZ measurements and AGN feedback with simulations. For example, both Scannapieco et al. (2008)

and Chatterjee et al. (2008) used large-scale cosmological simulations to give details about the possibilities of measuring AGN feedback with the tSZ effect, Cen & Safarzadeh (2015b) used simulations to investigate the feedback energies from quasars and implications for tSZ measurements, Hojjati et al. (2015) used large-scale cosmological simulations to estimate AGN feedback effects on cross-correlation signals between gravitational lensing and tSZ measurements, and Dolag et al. (2016) used large-scale simulations to study the impact of structure formation and evolution with AGN feedback on tSZ measurements.

In this work, we utilize the large-scale cosmological simulations Horizon-AGN and Horizon-noAGN, which are simulations with and without AGN feedback, respectively (Dubois et al., 2012, 2014; Kaviraj et al., 2015, 2016), to compliment the work done in Spacek et al. (2016, 2017). We will investigate looking at a similar population of moderate redshift, quiescent elliptical galaxies and simulate their tSZ measurements. We will then use their measurement distribution and stacking statistics to give insight into the previous observational results. These Horizon simulations have a comoving volume of 100 Mpc/h, 1024^3 dark matter particles, and a minimum cell size of 1 physical kpc, which allow for a large enough population of the generally uncommon galaxies we are interested in.

The structure of this paper is as follows: in Section 4.2, we discuss the tSZ effect and various models of AGN feedback. In Section 4.3, we discuss the Horizon-AGN simulation. In Section 4.4, we discuss how we select and measure the tSZ effect around galaxies. In Section 4.5, we give the parameters and measurements of our selected galaxies. In Section 4.6, we discuss implications for our results in regard to Spacek et al. (2016, 2017) and tSZ measurements of AGN feedback in general.

Throughout this work, we use a Λ Cold Dark Matter cosmological model with parameters (from Planck Collaboration et al., 2015d), $h = 0.68$, $\Omega_0 = 0.31$, $\Omega_\Lambda =$

0.69, and $\Omega_b = 0.049$, where h is the Hubble constant in units of 100 km s^{-1} Mpc^{-1}, and Ω_0, Ω_Λ, and Ω_b are the total matter, vacuum, and baryonic densities, respectively, in units of the critical density.

4.2 The tSZ Effect

When CMB photons pass through hot, ionized gas along our line of sight, inverse Compton scattering between the photons and electrons causes the photons to gain energy. The resulting shift in the CMB spectrum has a distinctive frequency dependence, with a weaker signal below, and a stronger signal above, 217.6 GHz. The nonrelativistic change in the CMB temperature ΔT as a function of frequency ν due to the tSZ effect is

$$\frac{\Delta T}{T_{\rm CMB}} = y\left(x\frac{e^x+1}{e^x-1} - 4\right). \tag{4.1}$$

Here, $T_{\rm CMB} = 2.725$ K is the CMB temperature, x is a dimensionless frequency given by $x \equiv \frac{h\nu}{kT_{\rm CMB}} = \frac{\nu}{56.81\,{\rm GHz}}$, h is the Planck constant, k is the Boltzmann constant, and the dimensionless Compton-y parameter is defined as

$$y \equiv \int dl\, \sigma_T \frac{n_e k\,(T_e - T_{\rm CMB})}{m_e c^2}, \tag{4.2}$$

where σ_T is the Thomson cross section, m_e is the electron mass, c is the speed of light, n_e is the electron number density, T_e is the electron temperature, and the integral is performed over the line-of-sight distance l.

When observing the tSZ effect on the sky, a useful quantity is the angularly integrated Compton-y parameter, Y, given by

$$Y \equiv l_{\rm ang}^2 \int y(\boldsymbol{\theta}) d\boldsymbol{\theta}, \tag{4.3}$$

where $l_{\rm ang}$ is the angular diameter distance. For the SPT 150 GHz parameters from Spacek et al. (2016), this is $Y_{\rm SPT} = 2.7 \times 10^{-8}\,{\rm Mpc}^2 E_{60}$, where E_{60} is the total line-of-sight gas thermal energy $E_{\rm therm}$ in units of 10^{60} erg. For the ACT 148 GHz parameters

from Spacek et al. (2017), this is $Y_{\rm ACT} = 2.9 \times 10^{-8}\,{\rm Mpc}^2 E_{60}$. The values are slightly different due to the slightly different frequency sensitivities and beam profiles of the two telescopes. Y can additionally be scaled and written as (i.e. Planck Collaboration et al., 2013)

$$\widetilde{Y} \equiv \frac{Y}{l_{\rm ang}^2} \times E^{-2/3} \times \left(\frac{l_{\rm ang}}{500\ {\rm Mpc}}\right)^2, \tag{4.4}$$

where $E(z) \equiv \sqrt{\Omega_0(1+z)^3 + \Omega_\Lambda}$ is the Hubble parameter.

Spacek et al. (2016, 2017) use simple models of heating due to gravitation and AGN feedback to compare with the above observational equations. For gravity, they assume that as gas collapses and virializes along with an encompassing spherical halo of dark matter, it is shock-heated to a virial temperature $T_{\rm vir}$. For isothermal gas, this gives a total thermal energy of

$$E_{\rm therm,gravity} = \frac{3kT_{\rm vir}}{2}\frac{\Omega_b}{\Omega_0}\frac{M}{\mu m_p} = 1.5 \times 10^{60}\,{\rm erg}\,M_{13}^{5/3}(1+z), \tag{4.5}$$

where m_p is the proton mass, $\mu = 0.62$ is the average particle mass in units of m_p, and M_{13} is the mass of the halo in units of $10^{13} M_\odot$. Using the relation between halo mass and stellar mass described in Spacek et al. (2016, 2017), $M_{\rm stellar} = 2.8^{+2.4}_{-1.4} \times 10^{10} M_\odot\, M_{13}^{5/3}(1+z)^{5/2}$, this gives

$$E_{\rm therm,gravity} = 5.4^{+5.4}_{-2.9} \times 10^{60}\,{\rm erg}\,\frac{M_{\rm stellar}}{10^{11} M_\odot}(1+z)^{-3/2}. \tag{4.6}$$

This is the total thermal energy expected around a galaxy of stellar mass $M_{\rm stellar}$ ignoring both radiative cooling, which will decrease $E_{\rm therm}$, and AGN feedback, which will increase it.

For AGN feedback, they use the simple model described in Scannapieco & Oh (2004), where the black hole emits energy at the Eddington luminosity, $L_{\rm Edd} = 1.26 \times 10^{38} (M_{\rm BH}/M_\odot) {\rm erg\ s^{-1}}$ (e.g. Shankar et al., 2013), for a time $0.035\, t_{\rm dynamical}$, with $t_{\rm dynamical} \equiv R_{\rm vir}/v_c = 2.6\,{\rm Gyr}\,(1+z)^{-3/2}$, and the gas is heated by a fraction ϵ_k of the

total bolometric luminosity of the AGN. This gives

$$E_{\rm therm,feedback} = 4.1 \times 10^{60}\,{\rm erg}\,\epsilon_{k,0.05}\,\frac{M_{\rm stellar}}{10^{11}M_{\odot}}\,(1+z)^{-3/2}, \tag{4.7}$$

where $\epsilon_{k,0.05} \equiv \epsilon_k/0.05$ represents a typical efficiency factor of 5%.

4.3 The Horizon-AGN Simulation

The Horizon-AGN simulation is a cosmological hydrodynamical simulation that uses the adaptive mesh refinement Eulerian hydrodynamics code RAMSES (Teyssier, 2002). The simulation is described in more detail in Dubois et al. (2012, 2014) and Kaviraj et al. (2015, 2016), and here we will just restate some of the most relevant information. The simulation box is $100/h$ Mpc comoving on each side, with 1024^3 dark matter particles at a resolution of $8 \times 10^7 M_{\odot}$. The simulation grid is refined throughout the simulation, with a minimum cell size of 1 physical kpc. Gas cools through emission by H, He, and metals. Stars are created when the density of hydrogen gas reaches 0.1 cm^{-3}, and star particles have a resolution of $\approx 2 \times 10^6 M_{\odot}$.

Black holes are seeded at $10^5 M_{\odot}$ when the gas and stellar densities and stellar velocity dispersion are high, with a maximum accretion rate at the Eddington limit and a radiative efficiency of 0.1. When the accretion rate is high ($> 0.01 L_{\rm Edd}$), a quasar-like feedback mode is assumed with 1.5% of the accretion energy injected as thermal energy in the surrounding gas. When the accretion rate is low ($< 0.01 L_{\rm Edd}$), a radio feedback mode is assumed with bipolar jets at 10% efficiency. Feedback parameters are chosen to match the $M_{\rm BH} - M_{\star}$ and $M_{\rm BH} - \sigma_{\star}$ relations observed at $z = 0$. Black holes are said to merge when they are closer than 4 kpc and slower than their mutual escape velocity.

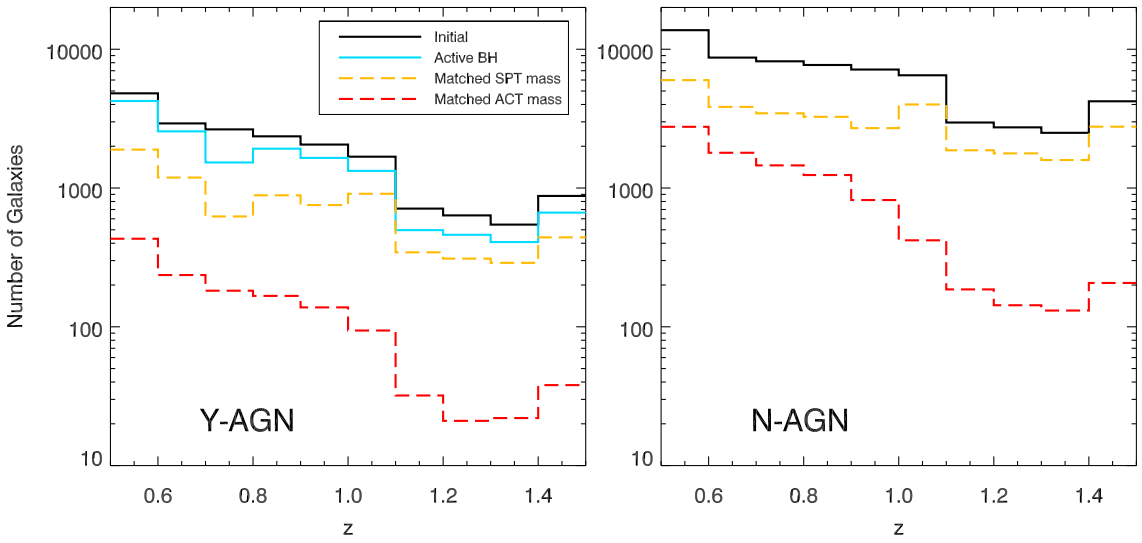

Figure 4.2: Number of galaxies per redshift bin for the initial population, after removing active black holes, and then after matching both the SpSPT and SpACT mass distributions. On the left is the Y-AGN simulation and on the right is the N-AGN simulation.

4.4 Data

We use the Horizon-AGN (abbreviated here as "Y-AGN") and Horizon-noAGN (abbreviated here as "N-AGN") simulations for our simulated galaxy data, and make comparisons with observational measurements from Spacek et al. (2016) (abbreviated here as "SpSPT") and Spacek et al. (2017) (abbreviated here as "SpACT"). In order to obtain as robust of a galaxy sample as possible, we collect data from the full available spread of redshift outputs: 0.52, 0.56, 0.59, 0.63, 0.67, 0.72, 0.76, 0.81, 0.86, 0.91, 0.97, 1.03, 1.09, 1.16, 1.23, 1.31, 1.40, and 1.49. We initially find all galaxies in the simulations with at least 250 star particles at each redshift. We then extract various parameters for each galaxy (stellar mass, age, star formation rate, and active black hole flag in the Y-AGN case) and corresponding dark matter halo (total mass, gas mass, stellar mass, black hole mass, and dark matter mass) in both Y-AGN and N-AGN. The active black hole flag says that a black hole is active if its mass is greater than $10^6 M_\odot$ and its luminosity is greater than $0.01 L_{\rm Edd}$. The stellar mass is taken

within a radius R_{200}, defined as the radius enclosing an overdensity of 200 times the critical density, given by

$$\frac{M(< R_{200})}{\frac{4}{3}\pi R_{200}^3} = 200\rho_{\rm c}(z), \tag{4.8}$$

where $M(< R_{200})$ is the mass enclosed within R_{200}, and $\rho_{\rm c}(z) = 3H^2(z)/(8\pi G)$. We then perform a cut on the galaxies corresponding to the selection criteria in SpSPT and SpACT, requiring $M_{\rm stellar} \geq 10^{11} M_{\odot}$, Age ≥ 1 Gyr, and a non-active black hole in the Y-AGN case. In addition, to prevent spurious measurements from galaxies near the edge of the simulation box, we require dark matter halos to be at least 10 R_{200} away from any edge. The simulation is periodic and these galaxies could be correctly measured by including the other side of the box, but since only a handful of galaxies are excluded using this constraint we decide to use this cut for simplicity. The number of galaxies left after the initial parameter cuts and the active black hole cut at each redshift bin is shown in Figure 4.2.

We will note that we see a steady increase in the fraction of galaxies that are flagged as active as we increase in redshift, generally $< 20\%$ for $0.5 < z < 1.0$ (15% mean) and $> 20\%$ for $1.0 < z < 1.5$ (25% mean). This makes sense, since $z \approx 2$ represents the peak of AGN activity, and it should decrease for lower z. The $0.7 < z < 0.8$ bin is the one outlier, with 42% of the galaxies flagged as active. This is due solely to the $z = 0.76$ data, which flagged 72% of its galaxies as active, much more than it should have. This does not have any major effect on our results, though, since the lower redshift galaxies are plentiful and the final SpSPT and SpACT matching cuts are limited by the number of higher redshift galaxies.

For each galaxy, we use the electron pressure to compute Compton-y values (Equation 4.2) and then project these values into the x, y, and z directions. We then select a square region around each galaxy and simulate measurements corresponding to the beam and pixel sizes in both SpSPT and SpACT. For SpSPT, we use regions that are

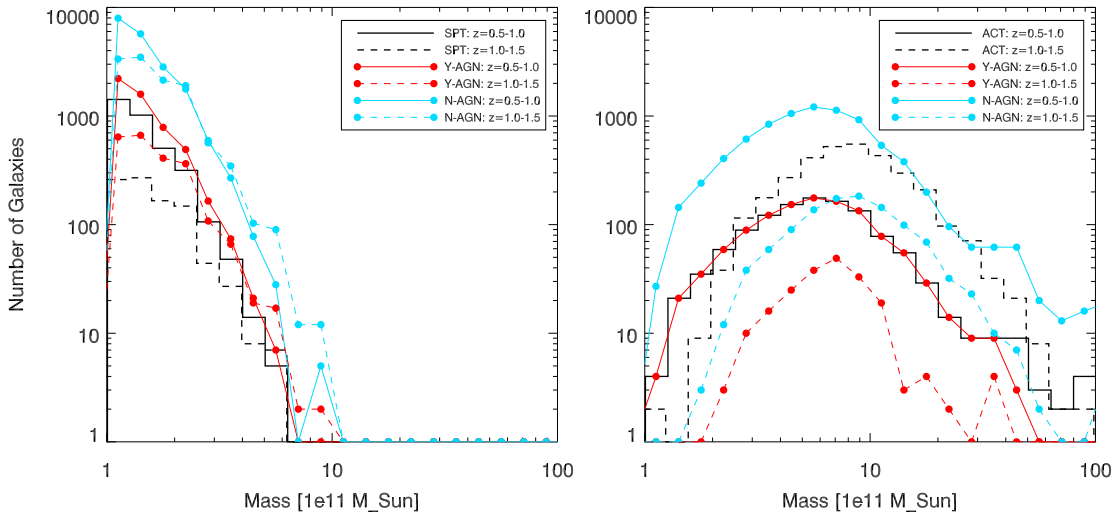

Figure 4.3: Mass selection comparisons.

8.25 × 8.25 arcmin, 33 × 33 pixels, convolved with a 1.15 arcmin FWHM Gaussian (corresponding to the 150 GHz SPT beam). For SpACT, we use regions that are 8.36 × 8.36 arcmin, 17 × 17 pixels, convolved with a 1.44 arcmin FWHM Gaussian (corresponding to the 148 GHz ACT beam). This results in a selection of galaxies for both Y-AGN and N-AGN at $0.5 < z < 1.5$ with tSZ measurements in the x, y, and z projections matching both SpSPT and SpACT. For simplicity, we will use only the x projections from now on, with the y and z results being very similar.

4.5 Measurements

In order to compare the simulated galaxies with the observational galaxies, we randomly build a population of simulated galaxies until their mass distribution matches the histogram distributions in SpSPT and SpACT. The matched distribution is scaled by whichever bin has the lowest fraction of Horizon galaxies compared to that bin for SpSPT or SpACT. An issue arises since the SpACT mass distribution is skewed to higher masses while the overall Horizon distributions favor lower masses. This makes it difficult to match the SpACT distribution at the highest masses, so instead

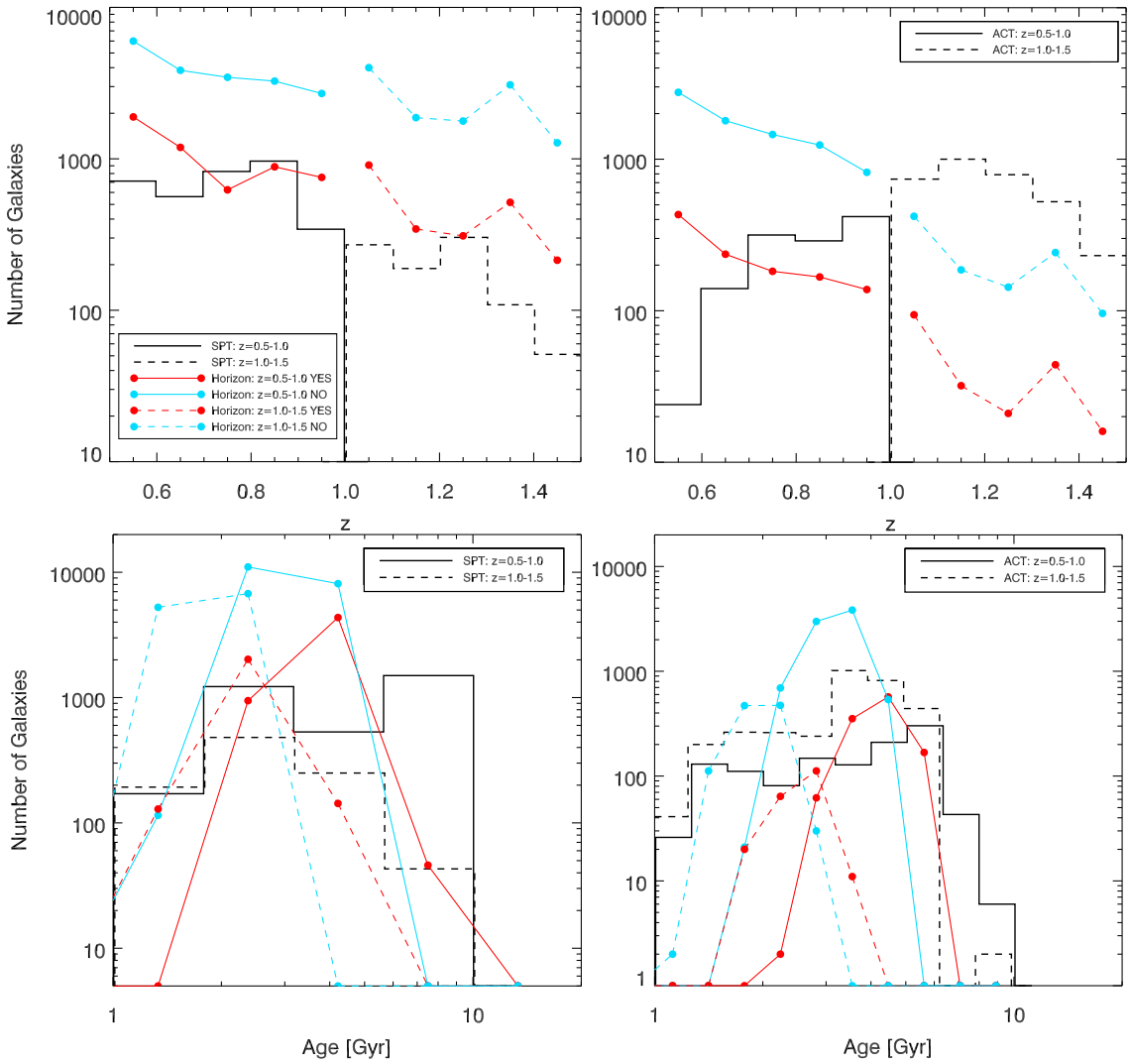

Figure 4.4: Redshift and age selection comparisons. The left plots are comparisons with SPT and the right plots are comparisons with ACT.

we choose some mass limit for each Horizon subset where we just keep all Horizon galaxies above that mass. This is especially clear for the Y-AGN $z = 1.0 - 1.5$ line in the right plot of Figure 4.3, where we only match the SpACT distribution up to $\approx 10^{12} M_{\odot}$ and keep every galaxy above that. The original SpSPT and SpACT distributions for mass along with the matched Horizon distributions are shown in Figure 4.3. The resulting SpSPT, SpACT, and Horizon distributions for redshift and age are shown in Figure 4.4, the final number of Horizon galaxies at each redshift bin after

Final bin:	Number	N(SpSPT/SpACT)
SPT low-z Y-AGN:	5345	937
SPT low-z N-AGN:	19249	937
SPT high-z Y-AGN:	2293	240
SPT high-z N-AGN:	12004	240
ACT low-z Y-AGN:	1154	227
ACT low-z N-AGN:	8073	227
ACT high-z Y-AGN:	207	529
ACT high-z N-AGN:	1087	529

Table 4.1: Final cumulative numbers for each redshift bin ("low-z" $= 0.5 < z < 1.0$ and "high-z" $= 1.0 < z < 1.5$) of each corresponding survey, compared with the numbers from SpSPT and SpACT that included Planck contamination modeling.

this matching are shown in Figure 4.2, and the final number of total galaxies in each redshift bin ("low-z" $= 0.5 < z < 1.0$ and "high-z" $= 1.0 < z < 1.5$) for each survey is given in Table 4.1.

The Horizon redshift distributions follow SpSPT well, with the number of galaxies decreasing as redshift increases. They do not follow SpACT as well, since SpACT peaks at higher redshifts while the mass distribution of SpACT requires a selection of lower redshift, higher mass Horizon galaxies. The Horizon age distributions are similar to those from SpSPT and SpACT, though N-AGN galaxies tend to be younger than Y-AGN galaxies.

A comparison of averaged parameters from SpSPT and SpACT with the final Horizon galaxies is shown in Table 4.2. Notice that the average redshifts of the Horizon galaxies are very close to the corresponding SpSPT and SpACT bins except for the SpACT low-z bin due to the fact that it drops off drastically towards $z = 0.5$. The average masses are all very similar except for the Y-AGN SpACT case, which

Survey	z	$\langle z \rangle$	$\langle l^2_{\rm ang} \rangle$ (Gpc^2)	$\langle M \rangle$ ($10^{11} M_\odot$)	$\langle$Age$\rangle$ (Gyr)	$\langle z \rangle_M$	$\langle l^2_{\rm ang} \rangle_M$ (Gpc^2)	Y (10^{-7}Mpc^2)
SPT	0.5-1.0	0.72	2.30	1.51	4.34	0.72	2.30	$2.3^{+0.9}_{-0.7}$
Y-AGN SPT	0.5-1.0	0.70	2.22	1.52	3.91	0.70	2.23	2.67
N-AGN SPT	0.5-1.0	0.71	2.26	1.52	3.05	0.70	2.25	1.05
SPT	1.0-1.5	1.17	3.02	1.78	2.64	1.19	3.03	$1.9^{+2.4}_{-2.0}$
Y-AGN SPT	1.0-1.5	1.20	3.04	1.72	2.46	1.20	3.03	3.05
N-AGN SPT	1.0-1.5	1.22	3.05	1.72	1.85	1.22	3.05	0.79
ACT	0.5-1.0	0.83	2.56	7.81	3.80	0.86	2.61	$1.2^{+1.4}_{-1.4}$
Y-AGN ACT	0.5-1.0	0.69	2.21	7.00	4.25	0.69	2.20	10.82
N-AGN ACT	0.5-1.0	0.69	2.22	8.10	3.22	0.69	2.22	2.26
ACT	1.0-1.5	1.20	3.04	10.1	3.56	1.21	3.05	$1.9^{+1.1}_{-1.0}$
Y-AGN ACT	1.0-1.5	1.19	3.02	7.67	2.59	1.18	3.02	17.96
N-AGN ACT	1.0-1.5	1.20	3.04	10.30	1.96	1.19	3.03	4.01

Table 4.2: Mean and mass-averaged values for several relevant galaxy parameters, comparing SpSPT and SpACT with the matched Horizon galaxies.

struggles to match the high redshift distribution of SpACT with its limited number of galaxies. SpSPT and SpACT galaxies tend to be older than the Horizon galaxies, again except for the Y-AGN SpACT case which has older galaxies due to its greater number of low redshift galaxies compared to SpACT.

When compared to low-z SpSPT, the Y-AGN Y value is high by 0.4σ, while the N-AGN value is low by 1.8σ (this is simply compared to the observational results plus errors, not taking into account simulation uncertainties). For high-z SpSPT, the Y-AGN value is high by 0.5σ while the N-AGN value is low by 0.6σ. When compared to low-z SpACT, the Y-AGN value is high by 6.9σ while the N-AGN value is high by 0.8σ. For high-z SpACT, the Y-AGN value is high by 14.6σ while the N-AGN value is high by 1.9σ. From these numbers, it appears that the low-z SpSPT results suggest

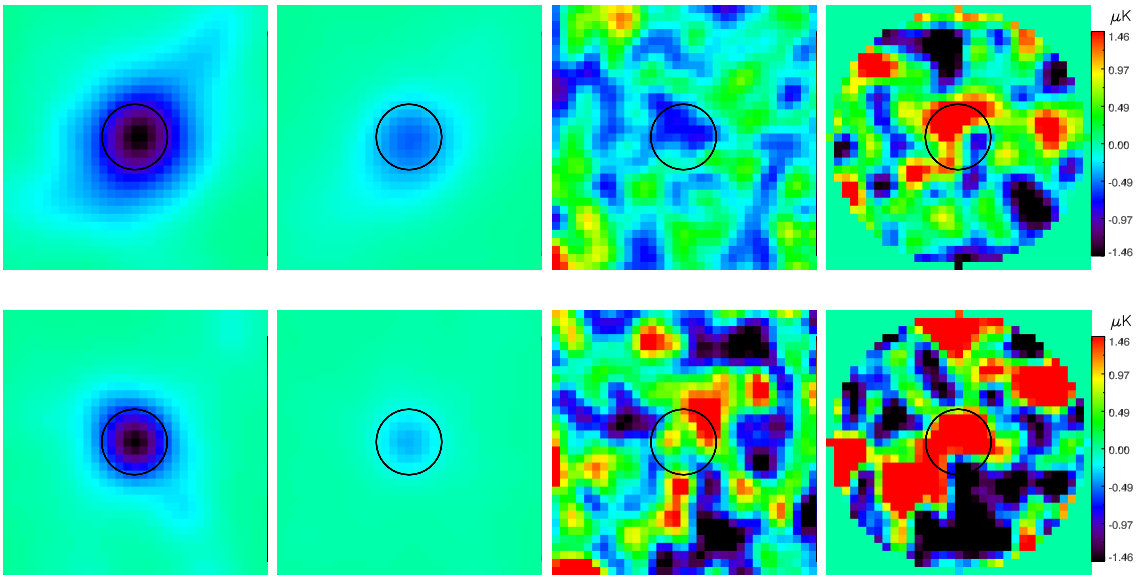

Figure 4.5: SpSPT 150 GHz stacked averages around galaxies for Y-AGN (left), N-AGN (left middle), low-z (top), and high-z (bottom). On the right are the initial stacking results from Spacek et al. (2016) with the same scale, for 150 GHz (right middle) and 220 GHz (right). Black circles represent a 1 arcmin radius.

AGN feedback energy, while the high-z SpSPT results do not distinguish between the models. On the other hand, both the low-z and high-z SpACT results heavily disfavor AGN feedback energy, with the low-z measurements strongly favoring N-AGN.

Final average stacked stamps for the SpSPT redshift bins are shown in Figure 4.5 for Y-AGN and N-AGN, along with the initial stamps from SpSPT 150 and 220 GHz with matching scales. Final average stacked stamps for the SpACT redshift bins are shown in Figure 4.6 for Y-AGN and N-AGN, along with the initial stamps from SpACT 148 and 220 GHz with matching scales. The plot scales for both figures are set by the highest and lowest pixels out of all four Horizon stamps. The low-z SpSPT stamps indicate a larger extent to the signal than for the high-z stamps, perhaps due to both larger sizes at lower redshifts and longer times for the hot gas to expand (the average ages are more than 1.5 times as long). This effect is not seen as clearly for SpACT, possibly due to the pixels being twice as large or the masses, and therefore signal, being so much greater. These stamps also indicate that the 1 arcmin radius

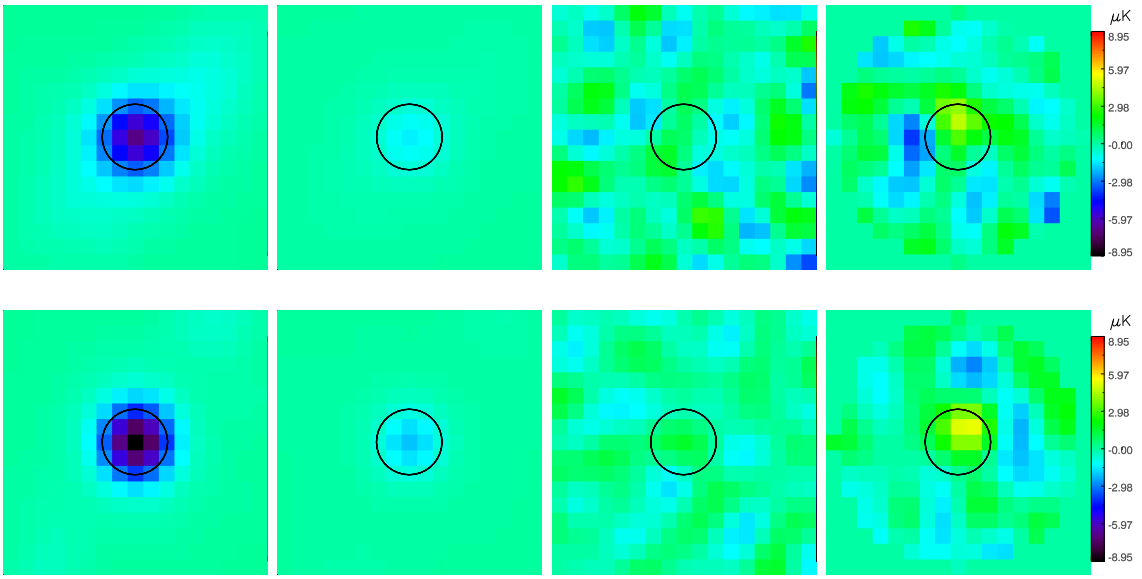

Figure 4.6: SpACT 148 GHz stacked averages around galaxies for Y-AGN (left), N-AGN (left middle), low-z (top), and high-z (bottom). On the right are the initial stacking results from Spacek et al. (2017) with the same scale, for 148 GHz (right middle) and 220 GHz (right). Black circles represent a 1 arcmin radius.

measurement aperture might be too small to contain the full tSZ signal. The low-z SpSPT stamps would have the full signal better contained within a twice as large aperture of 2 arcmin radius, while the high-z SpSPT stamps would need a 1.5-1.75 arcmin radius aperture. The SpACT stamps appear to need a 1.5-2 arcmin radius aperture to contain the full signal.

Mass binned averages for a subset of nine redshifts spanning the full range comparing Horizon to the model predictions are shown in Figure 4.7. There are several trends to notice here. Both the Y-AGN and N-AGN curves seem to roughly follow the $\tilde{Y} \propto Y \propto E_{\rm therm} \propto M_\star$ relation indicated by the simple models in Equations (4.6) and (4.7), except for the lowest redshifts of $z = 0.52$ and 0.63 where $\tilde{Y}$ appears to stay almost flat for the lower masses. The Y-AGN and N-AGN curves also seem to stay roughly the same distance apart, though at the highest redshift the N-AGN line falls right on the model prediction while the Y-AGN line is considerably higher than the model prediction. This could be due to the Horizon AGN feedback prescription

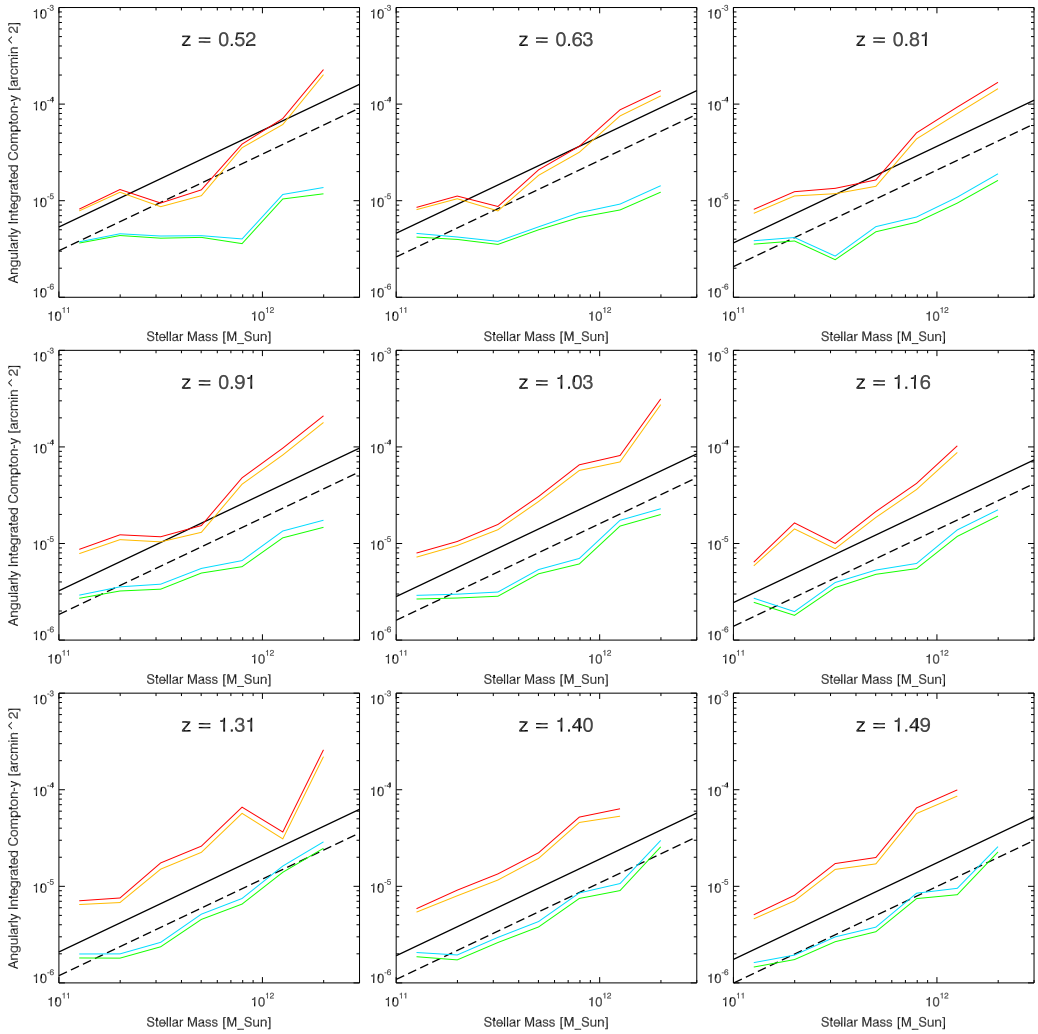

Figure 4.7: Comparison between angularly-integrated, mass-binned Compton-y measurements at a subset of simulation redshifts. Red is SPT-matched Y-AGN, orange is ACT-matched Y-AGN, blue is SPT-matched N-AGN, and green is ACT-matched N-AGN.

using more powerful feedback (e.g. longer feedback times, multiple feedback episodes, radio-mode jet feedback). The Horizon lines then both drop relative to the models as the redshift decreases, likely due to an increasingly larger time for radiative cooling to happen, which the models do not account for.

Final mass-binned averages for each redshift bin with each telescope, compared to the model predictions and the SpSPT and SpACT results, are shown in Figure 4.8. Here we see that there is not a distinct redshift dependence as predicted by the

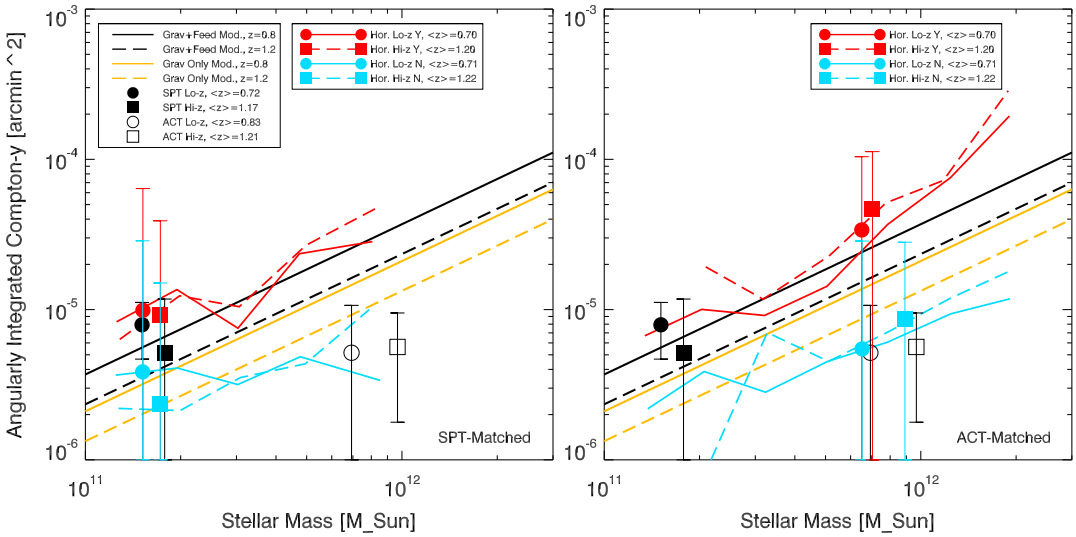

Figure 4.8: Final matched stack values for SPT and ACT. The error bars on the Horizon average points (red and blue) represent the standard deviation of the corresponding galaxy samples.

models, or if anything the high-z values seem to be larger more often than the low-z values, contrary to the model predictions. This is possibly due to the fact that the curves are averaged over a range of redshifts, as well as the possibility of different behavior due to radiative cooling. Looking at the final measurements from SpSPT and SpACT, we see as expected that the black SpSPT measurements are consistent with the Y-AGN curves, although it is hard to rule out the N-AGN curves which are about 1σ away. On the other hand, the red SpACT measurements are consistent with the N-AGN curves and not at all consistent with the Y-AGN curves.

We also gain some insight on potentially troublesome trends seen in the observational results. The SpSPT low-z results are actually quite a bit higher than the simple AGN feedback model predicts, while the SpACT results are all significantly lower than the simple gravitational model. Interestingly, both of these trends are reproduced in the Horizon results, suggesting it might not be the measurements that are errant, but instead the simple models are lacking in details that the Horizon simulations are able to incorporate.

4.6 Discussion

In this work, we have taken the large-scale cosmological hydrodynamical simulation Horizon-AGN, with AGN feedback, and its counterpart without AGN feedback, and extracted a sample of galaxies that match those from Spacek et al. (2016, 2017). We have then performed the same stacking procedure as SpSPT and SpACT, measuring the tSZ effect by redshift, mass, and telescope survey. Our results can be summarized as follows:

(i) Low-z galaxies (i.e. $0.5 < z < 1.0$) appear to have a tSZ signal with significantly more angular extent than high-z galaxies ($1.0 < z < 1.5$). This may be due to the fact that at these redshifts, lower redshift means a closer galaxy which means a larger angular extent. It may also be related to longer times since the peak of AGN activity around $z \approx 2$, giving hot gas impacted by AGN feedback longer time to expand.

(ii) The angularly integrated tSZ effect aperture size of 1 arcmin radius appears to poorly capture the total stacked tSZ signal in both redshift bins and both Y-AGN and N-AGN simulations. This means less data (i.e. pixels with our signal of interest) and therefore a less statistically robust result than could be possible. It looks like an aperture of 1.5-2.0 arcmin radius would be more effective in capturing the full signal, but would not be too large as to excessively increase the noise.

(iii) At low redshifts ($z \approx 0.52 - 0.63$), both the Y-AGN and N-AGN $\tilde{Y}$ measurements appear to be flat with respect to mass at low masses ($M \lesssim 10^{12} M_{\odot}$), especially N-AGN. This is not predicted by the simple models.

(iv) While at the highest redshift ($z = 1.49$) the N-AGN $\tilde{Y}$ curve follows the model very well, the Y-AGN curve is significantly higher than the model predicts. This might be due to the differences in how the simple model and Horizon handle the amount of AGN feedback energy, either in magnitude or in duration.

(v) Both the Y-AGN and N-AGN $\tilde{Y}$ curves appear to systematically drop relative to the model predictions as the redshift decreases. This is likely due to the fact that the models do not take into account the radiative cooling of the galaxies and surrounding gas, which would lower the tSZ signal, and which would increase in magnitude at lower redshifts as gas has longer to cool.

(vi) The models predict a distinct increase in $\tilde{Y}$ going from high-z to low-z, while the Horizon measurements show either no redshift dependence, or perhaps even an opposite effect where $\tilde{Y}$ increases going from low-z to high-z.

(vii) The SpSPT results are consistent with the Y-AGN curves and inconsistent with the N-AGN curves at around a 1σ level, while the SpACT results are consistent with the N-AGN curves and inconsistent with the Y-AGN curves at $\gtrsim 7\sigma$. Furthermore, the discrepancy between the SpSPT low-z results being higher than the Y-AGN model curves is promisingly supported by the Horizon Y-AGN curves, which tend to be higher than the corresponding models. Similarly, the discrepancy between the SpACT high-z results being lower than the N-AGN model curves is reproduced by the Horizon N-AGN curves, which tend to be lower than the corresponding models.

Overall, it would appear that the SpSPT results are mostly consistent with AGN feedback (although not very strongly), while the SpACT results are mostly consistent with no AGN feedback. These results seem to be inconsistent with each other, and it is not clear how to resolve this issue. It may perhaps be the case that the differences in galaxy selection, redshift, mass, and age distribution, and contamination removal between the two studies creates the need to perform their tSZ stacking analyses differently than they were done. There is also the fact that these studies are essentially unprecedented in their attempts to measure the tSZ effect around moderate redshift elliptical galaxies using the first publicly available data from the SPT and ACT surveys. There are also clearly still a lot of open questions that should be

investigated regarding these tSZ stacking measurements, as indicated by many of the above summary points.

There is a lot of further work to be done in the near future on these measurements. It may be interesting to investigate redshifts lower than 0.5 and higher than 1.5, as well as different cuts on galaxy parameters, to see if improvements can be made in these tSZ stacks and to understand the overall evolution of the hot gas around galaxies. In addition to the stellar mass of galaxies, it could be useful to explore relations between dark matter halo masses and the tSZ effect. This work could also be expanded by doing similar simulations to Horizion-AGN but using various models of AGN feedback, in order to understand a much more detailed picture of the AGN feedback process that is giving the observational results. Finally, there are several next-generation CMB detectors currently running and potentially releasing data soon, including Advanced-ACT and SPT-Pol, which have a large increase in sensitivity as well as more frequency bands. These will give much better tSZ measurements and the extra frequency bands would improve the ability to deal with contamination to the tSZ signal. These measurements can then provide future simulation work with even more robust observations to compare to and lead to increasingly constrained results.

Chapter 5

CONCLUSION

In the past two decades, galaxy and cluster observations have started revealing a more complex history for structure formation in the Universe than was previously thought. Recent cosmological simulations have also shown that many outstanding problems in the theory of galaxy and cluster evolution are significantly resolved by the inclusion of non-gravitational heating in the form of energetic feedback from AGNs. The true nature of AGN feedback, though, remains highly uncertain due to the difficulty of direct observations. The recent generation of microwave telescopes, like SPT, ACT, ALMA, and Planck, has opened up for the first time a new realm of possibilities in directly measuring the impact of AGN feedback on galaxies and clusters through measurements of anisotropies in the CMB caused by the tSZ effect. In this work, we have explored some of these new possibilities by using SPT and ACT data to measure the thermal energy in gas around massive moderate-redshift elliptical galaxies using the tSZ effect, and we have used the large Horizon-AGN cosmological simulation to better understand the implications for these tSZ measurements on AGN feedback models.

5.1 Results

In Chapter 2, we used BCS and VHS data to detect and measure elliptical galaxies with SExtractor and select them using gzK_s colors. We then applied cuts, requiring age $\geq$ 1 Gyr, mass $\geq 10^{11} M_{\odot}$, and SSFR ≤ 0.01 Gyr^{-1}, and we split the galaxies into two redshift bins, "low-z" ($0.5 < z < 1.0$) and "high-z" ($1.0 < z < 1.5$). We attempted to remove any possible contamination due to dust, AGNs, or clusters.

The result was 3394 low-z galaxies and 924 high-z galaxies. We made stacks of these galaxies in 150 and 220 GHz SPT data, and we saw a 2.2σ tSZ signal in the low-z bin, suggesting a gas thermal energy of $4.1 \pm 1.9 \times 10^{60}$ erg, but with contamination still clearly present. We used dust and synchrotron source counts to model and remove possible undetected contamination, and this resulted in thermal energies of $8.1^{+3.0}_{-2.5} \times 10^{60}$ erg at low-z and $6.7^{+8.3}_{-7.0} \times 10^{60}$ erg at high-z, detections at 3.5σ and 0.9σ confidence levels, respectively. We then included Planck data in our contamination removal and measured thermal energies of $7.6^{+3.0}_{-2.3} \times 10^{60}$ erg for 937 low-z galaxies and $6.0^{+7.7}_{-6.3} \times 10^{60}$ erg for 240 high-z galaxies, detections at 3.6σ and 0.9σ confidence levels, respectively. Using simple models of gravitational heating, we estimated non-gravitational thermal energies of $4.0^{+3.6}_{-4.3} \times 10^{60}$ erg for low-z and $E_{\rm therm,feed,dat} = 3.0^{+7.9}_{-7.0} \times 10^{60}$ erg for high-z, suggesting corresponding AGN feedback efficiencies of $7.5^{+6.5}_{-8.0}\%$ for low-z and $6.5^{+17.5}_{-15.5}\%$ for high-z. We also found that the Anderson-Darling goodness-of-fit test only helped us constrain our contaminant modeling parameters and not the thermal energy results.

In Chapter 3, we used SDSS and WISE data to select galaxies with the same requirements as in Chapter 2. The result was 1179 low-z galaxies and 3274 high-z galaxies. The initial stacks of these galaxies in 148 and 220 GHz ACT data showed only a hint of a tSZ signal at low-z and significant contamination in all cases. We did the same contamination modeling as in Chapter 2, and the results were thermal energies of $4.5^{+5.4}_{-5.1} \times 10^{60}$ erg at low-z and $7.0^{+4.0}_{-3.7} \times 10^{60}$ erg at high-z, representing 0.85σ and 1.78σ confidence levels, respectively. After including Planck data, we saw thermal energies of $5.6^{+5.9}_{-5.6} \times 10^{60}$ erg for 227 low-z galaxies and $7.0^{+4.7}_{-4.4} \times 10^{60}$ erg for 529 high-z galaxies, representing 0.97σ and 1.50σ confidence levels, respectively. Using simple models of gravitational heating, we estimated non-gravitational thermal

energies of $-9.5^{+16.1}_{-10.0} \times 10^{60}$ erg for low-z and $-8.9^{+16.5}_{-9.7} \times 10^{60}$ erg for high-z, both consistent with gravitational-only heating.

In Chapter 4, we used the Horizon-AGN ("Y-AGN") and Horizon-noAGN ("N-AGN") cosmological simulations to select galaxies using the same requirements as in Chapters 2 and 3, with the goal of making comparison measurements of the tSZ effect to both those previous works. We utilized simulation outputs from redshifts of 0.52, 0.56, 0.97, 1.03, 1.09, 1.31, and 1.49. We then matched the redshift distributions of those previous works and made our tSZ measurements match the pixel and beam sizes of the SPT and ACT work. Our resulting SPT-matched galaxy sample consisted of 2195 low-z Y-AGN, 10,240 low-z N-AGN, 1485 high-z Y-AGN, and 9374 high-z N-AGN. Our resulting ACT-matched galaxy sample consisted of 751 low-z Y-AGN, 3506 low-z N-AGN, 1071 high-z Y-AGN, and 6759 high-z N-AGN. After stacking the tSZ signals, we measured SPT-matched thermal energies of 16.3×10^{60} erg for low-z Y-AGN, 5.0×10^{60} erg for low-z N-AGN, 16.4×10^{60} erg for high-z Y-AGN, and 4.5×10^{60} erg for high-z N-AGN. We measured ACT-matched thermal energies of 15.0×10^{60} erg for low-z Y-AGN, 4.4×10^{60} erg for low-z N-AGN, 14.7×10^{60} erg for high-z Y-AGN, and 4.2×10^{60} erg for high-z N-AGN.

We found that these numbers, which are binned by mass and plotted in Figure 4.8, indicated that the SPT results from Chapter 2 are consistent with the Y-AGN results (with the low-z and high-z measurements within 0.4σ and 0.5σ, respectively, of the observational results) and discrepant with the N-AGN results, especially at low-z (with the low-z measurement off by 1.8σ from the observational results and the high-z measurement within 0.6σ). Additionally, the ACT results from Chapter 3 are consistent with the N-AGN results, especially at low-z (with the low-z measurement within 0.8σ of the observational results and the high-z measurement off by 1.9σ), and they are not at all consistent with the Y-AGN results (with the low-z and high-z

measurements off by 6.9σ and 14.6σ, respectively). We also found that the simple models for gravitational and AGN feedback heating used in Chapters 2 and 3 were potentially underestimating AGN feedback energies in general, and overestimating all energies at lower redshifts due to ignoring radiative cooling. We additionally found that the 1 arcmin radius apertures used to measure the angularly integrated tSZ effect were possibly too small and missing a significant amount of the extended tSZ signal, although the impact of increasing the size of the apertures is uncertain due to the resulting increase in noise uncertainty.

The results presented here lead to several interesting and open questions regarding AGN feedback. The SPT work done in Chapter 2 suggested the presence of non-gravitational heating at a level of about 0.9σ at low-z and 0.4σ at high-z, and while this is very uncertain due to both the measurements and the models used, it hints at the presence of AGN feedback. On the other hand, the ACT work done in Chapter 3, using a process very similar to that of Chapter 2, highly suggested the presence of only gravitational heating, with no hint of any other heating sources. The simulation results from Chapter 4 lended even more support to both of these contradictory conclusions. For consistent results, there are a few possibilities that seem most likely. First, the statistical confidence in the SPT results ($\approx 1\sigma$ at the most) is not overwhelming, so the SPT galaxy sample might have happened to have contained more tSZ signal than would be reflected in a complete sample, and better measurements would actually support only gravitational heating. It is also possible that the contaminant signal was overcompensated for and therefore the resulting tSZ signal was higher than it should be, or that the SPT galaxies, which tend to be lower redshift, are in larger group and cluster gravitational wells that have additional gravitational heating that is not accounted for. For the ACT results, it is possible that the contaminant signal was not accounted for fully and still dominates the final

results, resulting in too small of a tSZ signal. It is worth noting, though, that the methods used in both cases to account for and remove contamination were very similar. Additionally, there is uncertainty in the parameter calculations, especially for redshift and mass, that could have a significant effect on the results. The Compton-y measurements depend on redshift, e.g. resulting in a shift along the y-axis in Figure 4.8, and incorrect masses would result in a shift along the x-axis. Finally, it may be possible that there are additional effects on the thermal energies of higher mass elliptical galaxies that neither the simple models nor Horizon take into account, affecting the ACT results more which involve galaxies with much higher masses than both the SPT work and Horizon work.

5.2 Future Work

Clearly, there is room for a lot more work to be done on tSZ measurements around moderate redshift elliptical galaxies. For the observational work done here, the results are limited by the number of galaxies, the telescope sensitivities, and the effectiveness of modeling and removing contaminating signals. In Chapter 2 we only had SPT data at 150 and 220 GHz from 2008 covering 95 deg^2, and we used Planck data to model and remove undetected dusty contaminants. Due to our selection criteria, the larger beam size of Planck greatly reduced our sample of galaxies and therefore our measurement significance. However, the full data from the first-generation SPT observations includes 4 years of observations (2008-2011) and 3 bands (95, 150, and 220 GHz). With the 95 GHz band, which has a beam FWHM of 1.6 arcmin (Bleem et al., 2015), an additional 3 years of data, and greater sky coverage (2500 deg^2), constraints on contaminant signal could be improved while also preserving the full galaxy sample size, potentially leading to a much better measurement. Since the work done in Chapter 2 there have also been updates to both the BCS and VHS

with greater sensitivity and larger survey areas: the Dark Energy Survey (DES; Dark Energy Survey Collaboration et al., 2016) and VHS data release 3, released in December 2015. Starting back in 2012, the second-generation SPT detector, SPTpol, is collecting 4 seasons of data, covering 625 deg^2, with bands centered at 90 and 150 GHz (Austermann et al., 2012). The tSZ-relevant 150 GHz band is more than 3 times as sensitive with SPTpol than it was with the first-generation SPT detector used in Chapter 2.

In Chapter 3 we only had ACT data at 148 and 218 GHz from 2008 and 2009, along with Planck. The full data from the first-generation ACT Millimeter Bolometric Array Camera (MBAC) observations includes 4 years of observations (2007-2010) and 3 bands (148, 218, and 277 GHz). Like with the SPT 95 GHz band, the 277 GHz ACT band, which has a beam FWHM of 0.9 arcmin (Das et al., 2011), would allow improved constraints on the dust signal. Additionally, from 2013 to 2016 the second-generation ACT detector, ACTPol, collected 3 seasons of data, covering a few thousand square degrees, with bands centered at 97 and 148 GHz (Thornton et al., 2016). The tSZ-relevant 148 GHz band is more than twice as sensitive with ACTPol than it was with MBAC, used in Chapter 3. The sky coverage of a few thousand square degrees, compared with $\approx$300 deg^2 in Chapter 3, would also allow for a much larger selection of galaxies to be measured, and the 97 GHz band could provide another measurement of the tSZ signal and additional constraints on potentially contaminating synchrotron and dust emission.

While improved SPT and ACT data can give improved constraints on AGN feedback by measuring and stacking a lot of galaxies, it also may be possible to constrain AGN feedback by using dedicated measurements of a handful of promising galaxies with large radio telescopes and arrays. The tSZ signal is frequency dependent, and it turns out to be greater at lower frequencies. For example, the tSZ signal at 90 GHz

is 1.7 times greater than it is at 150 GHz, and at 45 GHz it is 2 times greater than at 150 GHz. This means the tSZ signal for the Very Large Array (VLA) and Atacama Large Millimeter/submillimeter Array (ALMA) telescopes is close to twice as strong as it is for SPT and ACT measurements. AGN feedback simulations looking at the tSZ effect (e.g. Scannapieco et al., 2008) suggest a sensitivity level of about 1 μK arcmin^2 to have a chance at constraining AGN feedback. Using the online sensitivity calculators for VLA and ALMA, where sensitivity $\times$ beam area = 1 μK arcmin^2, gives needed observation times of 4.33 hours for the VLA (FWHM = 0.038 arcmin, sensitivity = 0.88 mK) and 9.3 minutes for ALMA (FWHM = 0.1 arcmin, sensitivity = 0.13 mK). The sample values used for the VLA calculation include array configuration D, 25 antennas, 45 GHz frequency, and 8 GHz bandwidth, and for ALMA include 90 GHz frequency, 7.5 GHz bandwidth, and the 12m array with 40 antennas. These are rough calculations, but they highlight the reasonable amount of time needed at either of these telescopes to make significant measurements. There may be additional difficulties in these measurements due to the high resolutions, though, since at a redshift of 1, an angular size of 0.04 and 0.1 arcmin correspond to approximate physical sizes of 19 and 49 kpc, respectively. This means these telescopes could possibly resolve the regions of interest and therefore be limited by surface brightness concerns. Nevertheless, these types of measurements might prove to be effective.

There are also other radio telescopes with large sizes and high sensitivities. The Green Bank Telescope (GBT) has potential for significant tSZ measurements. It can operate at 30 GHz with a 0.37 arcmin resolution and reach fairly high sensitivity within a few hours. One major obstacle is the confusion limit, which is around 20 μK at this frequency, while the necessary sensitivity is close to 9 μK. Stacking measurements from a fairly small number of galaxies could fix this problem. There are also $1/f$ gain fluctuations that essentially limit the possible integration time,

especially at the higher frequencies of interest. These are big problems, but it could be worth looking into more closely with the wide array of receivers, backends, and observing techniques available to the GBT. Other possibilities include the Institut de Radioastronomie Millimetrique (IRAM) 30m telescope and Northern Extended Millimeter Array (NOEMA).

A future instrument that will make powerful CMB measurements is the TolTEC camera mounted on the Large Millimeter Telescope (LMT; toltec.astro.umass.edu/about.php), a 50 m telescope in Mexico. It will have three bands at 125, 214, and 273 GHz, with beam FWHM sizes of 9.5, 6.3, and 5 arcsec, respectively. To give an example of its potential, the planned TolTEC Large Scale Structure Survey will map 100 $\deg^2$ of the sky to depths of 0.18, 0.24, and 0.26 mJy at 125, 214, and 273 GHz, respectively (toltec.astro.umass.edu/science_lss.php). To put this in perspective, the depths of the SPT-SZ survey used in this work are 42, 18, and 85 μK arcmin at 95, 150, and 220 GHz, respectively (Schaffer et al., 2011). To compare TolTEC with SPT-SZ we can use the Jy-to-K conversion factors for the TolTEC beam sizes and frequencies, which are 0.868 Jy/K for 125 GHz, 0.672 Jy/K for 214 GHz, and 0.658 Jy/K for 273 GHz. Converting the TolTEC depths from mJy to μK using the above factors and then multiplying by the TolTEC beam sizes in arcmin gives comparable TolTEC values of 25, 17, and 14 μK arcmin at 125, 214, and 273 GHz, respectively. To directly compare, then, we have depths of 42 and 18 μK arcmin at 95 and 150 GHz for SPT-SZ, and 25 μK arcmin at 125 GHz for TolTEC. Additionally, we have a depth of 85 μK arcmin at 220 GHz for SPT-SZ, and 17 μK arcmin at 214 GHz for TolTEC. It is apparent that the TolTEC CMB sensitivities will be comparable, and likely significantly better, than the sensitivities of the telescopes used in this work, while having vastly better resolution. This could allow for deep, accurate studies of

the regions around the galaxies investigated in this work without having to worry about contamination from the central galaxy.

There are also many possibilities for further simulation work. The Horizon simulation contains more redshift coverage, filling in the gaps in the data used in Chapter 4. It also contains larger and smaller redshifts than those used here, which could be useful in doing further investigation on AGN feedback signals over cosmic time. The Horizon simulation also uses a single prescription for implementing AGN feedback, and in order to make distinctions between different possible modes and magnitudes of feedback it will be important to perform multiple simulations with varying feedback models. The stacking analysis used in this work did not use any sort of weighting scheme, but by analyzing different ways of weighting the tSZ stacks in simulations, there may be weighting methods that optimize the ability to distinguish between different AGN feedback models. Finally, a deeper look into the physical processes going on in these simulations will be important in understanding the discrepancies between the simple heating models used in Chapters 2 and 3 and the simulation results from Chapter 4.

In this dissertation, I have investigated the heating of gas around a unique group of elliptical galaxies that are expected to contain the remnant energy from past episodes of AGN feedback. I successfully detected the tSZ effect, and found hints of AGN feedback energy around lower-mass galaxies with the SPT and no sign of AGN feedback energy around higher-mass galaxies with the ACT. I used a pair of state-of-the-art, large-scale cosmological simulations to further interpret my observational results, reinforcing the conclusions made previously. The work done here represents both an important step in understanding the complete picture of galaxy evolution and a significant motivation for further research on this very important topic, especially as more powerful, more advanced detectors make increasingly better CMB measure-

ments. The future is extremely promising, and our understanding of galaxy evolution and the role that AGN feedback plays is going to keep getting drastically better, with no end in sight.

REFERENCES

Alam, S., Albareti, F. D., Allende Prieto, C., et al. 2015, ApJS, 219, 12

Alpher, R. A., & Herman, R. C. 1948, Physical Review, 74, 1737

Anderson, T. W., & Darling, D. A. 1954, Journal of the American Statistical Association, 49, pp. 765

Antonucci, R. 1993, ARA&A, 31, 473

Arcila-Osejo, L., & Sawicki, M. 2013, MNRAS, 435, 845

Austermann, J. E., Aird, K. A., Beall, J. A., et al. 2012, in Proc. SPIE, Vol. 8452, Millimeter, Submillimeter, and Far-Infrared Detectors and Instrumentation for Astronomy VI, 84521E

Barger, A. J., Cowie, L. L., Mushotzky, R. F., et al. 2005, AJ, 129, 578

Battaglia, N., Bond, J. R., Pfrommer, C., Sievers, J. L., & Sijacki, D. 2010, ApJ, 725, 91

Bauer, A. E., Drory, N., Hill, G. J., & Feulner, G. 2005, ApJL, 621, L89

Bertin, E., & Arnouts, S. 1996, A&AS, 117, 393

Best, P. N., & Heckman, T. M. 2012, MNRAS, 421, 1569

Best, P. N., Kauffmann, G., Heckman, T. M., et al. 2005, MNRAS, 362, 25

Binney, J. 1977, ApJ, 215, 483

Birkinshaw, M. 1999, Phys. Rep., 310, 97

Bîrzan, L., Rafferty, D. A., McNamara, B. R., Wise, M. W., & Nulsen, P. E. J. 2004, ApJ, 607, 800

Blake, C., Davis, T., Poole, G. B., et al. 2011, MNRAS, 415, 2892

Bleem, L. E., Stalder, B., de Haan, T., et al. 2015, ApJs, 216, 27

Blumenthal, G. R., Faber, S. M., Primack, J. R., & Rees, M. J. 1984, Nature, 311, 517

Bongiorno, A., Schulze, A., Merloni, A., et al. 2016, A&A, 588, A78

Borguet, B. C. J., Arav, N., Edmonds, D., Chamberlain, C., & Benn, C. 2013, ApJ, 762, 49

Bower, R. G., Benson, A. J., Malbon, R., et al. 2006, MNRAS, 370, 645

Brammer, G. B., van Dokkum, P. G., & Coppi, P. 2008, ApJ, 686, 1503

Brinchmann, J., Charlot, S., White, S. D. M., et al. 2004, MNRAS, 351, 1151

Brüggen, M., & Scannapieco, E. 2009, MNRAS, 398, 548

Bruzual, G., & Charlot, S. 2003, MNRAS, 344, 1000

Buchner, J., Georgakakis, A., Nandra, K., et al. 2015, ApJ, 802, 89

Bundy, K., Ellis, R. S., & Conselice, C. J. 2005, ApJ, 625, 621

Burns, J. O. 1990, AJ, 99, 14

Cameron, E., Carollo, C. M., Oesch, P. A., et al. 2011, ApJ, 743, 146

Carlstrom, J. E., Ade, P. A. R., Aird, K. A., et al. 2011, PASP, 123, 568

Cattaneo, A., Haehnelt, M. G., & Rees, M. J. 1999, MNRAS, 308, 77

Cen, R., & Safarzadeh, M. 2015a, ApJL, 798, L38

—. 2015b, ApJL, 809, L32

Chabrier, G. 2003, PASP, 115, 763

Chamberlain, C., Arav, N., & Benn, C. 2015, MNRAS, 450, 1085

Chartas, G., Brandt, W. N., Gallagher, S. C., & Proga, D. 2007, AJ, 133, 1849

Chatterjee, S., Di Matteo, T., Kosowsky, A., & Pelupessy, I. 2008, MNRAS, 390, 535

Chatterjee, S., Ho, S., Newman, J. A., & Kosowsky, A. 2010, ApJ, 720, 299

Chatterjee, S., & Kosowsky, A. 2007, ApJL, 661, L113

Chen, Y.-M., Wild, V., Kauffmann, G., et al. 2009, MNRAS, 393, 406

Compton, A. H. 1923, Physical Review, 21, 483

Conroy, C., & Gunn, J. E. 2010, ApJ, 712, 833

Costa, T., Sijacki, D., & Haehnelt, M. G. 2014, MNRAS, 444, 2355

Cowie, L. L., & Barger, A. J. 2008, ApJ, 686, 72

Cowie, L. L., Songaila, A., Hu, E. M., & Cohen, J. G. 1996, AJ, 112, 839

Crichton, D., Gralla, M. B., Hall, K., et al. 2016, MNRAS, 458, 1478

Daddi, E., Cimatti, A., Renzini, A., et al. 2004, ApJ, 617, 746

Dark Energy Survey Collaboration, Abbott, T., Abdalla, F. B., et al. 2016, MNRAS, 460, 1270

Das, S., Marriage, T. A., Ade, P. A. R., et al. 2011, ApJ, 729, 62

Das, S., Louis, T., Nolta, M. R., et al. 2014, J. Cosmology Astropart. Phys., 4, 014

de Kool, M., Arav, N., Becker, R. H., et al. 2001, ApJ, 548, 609

Debuhr, J., Quataert, E., Ma, C.-P., & Hopkins, P. 2010, MNRAS, 406, L55

Desai, S., Armstrong, R., Mohr, J. J., et al. 2012, ApJ, 757, 83

Dolag, K., Komatsu, E., & Sunyaev, R. 2016, MNRAS, 463, 1797

Drory, N., & Alvarez, M. 2008, ApJ, 680, 41

Dubois, Y., Devriendt, J., Slyz, A., & Teyssier, R. 2012, MNRAS, 420, 2662

Dubois, Y., Pichon, C., Welker, C., et al. 2014, MNRAS, 444, 1453

Dunn, J. P., Bautista, M., Arav, N., et al. 2010, ApJ, 709, 611

Dünner, R., Hasselfield, M., Marriage, T. A., et al. 2013, ApJ, 762, 10

Eisenhardt, P. R. M., Wu, J., Tsai, C.-W., et al. 2012, ApJ, 755, 173

Enoki, M., Ishiyama, T., Kobayashi, M. A. R., & Nagashima, M. 2014, ApJ, 794, 69

Fabian, A. C. 2012, ARA&A, 50, 455

Farrah, D., Urrutia, T., Lacy, M., et al. 2012, ApJ, 745, 178

Faucher-Giguère, C.-A., & Quataert, E. 2012, MNRAS, 425, 605

Feenberg, E., & Primakoff, H. 1948, Physical Review, 73, 449

Feldmann, R., & Mayer, L. 2015, MNRAS, 446, 1939

Ferrarese, L. 2002, ApJ, 578, 90

Feruglio, C., Maiolino, R., Piconcelli, E., et al. 2010, A&A, 518, L155

Feulner, G., Gabasch, A., Salvato, M., et al. 2005, ApJL, 633, L9

Fitzpatrick, E. L., & Massa, D. 1999, ApJ, 525, 1011

Fontanot, F., De Lucia, G., Monaco, P., Somerville, R. S., & Santini, P. 2009, MNRAS, 397, 1776

Ganguly, R., & Brotherton, M. S. 2008, ApJ, 672, 102

Gralla, M. B., Crichton, D., Marriage, T. A., et al. 2014, MNRAS, 445, 460

Greco, J. P., Hill, J. C., Spergel, D. N., & Battaglia, N. 2015, ApJ, 808, 151

Greene, J. E., Zakamska, N. L., & Smith, P. S. 2012, ApJ, 746, 86

Grogin, N. A., Kocevski, D. D., Faber, S. M., et al. 2011, ApJS, 197, 35

Gunn, J. E. 1971, ApJL, 164, L113

Haehnelt, M. G., & Tegmark, M. 1996, MNRAS, 279, 545

Hamann, F. W., Barlow, T. A., Chaffee, F. C., Foltz, C. B., & Weymann, R. J. 2001, ApJ, 550, 142

Hand, N., Appel, J. W., Battaglia, N., et al. 2011, ApJ, 736, 39

Hasselfield, M., Hilton, M., Marriage, T. A., et al. 2013, J. Cosmology Astropart. Phys., 7, 008

Helou, G., & Walker, D. W., eds. 1988, Infrared astronomical satellite (IRAS) catalogs and atlases. Volume 7: The small scale structure catalog, Vol. 7

Hewett, P. C., & Foltz, C. B. 2003, AJ, 125, 1784

Hirschmann, M., Dolag, K., Saro, A., et al. 2014, MNRAS, 442, 2304

Hirschmann, M., Somerville, R. S., Naab, T., & Burkert, A. 2012, MNRAS, 426, 237

Hojjati, A., McCarthy, I. G., Harnois-Deraps, J., et al. 2015, J. Cosmology Astropart. Phys., 10, 047

Hojjati, A., Tröster, T., Harnois-Déraps, J., et al. 2016, ArXiv e-prints, arXiv:1608.07581

Hopkins, P. F., Richards, G. T., & Hernquist, L. 2007, ApJ, 654, 731

Hubble, E. P. 1929, ApJ, 69, 103

Ishihara, D., Onaka, T., Kataza, H., et al. 2010, A&A, 514, A1

Jones, F. C. 1965, Physical Review, 137, 1306

Kang, Y., Kim, Y.-L., Lim, D., Chung, C., & Lee, Y.-W. 2016, ApJS, 223, 7

Karachentsev, I. D., Karachentseva, V. E., Huchtmeier, W. K., & Makarov, D. I. 2004, AJ, 127, 2031

Kauffmann, G., & Haehnelt, M. 2000, MNRAS, 311, 576

Kauffmann, G., White, S. D. M., & Guiderdoni, B. 1993, MNRAS, 264, 201

Kaviraj, S., Devriendt, J., Dubois, Y., et al. 2015, MNRAS, 452, 2845

Kaviraj, S., Laigle, C., Kimm, T., et al. 2016, ArXiv e-prints, arXiv:1605.09379

Keller, B. W., Wadsley, J., & Couchman, H. M. P. 2016, MNRAS, arXiv:1604.08244

Kelly, P. L., von der Linden, A., Applegate, D. E., et al. 2014, MNRAS, 439, 28

Kimm, T., Kaviraj, S., Devriendt, J. E. G., et al. 2012, MNRAS, 425, L96

Knigge, C., Scaringi, S., Goad, M. R., & Cottis, C. E. 2008, MNRAS, 386, 1426

Kodama, T., Yamada, T., Akiyama, M., et al. 2004, MNRAS, 350, 1005

Koekemoer, A. M., Faber, S. M., Ferguson, H. C., et al. 2011, ApJS, 197, 36

Kriek, M., & Conroy, C. 2013, ApJL, 775, L16

Kriek, M., van Dokkum, P. G., Labbé, I., et al. 2009, ApJ, 700, 221

Kristian, J. 1973, ApJL, 179, L61

Lacey, C., & Cole, S. 1993, MNRAS, 262, 627

LaMassa, S. M., Urry, C. M., Cappelluti, N., et al. 2013, MNRAS, 436, 3581

Lanz, L., Ogle, P. M., Alatalo, K., & Appleton, P. N. 2016, ApJ, 826, 29

Lapi, A., Cavaliere, A., & De Zotti, G. 2003, ApJL, 597, L93

Lapi, A., Raimundo, S., Aversa, R., et al. 2014, ApJ, 782, 69

Lurie, J. C., Henry, T. J., Jao, W.-C., et al. 2014, AJ, 148, 91

Lynden-Bell, D. 1969, Nature, 223, 690

MacPherson, H. 1916, The Observatory, 39, 131

Marconi, A., & Hunt, L. K. 2003, ApJL, 589, L21

Marriage, T. A., Acquaviva, V., Ade, P. A. R., et al. 2011, ApJ, 737, 61

Mauch, T., Murphy, T., Buttery, H. J., et al. 2003, MNRAS, 342, 1117

McMahon, R. 2012, in Science from the Next Generation Imaging and Spectroscopic Surveys, 37

McNamara, B. R., Nulsen, P. E. J., Wise, M. W., et al. 2005, Nature, 433, 45

Menci, N. 2006, in ESA Special Publication, Vol. 604, The X-ray Universe 2005, ed. A. Wilson, 557

Merloni, A. 2004, MNRAS, 353, 1035

Merloni, A., & Heinz, S. 2008, MNRAS, 388, 1011

Merritt, D., & Ferrarese, L. 2001, ApJ, 547, 140

Mocanu, L. M., Crawford, T. M., Vieira, J. D., et al. 2013, ApJ, 779, 61

Mocz, P., Fabian, A. C., & Blundell, K. M. 2013, MNRAS, 432, 3381

Moe, M., Arav, N., Bautista, M. A., & Korista, K. T. 2009, ApJ, 706, 525

Murphy, T., Sadler, E. M., Ekers, R. D., et al. 2010, MNRAS, 402, 2403

Natarajan, P., & Sigurdsson, S. 1999, MNRAS, 302, 288

Neistein, E., van den Bosch, F. C., & Dekel, A. 2006, MNRAS, 372, 933

Newton, R. D. A., & Kay, S. T. 2013, MNRAS, 434, 3606

Noeske, K. G., Faber, S. M., Weiner, B. J., et al. 2007, ApJL, 660, L47

Oke, J. B., & Gunn, J. E. 1983, ApJ, 266, 713

Ostriker, J. P., Choi, E., Ciotti, L., Novak, G. S., & Proga, D. 2010, ApJ, 722, 642

Padin, S., Staniszewski, Z., Keisler, R., et al. 2008, Appl. Opt., 47, 4418

Page, M. J. 2001, MNRAS, 328, 925

Page, M. J., Symeonidis, M., Vieira, J. D., et al. 2012, Nature, 485, 213

Papovich, C., Moustakas, L. A., Dickinson, M., et al. 2006, ApJ, 640, 92

Peacock, J. A. 1983, MNRAS, 202, 615

Pei, Y. C. 1995, ApJ, 438, 623

Peng, C. Y., Ho, L. C., Impey, C. D., & Rix, H.-W. 2002, AJ, 124, 266

Penzias, A. A., & Wilson, R. W. 1965, ApJ, 142, 419

Piffaretti, R., Arnaud, M., Pratt, G. W., Pointecouteau, E., & Melin, J.-B. 2011, A&A, 534, A109

Pipino, A., Silk, J., & Matteucci, F. 2009, MNRAS, 392, 475

Planck Collaboration, Ade, P. A. R., Aghanim, N., et al. 2013, A&A, 557, A52

—. 2014, A&A, 571, A28

Planck Collaboration, Adam, R., Ade, P. A. R., et al. 2015a, ArXiv e-prints, arXiv:1502.01586

—. 2015b, ArXiv e-prints, arXiv:1502.01587

—. 2015c, ArXiv e-prints, arXiv:1502.01588

Planck Collaboration, Ade, P. A. R., Aghanim, N., et al. 2015d, ArXiv e-prints, arXiv:1502.01589

—. 2015e, ArXiv e-prints, arXiv:1502.01598

—. 2015f, ArXiv e-prints, arXiv:1502.01599

—. 2016, A&A, 586, A140

Platania, P., Burigana, C., De Zotti, G., Lazzaro, E., & Bersanelli, M. 2002, MNRAS, 337, 242

Rafferty, D. A., McNamara, B. R., & Nulsen, P. E. J. 2008, ApJ, 687, 899

Rafferty, D. A., McNamara, B. R., Nulsen, P. E. J., & Wise, M. W. 2006, ApJ, 652, 216

Rees, M. J., & Ostriker, J. P. 1977, MNRAS, 179, 541

Rees, M. J. 1984, ARA&A, 22, 471

Reichardt, C. L., Stalder, B., Bleem, L. E., et al. 2013, ApJ, 763, 127

Richard, J., Kneib, J.-P., Ebeling, H., et al. 2011, MNRAS, 414, L31

Richstone, D., Ajhar, E. A., Bender, R., et al. 1998, Nature, 395, A14

Rosas-Guevara, Y., Bower, R. G., Schaye, J., et al. 2016, MNRAS, 462, 190

Ruan, J. J., McQuinn, M., & Anderson, S. F. 2015, ApJ, 802, 135

Ruhl, J., Ade, P. A. R., Carlstrom, J. E., et al. 2004, in Society of Photo-Optical Instrumentation Engineers (SPIE) Conference Series, Vol. 5498, Z-Spec: a broadband millimeter-wave grating spectrometer: design, construction, and first cryogenic measurements, ed. C. M. Bradford, P. A. R. Ade, J. E. Aguirre, J. J. Bock, M. Dragovan, L. Duband, L. Earle, J. Glenn, H. Matsuhara, B. J. Naylor, H. T. Nguyen, M. Yun, & J. Zmuidzinas, 11–29

Scannapieco, E., & Oh, S. P. 2004, ApJ, 608, 62

Scannapieco, E., Silk, J., & Bouwens, R. 2005, ApJL, 635, L13

Scannapieco, E., Thacker, R. J., & Couchman, H. M. P. 2008, ApJ, 678, 674

Schaan, E., Ferraro, S., Vargas-Magaña, M., et al. 2016, Phys. Rev. D, 93, 082002

Schaffer, K. K., Crawford, T. M., Aird, K. A., et al. 2011, ApJ, 743, 90

Schawinski, K., Thomas, D., Sarzi, M., et al. 2007, MNRAS, 382, 1415

Schaye, J., Crain, R. A., Bower, R. G., et al. 2015, MNRAS, 446, 521

Schiller, F., & Przybilla, N. 2008, A&A, 479, 849

Schlegel, D. J., Finkbeiner, D. P., & Davis, M. 1998, ApJ, 500, 525

Schlegel, E. M., Jones, C., Machacek, M., & Vega, L. D. 2016, ApJ, 823, 75

Schmidt, M. 1963, Nature, 197, 1040

Seyfert, C. K. 1943, ApJ, 97, 28

Shankar, F., Weinberg, D. H., & Miralda-Escudé, J. 2013, MNRAS, 428, 421

Shankar, F., Bernardi, M., Sheth, R. K., et al. 2016, MNRAS, 460, 3119

Shields, G. A. 1999, PASP, 111, 661

Sijacki, D., Springel, V., Di Matteo, T., & Hernquist, L. 2007, MNRAS, 380, 877

Silk, J. 1968, ApJ, 151, 459

—. 1977, ApJ, 211, 638

Simionescu, A., Roediger, E., Nulsen, P. E. J., et al. 2009, A&A, 495, 721

Siudek, M., Małek, K., Scodeggio, M., et al. 2016, ArXiv e-prints, arXiv:1605.05503

Skelton, R. E., Whitaker, K. E., Momcheva, I. G., et al. 2014, ApJS, 214, 24

Soergel, B., Flender, S., Story, K. T., et al. 2016, MNRAS, 461, 3172

Spacek, A., Scannapieco, E., Cohen, S., Joshi, B., & Mauskopf, P. 2016, ApJ, 819, 128

—. 2017, ApJ, 834, 102

Sturm, E., González-Alfonso, E., Veilleux, S., et al. 2011, ApJL, 733, L16

Sunyaev, R. A., & Zeldovich, Y. B. 1970, Ap&SS, 7, 3

—. 1972, Comments on Astrophysics and Space Physics, 4, 173

Swetz, D. S., Ade, P. A. R., Amiri, M., et al. 2011, ApJS, 194, 41

Teimoorinia, H., Bluck, A. F. L., & Ellison, S. L. 2016, MNRAS, 457, 2086

Teyssier, R. 2002, A&A, 385, 337

Thacker, R. J., Scannapieco, E., & Couchman, H. M. P. 2006, ApJ, 653, 86

Thornton, R. J., Ade, P. A. R., Aiola, S., et al. 2016, ArXiv e-prints, arXiv:1605.06569

Tombesi, F., Meléndez, M., Veilleux, S., et al. 2015, Nature, 519, 436

Tremaine, S., Gebhardt, K., Bender, R., et al. 2002, ApJ, 574, 740

Treu, T., Ellis, R. S., Liao, T. X., & van Dokkum, P. G. 2005, ApJL, 622, L5

Ueda, Y., Akiyama, M., Ohta, K., & Miyaji, T. 2003, ApJ, 598, 886

van der Wel, A., Bell, E. F., Häussler, B., et al. 2012, ApJS, 203, 24

Veilleux, S., Meléndez, M., Sturm, E., et al. 2013, ApJ, 776, 27

Vergani, D., Scodeggio, M., Pozzetti, L., et al. 2008, A&A, 487, 89

Voges, W., Aschenbach, B., Boller, T., et al. 1999, A&A, 349, 389

Voit, G. M. 1994, ApJL, 432, L19

Wampler, E. J., Chugai, N. N., & Petitjean, P. 1995, ApJ, 443, 586

White, S. D. M., & Frenk, C. S. 1991, ApJ, 379, 52

White, S. D. M., & Rees, M. J. 1978, MNRAS, 183, 341

Wright, A. E., Griffith, M. R., Burke, B. F., & Ekers, R. D. 1994, ApJs, 91, 111

Wright, E. L., Eisenhardt, P. R. M., Mainzer, A. K., et al. 2010, AJ, 140, 1868

Wuyts, S., Labbé, I., Schreiber, N. M. F., et al. 2008, ApJ, 682, 985

Wyithe, J. S. B., & Loeb, A. 2002, ApJ, 581, 886

—. 2003, ApJ, 595, 614

Yamamura, I., Makiuti, S., Ikeda, N., et al. 2010, VizieR Online Data Catalog, 2298, 0